The Pennsylvania State University

The Graduate School

Graduate Program in Acoustics

DETERMINATION OF INTERNAL PIPE ACOUSTIC PRESSURE USING EXTERNAL ACCELEROMETERS

A Thesis in

Acoustics

by

Alexandria R. Salton

Submitted in Partial Fulfillment

of the Requirements

for the Degree of

Master of Science

August 2011

The thesis of Alexandria R. Salton was reviewed and approved* by the following:

Dean E. Capone
Senior Research Associate, Associate Professor of Acoustics
Thesis Advisor

William K. Bonness
Research Associate

John B. Fahnline
Research Associate
Assistant Professor of Acoustics

Victor W. Sparrow
Professor of Acoustics
Interim Chair, Graduate Program in Acoustics

*Signatures are on file in the Graduate School.

ABSTRACT

A non-invasive method utilizing a ring of accelerometers to measure pipe interior acoustic pressures is presented. The internal acoustic pressure of the fluid inside a cylindrical pipe is directly related to the vibrations at the surface due to the coupling of the fluid and structure. The breathing mode provides the basis for this relationship and is extracted from accelerometer data using a circumferential modal decomposition routine. The measurement of pipe interior pressures can be useful in determining the integrity of a piping system by detecting high pressures, which may lead to the fatigue or failure of the system. In an operating industrial application, invasive pressure measurements may be undesirable or even impossible. Therefore, a non-invasive method for measuring these pressures is required.

Challenges introduced by using this particular method and the error they produce in the calculation of pressure, are investigated through an analytical model. The factors include the placement of the accelerometers in an equally-spaced circumferential ring, the transverse sensitivity of the measurement accelerometers, pipe wall thickness, and energy distribution. Experimental measurements are taken on a water-filled aluminum pipe to assess the feasibility of using a ring of accelerometers for the internal acoustic

pressure measurement. The pressure calculated using the accelerometers is compared to direct measurements using flush-mounted wall pressure sensors. The calculated pressure tracks the directly-measured pressure very accurately. However at this time, although a ring of accelerometers can aid in monitoring changes in acoustic pressure, additional sensors are needed to determine absolute pressure levels.

TABLE OF CONTENTS

LIST OF FIGURES

LIST OF TABLES

LIST OF SYMBOLS

a	mean radius of the shell
$\mathcal{B}$	fluid bulk modulus
c	velocity of propagation
d	pipe diameter
f	frequency
E	Young's modulus
Fl	fluid loading
h	thickness
H	Hankel function
J	Bessel function
k	wavenumber
m	axial mode number
M	moment resultant
n	circumferential mode number
N	force resultant
p	acoustic pressure
p	radial mode number

P	pressure amplitude
q	angle between pipe axis and direction of maximum transverse sensitivity
Q	force resultant
r	radial co-ordinate
t	time
T	percentage transverse sensitivity
u	axial displacement
U	axial displacement amplitude
v	tangential displacement
V	tangential displacement amplitude
w	radial displacement
W	radial displacement amplitude
z	axial co-ordinate
α	circumferential angle
β	$= (h/a)/\sqrt{12}$, relative thickness
γ	polarization angle
γ	shear strain
Γ	non-dimensional constant
ϵ	normal strain
ζ	non-dimensional radial wavenumber
η	material loss factor
θ	circumferential angle
κ	non-dimensional axial wavenumber
Λ	power factor
μ	propagation factor
ν	Poisson ratio

ξ	wavenumber constant
ρ	mass density
σ	normal stress
τ	shear stress
ϕ	polarization angle
ψ	non-dimensional constant
ω	angular frequency
Ω	non-dimensional frequency

Indices

a	acoustic
b	bending
e	external
f	fluid
i	internal
l	longitudinal
s	solid
t	torsional
$+$	positive direction
$-$	negative direction

Operators

Re	real part
$\bar{}$	time average
$\langle\rangle$	spacial average
$\cdot$	temporal derivative
$*$	complex conjugate

ACKNOWLEDGMENTS

The Graduate Program in Acoustics at Penn State University is the reason I made the move to Pennsylvania. After spending two years here, I am so thankful I decided to study acoustics at Penn State. I'd like to acknowledge the extremely knowledgeable faculty for providing me with a strong foundation in acoustics that I know will help me throughout my career. Not only have I learned a great amount from my professors, the students provided me with a strong and diverse intellectual community that has surely made me grow. The support of the faculty and students in the Graduate Program in Acoustics is unique and my appreciation can not be expressed enough.

I would also like to acknowledge the support from the Applied Research Laboratory (ARL) for providing a Graduate Assistantship through the Exploratory and Foundational (E & F) Graduate Student Research Program. I had the pleasure of working in the Garfield Thomas Water Tunnel and would like to acknowledge all of the staff and technicians there who were always willing to help me in each step of my project.

Above all, I'd like to thank my advisor, Dr. Dean Capone, for not only providing me with this project but also with advice and guidance throughout my two years at Penn State. And to Dr. William Bonness, who spent an equal amount of time helping me construct my project and providing suggestions to move forward. To all my committee

members, Dr. Dean Capone, Dr. William Bonness and Dr. John Fahnline, thank you for taking the time to read my thesis and for all of your helpful feedback and suggestions. I truly appreciate it.

And to my family, I surely would have not been here without their support. Thank you for instilling in me the importance of education from a very young age. It has led me to Penn State and provided me with the opportunity to meet and work with so many amazing individuals.

CHAPTER 1

INTRODUCTION

1.1 Motivation

Many piping systems built for the transport of fluids (such as water, natural gas, steam, etc.) have two concerns in common: maintenance and noise. Maintaining the piping system's integrity is a major concern. The system must be monitored throughout its lifetime in order to detect fatigue before it leads to an irreversible failure. Along with many other details that are monitored, changes in the acoustic pressure can provide information about possible leaks or other minor failures. Internal acoustic pipe pressure is also related to pipe noise. Propagating acoustic energy in the pipe creates an internal pressure field which interacts with the pipe wall causing it to vibrate. The vibrations of the pipe wall cause a disturbance in the external medium by radiating sound.

Directly measuring the internal acoustic pressure through traditional methods, such as using a hydrophone, requires drilling through the pipe wall to access the internal fluid. This is often undesirable. Therefore, non-invasive methods for measuring the

internal acoustic pressure of piping systems have been a topic of research applied to many industrial fields requiring piping system maintenance. Non-invasive methods take advantage of the coupling between the internal pressure field and the pipe wall vibrations. The fluid couples to the pipe wall in the normal direction, so the internal pressure can be determined indirectly by measuring the external vibrations. A number of non-invasive motion sensors have been developed and refined for the purpose of measuring internal acoustic pipe pressure.

This thesis is concerned with the feasibility of utilizing a ring of piezoelectric accelerometers in accurately detecting the internal acoustic pressure. The accelerometer sensors use the piezoelectric effect to create an electrical output that is proportional to the acceleration and are a common tool in vibration analysis. Therefore, as a familiar sensor in the field, the use of accelerometers in monitoring the internal acoustic pressure of piping systems would be relatively easy to implement. However, literature related to the use of accelerometers in this specific application is difficult to find, and when briefly mentioned, is not given an in-depth analysis.

Accelerometers are often chosen for the purpose of performing experimental modal analysis for a variety of reasons. A ring configuration of accelerometers is proposed in this work to measure the spatial harmonic motion of the pipe. With this configuration, a modal analysis can be performed to separate the circumferential modes. Determining modal contributions is important, as the internal acoustic pressure is directly related to the radial displacements contributed by the breathing mode, which is dominated by the energy from the acoustic fluid propagating wave. Theoretically, if the internal acoustic pressure is related to the breathing mode radial displacements of the pipe wall, any sensor with the ability to measure these radial displacements could be used to calculate the internal acoustic pressure. Schirmacher and Baars [1] utilize a circumferential and axial

array of tri-axial accelerometers to separate wavetype contributions with the objective of studying sound propagation in a high pressure gas pipe to design noise reduction devices. They determine the modal amplitudes in order to calculate the power flows from each mode, finding that "the main power transport is done by fluid borne sound" and claiming that the results were "backed impressively by a verifying pressure measurement" [1]. Although they provide some values of the power flows to confirm the dominance of the plane fluid wave, there are no plots or further explanation of the pressure measurements.

Also utilizing a circumferential and axial array of accelerometers, Conti, Stokes, and Corrado [2] characterize the noise from piping components such as valves and bends "by estimating the acoustic scattering matrix representations" [2] of these components. Although the scope of their project is larger than just measuring internal acoustic pressure, they give a brief mention to the ability of radially oriented accelerometers to "non-invasively measure fluid wave propagation" [2]. Although it appears that they are successful in measuring the non-dispersive fluid wave, there is no development of the relationship to internal pressure, as they employ other methods of analysis for characterizing the noise.

A less successful use of accelerometer rings for this purpose is mentioned in the thesis by deJong [3]. The objective of the thesis is to study the pulsations and vibrations in fluid piping systems and deJong states his concern that "although there is a direct relationship between the pressure in a flexible pipe and the radial 'breathing' motion of the pipe wall, the corresponding radial acceleration may be too small to be measured with accelerometers". The experiments deJong performed take advantage of a combination of strain gages and accelerometers. With respect to the use of accelerometers alone, deJong recommends that "the measurement of radial wall accelerations ($n = 0$) is not adopted, since these measurements will very likely be hampered by the transverse axis sensitivity

of the accelerometers". He goes on to suggest the work by Pinnington and Briscoe [4] using piezoelectric wire (PVDF) to overcome the problem of transverse sensitivity. In addition to Pinnington and Briscoe [4], Royston [5] and Muggleton, Brennan, Pinnington and Gao [6] have also published studies concerning the use of PVDF material to measure internal acoustic pipe pressure.

As mentioned by deJong [3], strain gages have been utilized for the purpose of measuring internal pipe pressure and have shown good results by Szasz, Fujikawa and DeBoo [7]. They implement strain gages arranged in a "T" configuration to measure the dynamic pressures of pipes and concluded that this configuration was a "viable and cost effective way of monitoring the acoustic loads that may be acting on piping and pressure vessel internals". Although many sensors show promise, sensor selection depends on several factors including the sensor's specifications related to sensitivity, cross sensitivity, noise floor, and environmential conditions.

Accelerometers have been reviewed favorably and unfavorably for measuring the fluid propagating wave. However, a more in-depth analysis is needed to assess the measurement accuracy that can be achieved using a ring of accelerometers. Due to the popularity of accelerometers in the field of vibration analysis and the relative ease in their application, the use of accelerometers for the indirect and non-invasive measurement of the internal acoustic pressure of piping systems warrants further research. This thesis attempts to provide a more in-depth analysis to assess the performance of accelerometers in overcoming the challenges faced in accurately predicting the internal acoustic pressure in piping systems.

1.2 Relationship between pipe wall motion and internal acoustic pressure

Fluid cannot support shear stresses, so the internal fluid couples with the pipe wall in the normal direction only, which corresponds to the radial direction in the case of circular cylindrical shells. The continuity condition requires the radial movements of the fluid and wall to be equal at their interface. Therefore, the radial wall vibration is directly related to the internal pressure. The relationship between the internal pressure field and the radial wall vibrations follows from the expression for the general pressure field inside a rigid walled cylinder from acoustic duct theory [8],

$$p = \sum_m \sum_n \sum_p P_{mnp} J_n(k_r^p r) e^{n\theta} e^{k_m z} e^{i\omega t}, \tag{1.2.1}$$

where P_{mnp} is determined via Euler's equation applied at the interface $r = a$

$$i\omega w = -\left(\frac{1}{i\rho_f \omega}\right) \left.\frac{\partial p}{\partial r}\right|_{r=a}, \tag{1.2.2}$$

which leads to the general expression of the internal acoustic pressure as a function of the radial vibrations,

$$p = \rho_f \omega^2 w \frac{J_n\left(k_r^p r\right)}{k_r^p J_n'\left(k_r^p a\right)}, \tag{1.2.3}$$

where ρ_f is the fluid density, ω is the radial frequency, k_r is the radial wavenumber, and J_n is the nth order Bessel function. The cylindrical coordinates z, r and θ correspond to the axial, radial and circumferential directions. The axial, circumferential, and radial mode orders correspond to the variables m, n and p. The radial displacement w in Equation (1.2.3) is assumed to be the radial motion associated with the internal acoustic

propagating wave.

The radial pipe wall motion is a superposition of circumferential modes. The lowest circumferential mode order, $n = 0$, is often called the breathing or axisymmetric mode, named for its uniform (in-phase) radial motion. The propagating internal acoustic energy in the fluid is strongly coupled to the $n = 0$ breathing mode. Therefore, this mode is of utmost concern to the present discussion. Yet, measuring the contributions from the breathing mode is difficult as its amplitude of radial vibration due to propagating acoustic waves is small in comparison to the higher order circumferential modes. The $n = 1$ circumferential mode often dominates the radial motion at low frequencies, presenting a major challenge in extracting the smaller amplitude breathing motion of the pipe. The $n = 1$ mode is termed the beam bending mode for its lateral motion without deformation of the cross-section. The higher order circumferential modes $n \geq 2$, are termed lobar modes, all of which involve deformation of the cross section. The $n = 0$ and $n = 1$ modes exist at all frequencies, however there is a cut-on frequency corresponding to each lobar mode, below which the mode cannot propagate. Therefore, it is important to compute these cut-on frequencies in order to identify the circumferential modes that exist within the frequency range of interest.

External sensors mounted to the pipe wall will detect the total radial motion including the contributions from all circumferential modes within the defined frequency range. Therefore, the problem can be somewhat simplified by limiting the frequency range to only include frequencies below the cut-on of the first lobar mode. Cut-on frequencies also exist for the waveguide radial acoustic modes p in the fluid, where plane-wave propagation only exists at $p = 0$. Therefore, another simplification can be made that limits the analysis range to frequencies below the cut-on of the first non-plane wave mode. This also ensures that the pressure distribution across the cross-section will be

uniform.

Another important identifying frequency limitation is the ring frequency, below which wall curvature effects dominate and above which the curvature effects are weak and the shell vibrates as a flat plate. The ring frequency is related to the speed at which membrane waves travel around the pipe circumference and it is related to the natural frequency of the $n = 0$ mode. It is expressed as $f_{ring} = c_s/2\pi a$, where c_s is the longitudinal plate speed and a is the radius of the pipe. For pipes in industrial applications, interest in pipe vibration is often limited to frequencies below the ring frequency where the wall curvature effects are dominant. These frequency limitations will be discussed in more detail in Chapter 2 as they pertain to shell and duct modes.

For frequencies much below the ring frequency, Pavic [9] states that only the $n = 0$ and $n = 1$ modes allow wave propagation along the pipe without spatial attenuation. There are four propagating waves related to these modes. The $n = 0$ response accounts for three of these wavetypes, one being the torsional wave related only to circumferential motion and uncoupled from axial and radial motion. The other two being the previously mentioned acoustical wave and the longitudinal wave which are coupled in the axial and radial directions, due to the effect of wall curvature. The fourth wavetype is the flexural wave corresponding to the $n = 1$ bending mode. Inclusion of the $n = 2$ mode introduces another wave-type and makes the analysis of pipe motion even more complex. Therefore, as noted before, special attention must be given to the cut-on frequency of the first lobar mode to avoid a more complicated analysis.

If the external sensors are able to extract the pure $n = 0$ breathing motion, it still consists of motion contributed by energy from the longitudinal wave as well as the desired acoustical wave. Pinnington and Briscoe [4] discuss the proper equation for pressure based on the ratio of acoustical radial motion to longitudinal radial motion.

This thesis focuses on Equation (1.2.3), which assumes that the radial wall motion is dominated by the acoustic fluid wave. The analytical model developed in Chapter 3 will analyze the limiting ratios of acoustic to longitudinal energy that will still allow the accurate prediction of acoustic pressure using the described equation. Under the assumption that the acoustical energy dominates the pipe radial response, the external sensors must accurately measure the relatively small vibrations corresponding to the $n = 0$ breathing mode, which is directly related to the internal acoustic pressure. Attention to the sensor configuration and cross-sensitivity of the accelerometers may help in the accurate extraction of the small amplitude vibrations of the $n = 0$ breathing mode.

1.2.1 Sensor configuration

The frequency range of interest is much below the natural frequency of the $n = 0$ breathing mode, which is related to the ring frequency of the pipe. Therefore the amplitude of the radial vibrations corresponding to travelling acoustic waves in the fluid are much smaller in comparison to the higher order pipe modes whose cut-on frequencies occur below the ring frequency. Therefore, the sensors must be built or configured in a way that they will be robust enough to reject the effects of other shell modes.

Configuring accelerometers in an equally-spaced ring around the circumference can take advantage of the circumferential harmonic motion of the pipe. Circumferential modal decomposition can be used to determine the respective amplitudes of each circumferential mode that exists within the defined frequency range. The $n = 0$ breathing mode is defined by its in-phase radial motion and is easily found by rejecting all out-of-phase components of motion. Conti, Stokes and Corrado [2] refer to the arrangement of accelerometers as a stave array composed not only of circumferential rings, but also arrays along the axial direction. In order to avoid aliasing, the number of sensors in the

circumferential ring must satisfy the Nyquist criteria. This is satisfied if there are $2N+1$ accelerometers, where N is the highest circumferential mode present in the frequency range of interest. Schirmacher and Baars [1] experiment with five rings of four equally-spaced accelerometers, which allows them to detect the $n = 0$ breathing mode and the $n = 1$ bending mode. This configuration relies heavily on the exact placement of the sensors, because if the opposite pairs are not exactly opposite, their measurements may produce errors in the circumferential decomposition of the modal amplitudes. The level of inaccuracy produced by an offset of the accelerometer placement is analyzed through the use of the model developed in Chapter 3. The method analyzed in this thesis is only concerned with the performance of an individual circumferential ring of accelerometers in predicting the internal acoustic pressure. Further research may find benefits to adding more axial positions to the analysis.

1.2.2 Sensor cross-sensitivity

When measuring the radial motion utilizing accelerometers, it is assumed that only radial motion is being measured. However, every accelerometer has some cross-sensitivity (transverse-sensitivity) that may allow the measurements to be contaminated with the motion from the other two orthogonal directions. The amount of contamination depends on the orientation of the sensor as well as the orientation of the sensing material itself. Accelerometers have at least 4% cross sensitivity to other motion [4], though it should be noted that accelerometers can be chosen that have a minimal cross-sensitivity by design. The analytical model developed in Chapter 3 will analyze the effect of accelerometer cross-sensitivity on the accuracy of utilizing a ring of accelerometers to indirectly measure the internal acoustic pressure.

1.3 Piping systems and their components

The inherent geometry of a pipe, material properties of the pipe wall, and properties of the contained fluid will all have an effect on the vibration response of the pipe to mechanical or acoustical excitations. In general, pipes are described as small diameter, thick walled circular cylindrical shells. Relative to large diameter, thin-walled applications such as aircraft fuselages or submarine hulls, this description of pipes is accurate. However, thin-shell theory used to describe shell motion is still applied to pipes due to the relatively small amplitude vibrations in comparison to the shell thickness. Thin shell theory requires the thickness-to-radius ratio h/a to be small enough so that higher powers of h/a can be neglected in comparison to unity. The ratio of length to diameter also separates pipes from other forms of circular cylindrical shells as it is usually much larger than for a large diameter and thin-walled shell.

Applying the same amplitude of acoustic pressure to a thicker walled pipe will produce smaller amplitude vibrations than for a thinner walled pipe, which will make the sensor's ability to detect the $n = 0$ breathing motion even more difficult. Similar to a change in thickness, a more rigid pipe wall material such as steel will deform less than a more flexible pipe material such as plastic. However, the flexibility of the material may present new challenges, such as the acoustic signals being heavily attenuated and the frequencies being generally low and narrow-band [10]. The analytical model in Chapter 3 will help to shed light on the effects of varying pipe geometry and material.

The internal fluid will also have an effect on pipe vibrations. Pipes may transport heavy or light fluids and this will affect the pressure field inside the pipe and in turn the pipe vibrations. A metal pipe containing air behaves much like a rigid-walled duct, with its vibration amplitudes being extremely small. Heavier fluids such as water with a higher fluid density will exert larger fluid loading on the shell and will lower the cut-

on frequencies of the circumferential shell modes, limiting the analysis range to lower frequencies.

For pipes, people are generally concerned with noise escaping from the system rather than entering the system [11]. The flow of the fluid is controlled by valves which will produce a large amount of acoustic energy in the pipe. Pumps may also present a mechanical source producing acoustic energy in the pipe. Other sources of acoustic energy can be caused from elbows or flanges. In the laboratory, sources of sound are produced using loudspeakers and shakers. The range of frequencies in which noise from these components is generally produced is in the lower range below 1 kHz. Therefore the sensor's performance at low frequencies is essential to accurate measurements. Experiments conducted for this thesis (discussed in Chapter 4) will utilize an acoustic projector and electromagnetic shaker to excite internal acoustic pulsations as an acoustical source and mechanical source respectively.

The layout of the piping system presents another challenge in the way the sensors are configured. The piping system may contain turns or other components making it difficult to locate an ideal measurement location. An ideal location would be one placed on a long straight run of pipe far from any discontinuities.

1.4 Environmental conditions

Although this thesis will not provide an in-depth discussion of the selection of sensors based on environmental conditions, it is an important factor in sensor selection and warrants brief mention here. Even if a sensor is chosen which exhibits the largest sensitivity, lowest noise floor at low frequencies, smallest cross-sensitivity, and an advantageous configuration, it cannot be used if it does not have the ability to withstand the harsh environmental conditions in which the piping system is placed. Sensor characteristics

are easily found on specification sheets which describe the limitations of the sensor in regards to temperature, maximum acceleration or strain, and resistance to corrosive fluids. Industrial applications in which these sensors would be used to monitor internal acoustic pressure are often under high pressure and high temperature and in the case of nuclear power plants, in the presence of intense nuclear radiation. Sensors must be selected in terms of their ability to withstand the harsh conditions imposed on them. Sensors can be designed for their specific applications and there are a wide variety of designs available, each with their own advantages and limitations. Based on the specific environment, a sensor can be selected that best meets the needs of the measurements.

The sensing element of accelerometers is made with long-term stability in mind. Quartz and Lead-zirconate-titinate (PZT) are both used to manufacture accelerometers. Although quartz exhibits long-term stability, PZT naturally decays over time and requires frequent calibration [12]. Therefore, the accelerometers that contain PZT are artificially aged at the factory in order to lessen the amount of decay seen by the consumer. Additionally, accelerometers with noncorrosive nonmagnetic stainless steel cases can be selected specifically for harsh conditions in order to resist the effect of harsh chemicals. Connectors are also offered in order to seal the accelerometers from outside contaminants.

1.5 Overview

The following chapters provide an in-depth discussion of the challenges faced in indirectly measuring the internal acoustic pressure by the extraction of the $n = 0$ breathing mode utilizing a ring of accelerometers. Chapter 2 presents the background required to delve more deeply into the subject of fluid-structure interactions and wave propagation in fluid-filled pipes. These subjects are the foundation for the development of an analytical

model in Chapter 3. The model will analyze the effect of varying parameters such as propagating wave energies, pipe geometry and material, and accelerometer inaccuracies. This model will be useful in determining why errors are present in the experimental results presented in Chapter 4. These results compare the method utilizing a non-invasive circumferential ring of accelerometers to the direct method of measuring the internal pressure with flush-mounted pressure sensors.

The desired outcome of this research is to determine the feasibility of using a ring of accelerometers to indirectly measure the acoustic pressure in a pipe. The relationship between internal acoustic pressure and the external displacements of the pipe wall is well known and has been extensively studied. The method utilizing accelerometers to detect the desired displacements and calculate the internal pressure shows promise. The following discussion will present an assessment of the most prevalent challenges in using this method and the alterations for improving the performance for use in future research and eventual installation.

CHAPTER 2

MATHEMATICAL FORMULATION

2.1 Introduction

This chapter presents a review of the underlying equations and assumptions used in deriving the relationship between the internal acoustic pressure and external surface vibrations of a cylindrical pipe. The review begins with the subjects of thin shell theory and fluid wave-guides to introduce the equations that govern the shell and fluid motion separately. After developing an understanding of their separate solutions, the solution to the coupled motion of the fluid filled cylindrical shell is presented. A circumferential decomposition technique used to extract individual vibrational modes is presented, with a focus on the uniform radial motion exhibited by the $n = 0$ breathing mode. Extracting the character of the $n = 0$ breathing mode is the key to correctly calculating the internal acoustic pressure, as the radial motion from this mode is dominated by the energy transferred by the acoustic propagating wave. A brief overview of wave propagation and energy flow through straight pipes not only heightens awareness of the challenges faced

in measuring radial vibrations responding purely to the acoustic propagating wave, but also presents a powerful tool in modelling surface displacements of a pipe. The chapter ends with the derivation of a simpler expression for the internal acoustic pressure and it's relationship with the material properties and fluid-loading. The simplified expression also provides a link to a precise theoretical expression for internal acoustic pressure that takes advantage of the fluid-loading terms corresponding to the different propagating waves. The model described in Chapter 3 makes use of the two pressure expressions to compare an exact and approximate calculation of pressure.

The internal acoustic pressure of a fluid-filled cylindrical pipe is directly related to the external radial vibrations at the pipe's surface. This relationship is a consequence of the coupled motion of the structure and its contained fluid, as well as the continuity condition at their interface. The subject of fluid structure interaction is covered in numerous texts, including Junger and Feit [13] and Fahy and Gardonio [11]. In these texts, a section on fluid-loading will often derive the relationship between acoustic pressure and normal surface vibrations for various structures. The normal surface vibrations of a cylindrical pipe correspond to motion in the radial direction. The radial motion desired in computing the internal acoustic pressure corresponds to the $n = 0$ 'breathing' mode, named for its uniform circumferential motion as if the pipe were breathing in and out. This mode is dominated by the energy from the acoustic fluid wave. The presence of higher order modes of vibration and other propagating modes can present challenges in accurately computing an internal acoustic pressure from the external surface vibrations.

2.2 Solution of a fluid-filled shell of circular cross section

The surface of a fluid-filled cylindrical shell of circular cross-section locally reacts to pressure fluctuations in the fluid, resulting in a coupled solution between the fluid and

structure. However, the shell and its contained fluid must still satisfy the equations of motion and acoustic wave equation respectively. Since a fluid cannot support shear stress, the interaction between a structure and its contained fluid occurs only in the direction normal to the structure, which is in the radial direction for a cylindrical shell. The coupled solution requires continuity at the interface of the fluid and structure, and the momentum equation provides the relationship between displacement normal to the surface and the internal acoustic pressure. The equations and theories that govern shell and fluid motion as well as their coupled solutions have been studied in-depth by many authors including de Jong [3], Fahy and Gardonio [11], Junger and Feit [13], Leissa [14], Pavic [9], Skelton and James [15], Soedel [16] and many others not included in this list. This section gives a brief overview of the important equations and assumptions involved in solving for the motion of a shell and fluid.

Cylindrical shell motion is described using "thin shell" theory, which introduces a number of assumptions in order to simplify the equations of motion. The motion of the contained fluid is described through the derivation of the linear acoustic wave equation and its solution for a cylindrical waveguide. Once the displacement of the shell and the internal acoustic pressure of the fluid are understood separately, the coupled solution is presented.

2.2.1 Shell motion

The equations of motion for a cylindrical shell, even in their simplest form are still quite complicated. The various "thin shell" theories attempt to simplify the complicated equations of motion for shells by making a number of simplifying assumptions. For a more in-depth discussion of the intricacies involved in the derivation of each of the thin shell theories, Leissa [14] has provided an extensive review of the subject. The development

presented here will follow the work of Leissa [14], deJong [3] and Soedel [16]. The thin shell theories derived in Leissa[14] can all be obtained from Love's postulates, and only differ in terms proportional to the non-dimensional shell thickness parameter $\beta^2 = h^2/12a^2$ for cylindrical shells. These differences arise from the simplifying assumptions made, or the point at which the assumptions are used in the derivations of the strain-displacement equations and the force and moment resultants.

The following formulations will make use of the coordinate system presented in Figure 2.1(a), where z, θ, and r are the cylindrical coordinates and u, v and w are the orthogonal components of displacement. The shell is described by it's radius of curvature, a, at the middle surface and it's thickness, h.

The discussion will begin with Love's "first approximation" shell theory which provides the basis for the derivation of other thin shell theories. Love made four simplifying assumptions in evaluating the small displacements of thin shells. The first defined a "thin shell" as one whose thickness was small compared with its other dimensions. The second required the strains and displacements to be sufficiently small so that the equations remain linear. The third allows the transverse normal stress to be neglected as it is small compared to the other normal stress components. The last assumption is known as Kirchoff's hypothesis: "normals to the undeformed middle surface remain straight and normal to the deformed middle surface and suffer no extension"[14]. Kirchoff's hypothesis is a geometric assumption that results in the following equation:

$$\left.\begin{aligned} \gamma_{zr} &= 0 \\ \gamma_{\theta r} &= 0 \\ \epsilon_r &= 0 \end{aligned}\right\}, \tag{2.2.1}$$

where γ_{zr} and $\gamma_{\theta r}$ are the shear strains in-plane with the middle surface and ϵ_r is the

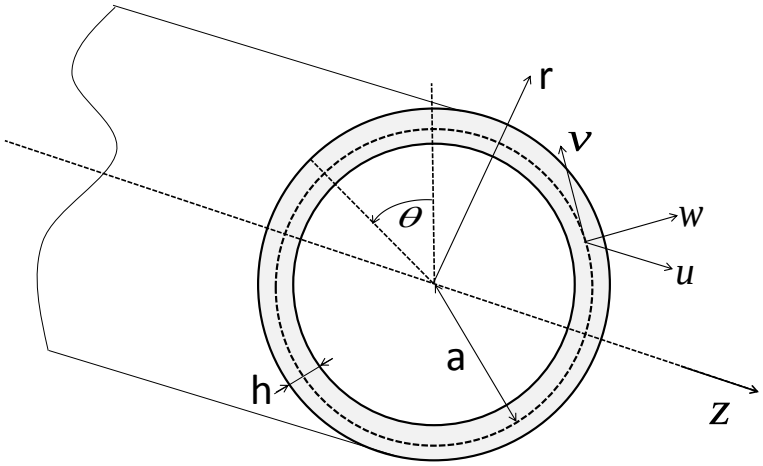

(a) coordinates of a cylindrical shell

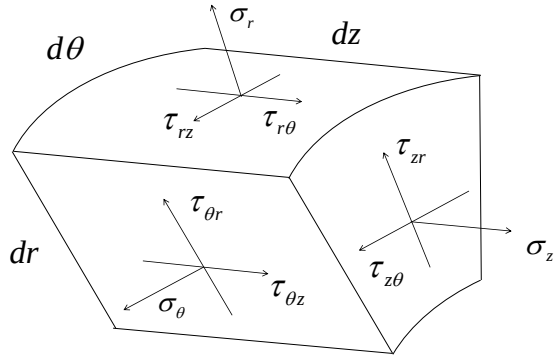

(b) Positive stresses

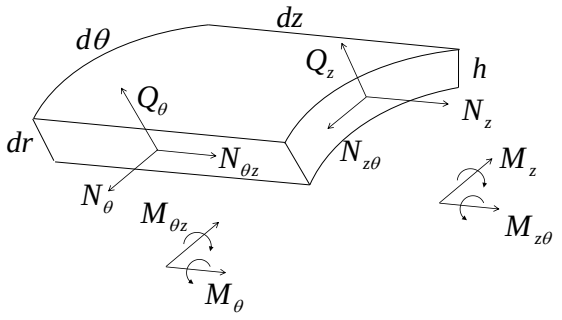

(c) Resultant forces and moments

Figure 2.1. Geometry of cylindrical shell and shell elements

strain normal to the middle surface. These assumptions lead to the transverse shear stresses,

$$\tau_{zr} = \tau_{\theta r} = 0, \tag{2.2.2}$$

as a result of Hooke's law. The middle surface is defined when $r = a$ and the in-plane displacements vary linearly through the thickness of the shell [3],

$$u \approx u_0 - (r-a)\frac{\partial w_0}{\partial z}, \quad v \approx v_0 - \frac{r-a}{a}\left(\frac{\partial w_0}{\partial \theta} - v_0\right), \quad w \approx w_0, \tag{2.2.3}$$

where the indice '0' denotes the middle surface. The remaining normal and shear strains are defined by the strain-displacement equations [3, 16],

$$\epsilon_z = \frac{\partial u}{\partial z}, \quad \epsilon_\theta = \frac{1}{a}\frac{\partial v}{\partial \theta} + \frac{w}{a}, \quad \gamma_{z\theta} = \gamma_{\theta z} = \frac{\partial v}{\partial z} + \frac{1}{a}\frac{\partial u}{\partial \theta}, \tag{2.2.4}$$

where the relationship between the stresses and strains is defined by Hooke's law and leads to the normal and shear stresses,

$$\sigma_z = \frac{E}{1-\nu^2}\left(\epsilon_z + \nu\epsilon_\theta\right), \quad \sigma_\theta = \frac{E}{1-\nu^2}\left(\epsilon_z + \nu\epsilon_\theta\right), \quad \tau_{z\theta} = \frac{E}{2(1+\nu)}\gamma_{z\theta}, \tag{2.2.5}$$

where ν is Poisson's ratio and $E = (1 + i\eta)E_{\text{real}}$ is the complex Young's modulus accounting for damping by including the material loss factor η. The normal and shear stresses are those shown in Figure 2.1(b). The equations of motion for a thin, isotropic and homogeneous shell of constant thickness in terms of its stresses are [3],

$$\frac{\partial \sigma_z}{\partial z} + \frac{1}{r}\frac{\partial \tau_{z\theta}}{\partial \theta} + \frac{\partial \tau_{zr}}{\partial r} + \frac{\tau_{zr}}{r} = \rho_s \frac{\partial^2 u}{\partial t^2}, \tag{2.2.6}$$

$$\frac{\partial \tau_{z\theta}}{\partial z} + \frac{1}{r}\frac{\partial \sigma_\theta}{\partial \theta} + \frac{\partial \tau_{\theta r}}{\partial r} + \frac{2\tau_{\theta r}}{r} = \rho_s \frac{\partial^2 v}{\partial t^2}, \tag{2.2.7}$$

$$\frac{\partial \tau_{rz}}{\partial z} + \frac{1}{r}\frac{\partial \tau_{r\theta}}{\partial \theta} + \frac{\partial \sigma_r}{\partial r} + \frac{\sigma_r - \sigma_\theta}{r} = \rho_s \frac{\partial^2 w}{\partial t^2}, \tag{2.2.8}$$

where the coupling stresses are neglected to ensure symmetry of the stress tensors ($\tau_{\theta r} = \tau_{r\theta}$). The equations of motion can also be described in terms of its force N, Q and moment M resultants [3, 16] shown in Figure 2.1(c),

$$\frac{\partial N_z}{\partial z} + \frac{1}{a}\frac{\partial N_{z\theta}}{\partial \theta} = \rho_s h \frac{\partial^2 u_0}{\partial t^2}, \tag{2.2.9}$$

$$\frac{\partial N_{\theta z}}{\partial z} + \frac{1}{a}\frac{\partial N_\theta}{\partial \theta}\frac{Q_\theta}{a} = \rho_s h \frac{\partial^2 v_0}{\partial t^2}, \tag{2.2.10}$$

$$\frac{a_i}{a} p^i(r = a_i) - \frac{a_e}{a} p^e(r = a_e) + \frac{\partial Q_z}{\partial z} + \frac{1}{a}\frac{\partial Q_\theta}{\partial \theta} - \frac{N_\theta}{a} = \rho_s h \frac{\partial^2 w_0}{\partial t^2}, \tag{2.2.11}$$

$$\frac{\partial M_z}{\partial z} + \frac{1}{a}\frac{\partial M_z}{\partial \theta} = -Q_z, \quad \frac{\partial M_{z\theta}}{\partial z} + \frac{1}{a}\frac{\partial M_\theta}{\partial \theta} = -Q_\theta, \tag{2.2.12}$$

where the resultants are calculated by integration of the stresses across the shell thickness. The integral is evaluated differently for the various shell theories as a result of the chosen simplifying assumptions.

The simplest equations of motion are those of Donnell-Mushtari [14],

$$\frac{\partial^2 u}{\partial z^2} + \frac{1-\nu}{2a^2}\frac{\partial^2 u}{\partial \theta^2} + \frac{1+\nu}{2a}\frac{\partial^2 v}{\partial z \partial \theta} + \frac{v}{a}\frac{\partial w}{\partial z} - \frac{1}{c_p^2}\frac{\partial^2 u}{\partial t^2} = 0, \tag{2.2.13}$$

$$\frac{1+\nu}{2a}\frac{\partial^2 u}{\partial z \partial \theta} + \frac{1-\nu}{2}\frac{\partial^2 v}{\partial z^2} + \frac{1}{a^2}\frac{\partial^2 v}{\partial \theta^2} + \frac{1}{a}\frac{\partial w}{\partial \theta} - \frac{1}{c_p^2}\frac{\partial^2 v}{\partial t^2} = 0, \tag{2.2.14}$$

$$\frac{v}{a}\frac{\partial u}{\partial z} + \frac{1}{a^2}\frac{\partial v}{\partial \theta} + \frac{w}{a^2} + \beta^2\left(a^2\frac{\partial^4 w}{\partial z^4} + 2\frac{\partial^4 w}{\partial z^2 \partial \theta^2} + \frac{1}{a^2}\frac{\partial^4 w}{\partial \theta^4}\right) + \frac{1}{c_p^2}\frac{\partial^2 w}{\partial t^2} - \frac{p_a(1-\nu^2)}{Eh} = 0, \tag{2.2.15}$$

where the remaining thin shell theories can be viewed as alterations to the Donnell-Mushtari formulation. Leissa [14] presents the equations of motion for a cylindrical shell

in matrix form as

$$[\mathcal{L}]\begin{bmatrix} \mathrm{u} \\ \mathrm{v} \\ \mathrm{w} \end{bmatrix} = \{0\}, \tag{2.2.16}$$

where $[\mathcal{L}]$ is the sum of the differential operator according to Donnell-Mushtari theory and a "modifying" operator multiplied by β^2,

$$[\mathcal{L}] = [\mathcal{L}_{D-M}] + \beta^2 [\mathcal{L}_{MOD}] \tag{2.2.17}$$

so that the other thin shell theories can be found by altering the elements of the Donnell-Mushtari operator by terms proportional to β^2, which will be more important for pipes with larger h/R ratios but still within the constraints of the thin shell assumptions.

Therefore, the equations of motion for small displacements of a thin circular cylindrical shell are determined from the stress and strains the shell material undergoes, and the resulting forces and moments. Unlike the motion of a plate in which the normal motion is independent of the in-plane motion, the curvature of a cylindrical shell induces coupling between the membrane and bending motion.

2.2.2 Fluid motion

The components of fluid displacement, $\boldsymbol{\xi} = (\xi_r, \xi_\theta, \xi_z)$, in a homogeneous, compressible fluid, with density ρ_f, must satisfy the linearized equation of continuity [17],

$$\frac{\partial \rho_f}{\partial t} + \nabla \cdot \rho_f \frac{\partial \boldsymbol{\xi}}{\partial t} = 0, \tag{2.2.18}$$

which defines the relationship between particle velocity and fluid density. For small amplitude displacement, in the absence of sources, the fluid must also satisfy the linear Euler's equation,

$$\rho_f \frac{\partial \boldsymbol{\xi}}{\partial t} = -\nabla p \tag{2.2.19}$$

relating fluid acoustic pressure p and particle velocity. The thermodynamic behavior of the fluid is defined by the equation of state,

$$\frac{\partial \rho_f}{\partial p} = \frac{\rho_f}{\mathcal{B}} \tag{2.2.20}$$

where $\mathcal{B} = \rho_f c_f^2$ is the fluid bulk modulus and c_f is the speed of sound in the fluid. Equations (2.2.18), (2.2.19), (2.2.20) are the three linear equations that govern fluid motion. Taking the time derivative of Equation (2.2.18) and the divergence of Equation (2.2.19) and defining ρ_f in terms of p from the equation of state, leads to the linear wave equation for the acoustic pressure [17],

$$\nabla^2 p = \frac{1}{c_f^2} \frac{\partial^2 p}{\partial t^2}. \tag{2.2.21}$$

For a cylindrical waveguide, the wave equation can be expressed in cylindrical coordinates as [17],

$$\left(\frac{\partial^2}{\partial r^2} + \frac{1}{r} \frac{\partial}{\partial r} + \frac{1}{r^2} \frac{\partial^2}{\partial \theta^2} + \frac{\partial^2}{\partial x^2} \right) p = \frac{1}{c_f^2} \frac{\partial^2 p}{\partial t^2}. \tag{2.2.22}$$

To find the solution to the fluid acoustic pressure p, assume harmonic solutions and separation of variables,

$$p(r,\theta,z,t) = \mathbf{R}(r)\mathbf{\Theta}(\theta)\mathbf{Z}(z)e^{i\omega t}, \tag{2.2.23}$$

which results in the four independent equations [17],

$$\frac{d^2\mathbf{R}}{dr^2} + \frac{1}{r}\frac{d\mathbf{R}}{dr} + \left(k_r^2 - \frac{m^2}{r^2}\right)\mathbf{R} = 0, \tag{2.2.24}$$

$$\frac{d^2\mathbf{Z}}{dz^2} + k_z^2\mathbf{Z} = 0, \tag{2.2.25}$$

$$\frac{d^2\mathbf{\Theta}}{d\theta^2} + n^2\mathbf{\Theta} = 0, \tag{2.2.26}$$

$$(\omega/c)^2 = k^2 = k_r^2 + k_z^2, \tag{2.2.27}$$

where k and k_z are the acoustic and axial wavenumbers respectively. The solutions to Equations (2.2.25) and (2.2.26) are simply

$$\mathbf{Z} = \left\{ \begin{array}{c} e^{ik_z z} \\ \\ e^{-ik_z z} \end{array} \right\} \quad \text{and} \quad \mathbf{\Theta} = \left\{ \begin{array}{c} e^{in\theta} \\ \\ e^{-in\theta} \end{array} \right\}. \tag{2.2.28}$$

The solution to Equation (2.2.24) is,

$$\mathbf{R} = \left\{ \begin{array}{c} J_n\left(k_r r\right) \\ \\ N_n\left(k_r r\right) \end{array} \right\}, \tag{2.2.29}$$

where J_n and N_n are the ordinary Bessel and Neumann functions respectively and n is the mode order. Therefore, the general solution to the wave equation for a duct of

circular cross section is,

$$p(r,\theta,z,t) = P_n \left\{ \begin{array}{c} J_n(k_r r) \\ N_n(k_r r) \end{array} \right\} \left\{ \begin{array}{c} e^{in\theta} \\ e^{-in\theta} \end{array} \right\} \left\{ \begin{array}{c} e^{ik_z z} \\ e^{-ik_z z} \end{array} \right\} \left\{ \begin{array}{c} e^{i\omega t} \\ e^{-i\omega t} \end{array} \right\}, \tag{2.2.30}$$

resulting from the separable solutions of the Helmholtz equation as derived above. For the circular cylindrical waveguide, the Neumann function is discarded because it diverges for a vanishing argument and does not satisfy a finite solution at $r = 0$. The pressure field is then defined as,

$$p(r,\theta,z,t) = P_n J_n(k_r r) \left\{ \begin{array}{c} e^{in\theta} \\ e^{-in\theta} \end{array} \right\} \left\{ \begin{array}{c} e^{ik_z z} \\ e^{-ik_z z} \end{array} \right\} e^{i\omega t}. \tag{2.2.31}$$

For uniform radiation, Morse [18] explains that both $k_z = 0$ and $n = 0$ represent outgoing waves in an axisymmetric tube. Uniform circumferential radiation is desired, yet the axial uniformity described by $k_z = 0$ is not satisfied for the frequency range of interest where $k_r^2 < k^2$. The axial wavenumber happens to be an important term in the coupled solution. Therefore, the pressure is simply,

$$p(r,z,t) = \left(P_{0+} e^{-ik_z z} + P_{0-} e^{ik_z z} \right) J_0(k_r r) e^{i\omega t} \tag{2.2.32}$$

where $n = 0$ implies an axisymetric solution and the pressure does not depend on circumferential position. The axial dependence is related to the propagating waves travelling in opposite directions with complex axial wavenumber k_z. The positive and negative going waves are denoted by the $+$ and $-$ sub-indices, respectively. For an "infinite" waveguide, there are no reflected waves and $P_{0-} = 0$. The solution to the amplitude P_0 is found by applying the boundary condition that requires continuity of the fluid and structure at

their interface.

2.2.3 Fluid structure interaction

The acoustic pressure pulsations of the contained fluid interact with the pipe structure and are therefore directly related to the radial shell motion. Euler's equation (or the momentum equation) [17],

$$\rho_f \frac{\partial w}{\partial t} + \frac{\partial p}{\partial r} = 0 \tag{2.2.33}$$

expresses the relationship between the radial velocity of the shell and the acoustic pressure of the fluid. Assuming time-harmonic dependence, Equation (2.2.33) can be restated as,

$$\frac{\partial p(r,z)}{\partial r} = i\omega\rho_f W(z), \tag{2.2.34}$$

where W is the radial displacement amplitude at axial position z. At the interface $r = a$, the motion must be equivalent. Applying this boundary condition to Equation (2.2.34),

$$\left.\frac{\partial p(r,z)}{\partial r}\right|_{r=a} = i\omega\rho_f W(z,\theta), \tag{2.2.35}$$

will lead to a solution for P_0 in Equation (2.2.32). Substituting Equation (2.2.32) into Equation (2.2.35) results in,

$$P_0 k_r J_0'(k_r a) = i\omega\rho_f W_0 \tag{2.2.36}$$

where P_0 and W_0 are the internal acoustic pressure amplitude and the radial displacement due to the $n = 0$ mode at a single axial position, respectively. W_0 has no circumferential

dependence, as the $n = 0$ motion is uniform around the circumference. Solving for the coefficient P_0,

$$P_0 = \frac{i\omega\rho_f W_0}{k_r J_0'(k_r a)}. \tag{2.2.37}$$

Substituting the solution for the coefficient P_0 into Equation (2.2.32) results in the exact solution to the pressure inside the pipe in terms of the pipe wall radial displacement, as shown in Equation (2.2.32):

$$P = \rho_f \omega^2 W_0 \frac{J_0\left(rk_r\right)}{k_r J_0'\left(ak_r\right)} \tag{2.2.38}$$

expressed in some texts [11] in terms of the specific acoustic impedance. If an infinite shell and plane wave motion in the fluid is assumed, Equation (2.2.38) will be axially uniform, having no axial dependence.

2.3 Modes of a pipe

The shell modes of the structure and the acoustic modes of its contained fluid are coupled. For a structure containing a light fluid such as gas, the waves will correspond to the uncoupled *in vacuo* shell waves and the rigid-walled duct acoustic waves. However, when the structure is filled with a heavy fluid such as oil or water, the modes of the fluid and structure are coupled. This section will review the uncoupled modes of an *in vacuo* cylindrical shell and those of the rigid-walled duct, and follow with an overview of the coupled modes of a fluid-filled cylindrical shell. The mode coupling depends largely on the axial phase speeds of the waveguide modes. Therefore, a solution to the axial phase speed will be derived. This section will end with a discussion of circumferential modal decomposition as a solution to extract distinct modal displacement amplitudes from the

total exterior motion of a shell.

2.3.1 Shell modes

The motion of the shell wall varies with axial position z and circumferential angle θ, and is defined in its simplest form as [11],

$$u, v, w = [U(z), V(z), W(z)] \cos(n\theta + \phi), \quad 0 \leq n \leq \infty \tag{2.3.1}$$

where n is the circumferential mode order (Figure 2.2) and ϕ is the polarization angle.

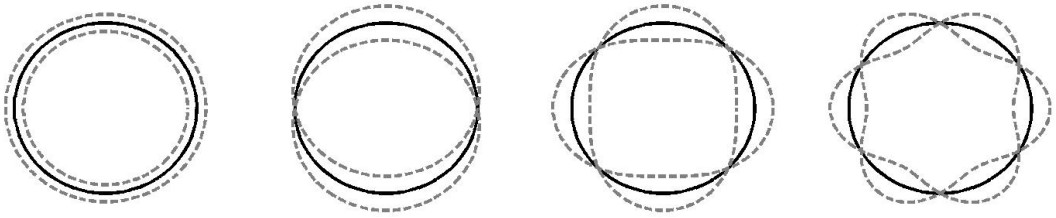

(a) $n = 0$ breathing mode (b) $n = 1$ bending mode (c) $n = 2$ ovaling mode (d) $n = 3$ mode

Figure 2.2. Cylindrical shell circumferential mode shapes.

The $n = 0$ breathing mode consists of uniform radial displacement and its motion is a result of the energy from the acoustic fluid propagating wave. Propagating waves will be discussed further in Section 2.4. Axial modes may occur for finite shells, however this review is limited to infinite cylindrical shells which have no axial dependence.

2.3.2 Acoustic modes

The pressure field inside a rigid walled cylinder varies with radial, axial and circumferential position. Again, assuming an infinite duct, we disregard axial modes. The circumferential modes are similar to those of a shell, with similar nodal lines. Yet, concentric circular pressure nodes will occur above the cut-on frequency of the first non-plane

wave mode. The cut-on frequency is dependent on the argument at which the derivative of the Bessel function goes to zero. The first point at which the derivative of the Bessel function is zero occurs when the argument is equal to 1.84, leading to an expression for the first cut-on [11],

$$\omega_{\text{cut-on}} = 1.84\frac{c_f}{a}, \tag{2.3.2}$$

where $\omega = 2\pi f$ is an angular frequency. The internal modes will occur in pairs, some of which are presented in Figure 2.3, where p denotes the radial mode order.

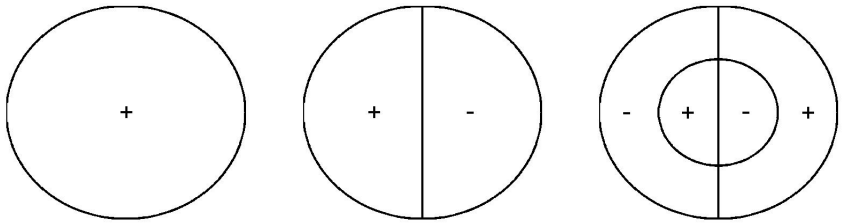

(a) $n = 0$,$p = 0$ (b) $n = 1$,$p = 0$ (c) $n = 1$,$p = 1$

Figure 2.3. Circumferential and radial nodal lines of interior duct modes

The formulations in this thesis are limited to plane-wave motion and therefore limited to a frequency range that lies below the cut-on of the first duct mode. These limitations guarantee that the pressure is uniform over the entire cross-section. Therefore, the pressure calculated at the interface of the fluid and structure is equivalent to the interior pressure, independent of radial position.

2.3.3 Coupling between shell modes and acoustic modes

The coupling between shell modes and acoustic modes is largely dependent on the axial phase speed, which takes into account the mass loading on the shell by the fluid. The

axial and circumferential wavenumbers are related by the expression,

$$k^2 = k_z^2 - k_r^2, \tag{2.3.3}$$

where k is the free acoustical wavenumber in the fluid. Pavic defines a non-dimensional axial wavenumber $\kappa = k_z a$, which are the "real solution of the dispersion equation"[9],

$$\det[\mathcal{L}] = 0 \tag{2.3.4}$$

where the matrix $[\mathcal{L}]$ is the differential operator in the cylindrical shell equations of motion (Equation (2.2.16)). Pavic [9] chooses to follow the thin shell theory developed by Flügge, where the elements of matrix $[\mathcal{L}]$ are,

$$\begin{aligned}
\mathcal{L}_{11} &= \kappa^2 + \left[\frac{(1-\nu)}{2}\right]\left(1+\beta^2\right)n^2 - \Omega^2, \\
\mathcal{L}_{12} &= \mathcal{L}_{21} = -\left[\frac{(1+\nu)}{2}\right]\kappa n, \\
\mathcal{L}_{13} &= \mathcal{L}_{31} = -\nu\kappa - \beta^2\kappa\left[\kappa^2 - \left\{\frac{(1-\nu)}{2}\right\}n^2\right], \\
\mathcal{L}_{22} &= n^2 + \left[\frac{(1-\nu)}{2}\right]\left(1+\beta^2\right)\kappa^2 - \Omega^2, \\
\mathcal{L}_{23} &= \mathcal{L}_{32} = n + \left[\frac{(3-\nu)}{2}\right]\beta^2 n\kappa^2, \\
\mathcal{L}_{33} &= 1 - \Omega^2 - Fl + \beta^2\left[1 - 2n^2 + \left(\kappa^2 + n^2\right)^2\right],
\end{aligned} \tag{2.3.5}$$

and where Fl is the internal fluid-loading term accounting for the effect of mass loading by the fluid on the structure. For applications in which the internal fluid is significantly heavier than the exterior fluid (such as a water filled pipe), the exterior fluid-loading can be neglected as it will be much smaller than the internal fluid-loading. For the longitudinal and acoustical components corresponding to the $n = 0$ breathing mode, the

fluid-loading is [9],

$$Fl_{l,a} = -\frac{\rho_f}{\rho_s}\frac{a}{h}\frac{2}{\psi - \zeta_{l,a}^2}, \tag{2.3.6}$$

where the non-dimensional constant $\psi = (c_s/c_f)^2$ is a ratio of the sound speed in the shell to the sound speed in the fluid. The variable ζ is a function of the non-dimensional wavenumber, which varies for the longitudinal and acoustical wavetypes,

$$\zeta_l = (1+\Delta)^{1/2} \quad \text{and} \quad \zeta_a = \left[\psi + \left(2(\rho_f/\rho_s)(a/h) + \nu^2\right) / \left(1-\nu^2\right)\right]^{1/2}, \tag{2.3.7}$$

where $\Delta = \nu^2(\psi - 1) / \left[(\psi-1)\left(1-\nu^2\right) + 2(\rho_f/\rho_s)(a/h) + \nu^2\right]$. The expression for the flexural component of fluid-loading, corresponding to the $n = 1$ bending mode, is [9]

$$Fl_b = \Omega^2 \frac{\rho_f}{\rho_s}\frac{a}{h}. \tag{2.3.8}$$

The axial phase speed c_z is determined from the expression for the acoustical axial wavenumber, $\kappa_a = k_z a = \zeta_a \Omega$ as follows,

$$k_z a = \left[\left(\frac{c_s}{c_f}\right)^2 + \frac{2(\rho_f/\rho_s)(a/h) + \nu^2}{1-\nu^2}\right]^{1/2} \frac{\omega}{c_s/a} \tag{2.3.9a}$$

$$\frac{c_s}{c_z} = \left[1 + \frac{2(\rho_f/\rho_s)(a/h) + \nu^2}{1-\nu^2}\left(\frac{c_s}{c_f}\right)^2\right]^{1/2} \tag{2.3.9b}$$

$$c_z = c_s\left[1 + \frac{2(\rho_f/\rho_s)(a/h) + \nu^2}{1-\nu^2}\left(\frac{c_s}{c_f}\right)^2\right]^{-1/2}. \tag{2.3.9c}$$

Some texts [13, 19] will define the axial phase speed as

$$c_z = c_s\left[1 + \frac{2\rho_f a}{\rho_s h}\left(\frac{c_s}{c_f}\right)^2\right]^{-1/2}, \tag{2.3.10}$$

assuming ν^2 is negligible. The choice to disregard Poisson's ratio depends on the material properties of the pipe and whether ν^2 is small enough to have a negligible effect on the axial phase speed calculation. However, both equations include the density and speed in both the structure and fluid, coupling the two systems.

2.3.4 Circumferential modal decomposition

The complicated circumferential motion of a pipe can be expressed as a sum of the individual vibrational modes. However, when calculating the internal acoustic pressure from Equation (2.2.38), only uniform radial motion corresponding to the $n = 0$ breathing mode is desired. Therefore, it is necessary to extract the character of the $n = 0$ mode from the total motion of the pipe. Methods for separating the modes of vibration take advantage of the circumferential spatial harmonic motion that results due to the axisymmetric and uniform nature of a pipe.

Circumferential modal decomposition techniques rely on harmonic analysis, where the amplitudes of each vibrational mode are a sum of the fundamental harmonic components. Harmonic analysis is a general term that includes the subject of Fourier analysis. Therefore, the basis of harmonic analysis starts with an understanding of the Fourier series [17],

$$f(x) = \frac{a_0}{2} + \sum_{n=1}^{\infty} [a_n \cos(nx) + b_n \sin(nx)], \tag{2.3.11}$$

which describes the way a periodic complex function $f(x)$ can be expressed as a superposition of sinusoidal waves. The exponential form is,

$$f(x) = \sum_{n=-\infty}^{\infty} c_n e^{inx}, \tag{2.3.12}$$

where a_n and b_n are the sum and difference of the positive and negative n components of c,

$$a_n = c_n + c_{-n} \tag{2.3.13}$$

$$b_n = i(c_n - c_{-n}). \tag{2.3.14}$$

Performing a Fourier transform decomposes the function $f(x)$ into its fourier coefficients,

$$c_n = \frac{1}{2\pi} \int_{-\pi}^{\pi} f(x) e^{-inx} dx. \tag{2.3.15}$$

The coefficients a_n and b_n can also be found directly by,

$$a_n = \frac{1}{\pi} \int_{-\pi}^{\pi} f(x) \cos(nx) dx, \tag{2.3.16}$$

$$b_n = \frac{1}{\pi} \int_{-\pi}^{\pi} f(x) \sin(nx) dx. \tag{2.3.17}$$

When constructing a model or performing analysis of measurements, it is more practical to define a discrete Fourier transform,

$$f_n = \frac{1}{N} \sum_{x=0}^{N-1} f_x e^{-2\pi inx/N}, \tag{2.3.18}$$

where n and x range from 0 to N-1. The discrete Fourier transform results in the two sided spectrum f_n, and the one sided spectrum is evaluated by summing the corresponding positive and negative components of n. Therefore, the number of sampling points N is directly related to the number of modes n by the Nyquist-Shannon theorem. The number of sampling points N should be greater or equal to $2\mathcal{N} + 1$, where $\mathcal{N}$ is the highest mode order that can be extracted. If higher order modes than $\mathcal{N}$ are present,

aliasing will occur and the number of sampling points should be increased.

In the case of extracting the circumferential vibrational modes of a pipe, n will correspond to the mode order and the sampling and summation is performed over the circumferential coordinate θ, yielding a spatial fourier transform. When performing modal analysis, using an input force to a structure and measuring the acceleration at N circumferential positions, it is common to work with FRF's (frequency response functions) [20],

$$H_{xy}(f) = \frac{G_{xy}(f)}{G_{xx}(f)}, \tag{2.3.19}$$

where

$$G_{xy} = \overline{X^*(f)Y(f)}, \tag{2.3.20}$$

and X and Y are the force and acceleration linear spectrums. In the case of operational data, when the input force is not measured, an arbitrary sensor in the circumferential ring can be chosen as the reference. Bonness, Fahnline and Jenkins [21] developed a wavenumber decomposition technique which extracts the Fourier coefficients using the provided FRF, scaled by $|G_{xx}|^{1/2}$ or an average of $|G_{xy}|^{1/2}$ to give the FRF spectral character. A discrete spatial Fourier Transform (DFT) of the scaled H_{xy} is taken at each frequency as in Equation (2.3.18). The total energy is computed by summing the energy of the corresponding positive and negative components of H_n.

If the input force is unknown, computing the linear spectrum at each circumferential position is sufficient to perform the modal analysis. Furthermore, if the only mode of interest is the breathing mode, it is possible to extract it in the time domain as well as the frequency domain. The discrete Fourier transform from Equation (2.3.18) for $n = 0$

is simply,

$$f_0 = \frac{1}{N} \sum_{x=0}^{N-1} f_x, \tag{2.3.21}$$

where f_0 is the average of f_x over all sampling points. In the frequency domain, modal analysis depends on the difference in-phase between the different circumferential positions. In the time domain, the difference in-phase is exhibited by the corresponding positive and negative displacements for mode orders higher than zero. Therefore, a circumferential average at each time sample yields only the uniform displacement corresponding to the $n = 0$ breathing motion. Therefore, for the $n = 0$ breathing mode, the circumferential modal decomposition can be performed in the frequency domain or time domain. However, if higher order modes are desired for analysis, it is necessary to compute the wavenumbers in the frequency domain.

2.4 Wave propagation in a fluid-filled pipe

The only mode of concern in determining the internal acoustic pressure from normal surface vibrations is the $n = 0$ breathing mode, assuming it is dominated by the energy from the acoustical propagating wave in the fluid. However, the radial motion has components corresponding to the longitudinal and flexural propagating waves as well as the acoustical propagating wave. Therefore, the existence of other propagating waves in the system must be taken into account, as they may interfere with measurements of the desired quantity. The following section defines the propagating waves of interest and their role in the equations of displacement for the three orthogonal directions of motion. The displacement can be calculated at any position on the pipe by using energies corresponding to the different propagating wave-types to be discussed.

2.4.1 Propagating waves

There are four propagating waves that exist in the fluid/structure system at relatively low frequencies $\Omega << 1$, which have been studied in-depth by Pavic [9] and Fuller and Fahy [22]. The frequency will be described by the relative frequency, $\Omega = \omega/\omega_r$, where $\omega_r = c_s/a$ is the ring frequency and $c_s = \sqrt{E/\rho_s(1-\nu^2)}$ is the speed of sound in the structure. The frequency range of interest corresponds to the frequencies much below the ring frequency, where only the $n = 0$ and $n = 1$ modes allow wave propagation without spatial attenuation. The four propagating waves are called the longitudinal (compression), acoustical, torsional and flexural waves. Other waves exist, such as evanescent and quasi-propagating waves, yet these waves decay exponentially from the extremities of the pipe and therefore are assumed to be negligible far from discontinuities. Of the four propagating waves studied, the longitudinal, acoustical, and torsional are related to the desired $n = 0$ breathing mode of the pipe's surface and the flexural waves are related to the $n = 1$ bending mode. The following analytical development disregards higher order modes because the frequency range of interest is below the frequency of the second cut-on, where the cut-on can be evaluated approximately by,

$$\Omega^2_{\text{cut-on}} = \frac{\beta^2 n^2 (n^2-1)^2}{1 + n^2(1+\nu/n) + \beta^2(n^2-1)^2} \tag{2.4.1}$$

found by Pavic [9], where ν is Poisson's ratio of the shell material and n is the circumferential mode.

2.4.2 Displacement equations

The three orthogonal components of pipe motion, axial, tangential and radial (shown in Figure 2.1(a)), can be described in terms of the four propagating waves in the following

equations given by Pavic [9]:

$$\begin{aligned}\mathbf{u} =& iU_{l+}\mu_{l+} + iU_{l-}\mu_{l-} + iU_{a+}\mu_{a+} + iU_{a-}\mu_{a-} \\ &+ iU_{b+}\mu_{b+}\cos\alpha_+ + iU_{b-}\mu_{b-}\cos\alpha_-, \qquad (2.4.2a)\end{aligned}$$

$$\mathbf{v} = V_{t+}\mu_{t+} + V_{t-}\mu_{t-} + V_{b+}\mu_{b+}\sin\alpha_+ + V_{b-}\mu_{b-}\sin\alpha_-, \qquad (2.4.2b)$$

$$\begin{aligned}\mathbf{w} =& W_{l+}\mu_{l+} + W_{l-}\mu_{l-} + W_{a+}\mu_{a+} + W_{a-}\mu_{a-} \\ &+ W_{b+}\mu_{b+}\cos\alpha_+ + W_{b-}\mu_{b-}\cos\alpha_-, \qquad (2.4.2c)\end{aligned}$$

where μ is the propagation factor,

$$\mu_{q\pm} = \exp(\mp i\kappa_q z/a + i\phi_{q\pm}), \quad q = l, a, t, b \qquad (2.4.3)$$

and where ϕ is the phase angle and α corresponds to the polarization of the bending waves, $\alpha_\pm = \theta - \gamma_\pm$. The non-dimensional axial wavenumbers are,

$$\begin{aligned}&\kappa_l \simeq \zeta_l\Omega, && \text{with } \zeta_l = (1+\Delta)^{1/2}, \\ &\kappa_a \simeq \zeta_a\Omega, && \text{with } \zeta_a = \left[\psi + \left(2\eta + \nu^2\right)/\left(1-\nu^2\right)\right]^{1/2}, \\ &\kappa_t = \zeta_t\Omega, && \text{with } \zeta_t = \left[2/\left(1-\nu\right)\right]^{1/2}, \\ &\kappa_b \simeq \zeta_b\sqrt{\Omega}, && \text{with } \zeta_b = (2+\eta)^{1/4},\end{aligned} \qquad (2.4.4)$$

with constants,

$$\psi = \left(\frac{c_s}{c_f}\right)^2, \quad \eta = \left(\frac{\rho_f}{\rho_s}\right)\left(\frac{a}{h}\right), \quad \Delta = \frac{\nu^2\left(\psi-1\right)}{\left[\left(\psi-1\right)\left(1-\nu^2\right)+2\eta+\nu^2\right]}. \qquad (2.4.5)$$

The complex quantities **u**,**v**, and **w** correspond to the axial, tangential and radial displacements respectively and the wave amplitudes U, V, and W are real quantities. Gen-

eral equations of motion can be expressed as:

$$\mathbf{u} = U(z)\cos(n\alpha) \tag{2.4.6a}$$

$$\mathbf{v} = V(z)\sin(n\alpha) \tag{2.4.6b}$$

$$\mathbf{w} = W(z)\cos(n\alpha) \tag{2.4.6c}$$

and are cited in many textbooks [11, 13]. This development expresses the real wave amplitudes in terms of the propagating wave components,

$$U = iU_{l+}\mu_{l+} + iU_{l-}\mu_{l-} + iU_{a+}\mu_{a+} + iU_{a-}\mu_{a-} + jU_{b+}\mu_{b+} + iU_{b-}\mu_{b-}, \tag{2.4.7a}$$

$$V = V_{t+}\mu_{t+} + V_{t-}\mu_{t-} + V_{b+}\mu_{b+} + iU_{b-}\mu_{b-}, \tag{2.4.7b}$$

$$W = W_{l+}\mu_{l+} + W_{l-}\mu_{l-} + W_{a+}\mu_{a+} + W_{a-}\mu_{a-} + W_{b+}\mu_{b+} + W_{b-}\mu_{b-}. \tag{2.4.7c}$$

The radial displacement is a sum of the displacements contributed by the longitudinal, acoustical and flexural propagating waves, as seen in Equation (2.4.2c). It should be noted that the radial displacement amplitude W_0 in Equation (2.2.38) assumes that the acoustical component of radial displacement W_a dominates the total radial motion in W_0. Section 2.3.4 described the technique for extracting the $n = 0$ mode from the radial motion, which would cancel the bending wave components of radial displacement. Yet Equation (2.4.2c) shows that the $n = 0$ radial motion will still be composed of contributions by the energy from the longitudinal propagating wave as well as the acoustical propagating wave. As long as W_l is negligible compared to W_a, then $W \approx W_0$. The ratio of energies in the acoustic and longitudinal propagating waves that ensures $W \approx W_0$ will be examined in Chapter 3.

2.4.3 Energy flow

The energy flow factors from each propagating wave provide a powerful analytical tool for reconstructing pipe motion. Energy flow factors are described in terms of the known wave amplitudes of pipe motion by Pavic [9]. Yet, the energy flow expressions can be used to deduce the wave amplitudes.

There are sixteen unknown wave amplitudes, including the positive and negative components, that describe the total pipe motion. Using the reflection coefficients, the negative going wave amplitude can be described in terms of its positive-going wave amplitude. For example the displacement amplitude U_{l-} can be defined as $U_{l-} = r_l U_{l+}$ where r_l is the reflection coefficient in the longitudinal wave type. Pavic [9] also describes the relationships between the wave amplitudes,

$$U_{l\pm} = \mp\Gamma_l/\Omega W_{l\pm}, \quad U_{a\pm} = \mp\Gamma_a/\Omega W_{a\pm}, \quad U_{b\pm} = \pm\zeta_b\sqrt{\Omega}W_{b\pm}, \quad V_{b\pm} = -W_{b\pm}, \quad (2.4.8)$$

where $\Gamma_q = \nu\zeta_q/(\zeta_q^2-1)$ can be readily obtained using the formulae derived from the exact coupled solution for fluid-loading. With these relationships, we can reduce the amount of unknown wave amplitudes to four, U_{l+}, U_{a+}, W_{b+} and V_{t+}. The equations used to solve for these unknown variables come from the extensional, flexural, and curvature-dependent energy flow factors:

$$\begin{aligned} < \Lambda_e >_{y,x} = (\omega/2a) \big\{ & \kappa_l(U_{l+}^2 - U_{l-}^2) + \kappa_a(U_{a+}^2 - U_{a-}^2) + ((1-\nu)/2)\kappa_t(V_{t+}^2 - V_{t-}^2) \\ & + (\kappa_b/2)\left[(U_{b+}^2 - U_{b-}^2) + ((1-\nu)/2)(V_{b+}^2 - V_{b-}^2)\right] \\ & + ((1+\nu)/4)(U_{b+}V_{b+} + U_{b-}V_{b-})\big\} \end{aligned} \quad (2.4.9a)$$

$$\begin{aligned} < \Lambda_f >_{y,x} = (\omega/a)\beta^2 \big[& \kappa_l^3(W_{l+}^2 - W_{l-}^2) + \kappa_a^3(W_{a+}^2 - W_{a-}^2) \\ & + \kappa_b((1+\kappa_b^2)/2)(W_{b+}^2 - W_{b-}^2)\big] \end{aligned} \quad (2.4.9b)$$

$$< \Lambda_c >_{y,x} = (\omega/2a)\left[\nu\left\{(1+\beta^2)\left[(U_{l+}W_{l+} + U_{l-}W_{l-}) + (U_{a+}W_{a+} + U_{a-}W_{a-})\right]\right.\right.$$
$$\left.\left. + \frac{1}{2}\left[1 - \beta^2((1-\nu)/\nu)\right](U_{b+}W_{b+} + U_{b-}W_{b-})\right\}\right.$$
$$\left. + \beta^2\{...\}\right], \tag{2.4.9c}$$

where "the terms containing β^2 can be neglected in comparison to unity" since $\beta^2 << 1$ [9]. Grouping the terms from each wave-type provides four equations describing the four flow factors in each propagating wave component. Using the reflection coefficients and relationships between displacement amplitudes leads to the four following wave amplitude equations,

$$U_{l+}^2 = \Lambda_l(a/\omega)\left[\frac{1}{2}\kappa_l(1-|r_l|^2) + \beta^2\kappa_l^3(\Omega/\Gamma_l)^2(1-|r_l|^2)\right. \tag{2.4.10a}$$
$$\left. + \frac{1}{2}\nu(1+\beta^2)(-\Omega/\Gamma_l)(1+|r_l|^2)\right]^{-1}$$
$$U_{a+}^2 = \Lambda_a(a/\omega)\left[\frac{1}{2}\kappa_a(1-|r_a|^2) + \beta^2\kappa_a^3(\Omega/\Gamma_a)^2(1-|r_a|^2)\right. \tag{2.4.10b}$$
$$\left. + \frac{1}{2}\nu(1+\beta^2)(-\Omega/\Gamma_a)(1-|r_a|^2)\right]^{-1}$$
$$W_{b+}^2 = \Lambda_b(a/\omega)\left[\frac{1}{4}\kappa_b(\zeta_b\sqrt{\Omega})^2(1-|r_b|^2) + \frac{1}{4}\kappa_b((1-\nu)/2)(1-|r_b|^2)\right. \tag{2.4.10c}$$
$$+ \frac{1}{2}((1-\nu)/4)(1+|r_b|^2) + \beta^2\kappa_b((1+\kappa_b^2)/2)(1-|r_b|^2)$$
$$\left. + \frac{1}{4}\nu\beta^2((1-\nu)/\nu)(\zeta_b\sqrt{\Omega})(1+|r_b|^2)\right]^{-1}$$
$$V_{t+}^2 = \Lambda_t(2a/\omega)\left[((1-\nu)/2)\kappa_t(1-|r_t|)\right]^{-1}. \tag{2.4.10d}$$

So, if the four components of energy flow Λ_l, Λ_a, Λ_b, and Λ_t are defined, it is possible to reconstruct the entire pipe motion at any point on the pipe.

2.5 Simplified expression for pressure

The relationship between the internal acoustic pipe pressure and the velocity normal to the pipe's surface is expressed in Equation (2.2.38) and its derivation was presented in section 2.2. This expression represents an exact solution if W is the radial displacement due to the acoustical energy in the $n = 0$ breathing mode. With Equation (2.4.2c), the acoustical component of radial displacement is known and the exact pressure can be computed. In cases where only the total radial displacement is known, circumferential modal decomposition can be used to extract the $n = 0$ component of vibration, but this will not ensure a purely acoustical radial displacement value. This section will present a simplification to Equation (2.2.38) using a series solution of Bessel functions. Another equation for pressure will be developed based on the simplified solution for theoretical cases when the three components of radial displacement (acoustical, longitudinal, bending) are known. An additional derivation of the simplified expression will be presented using the hoop strain and stress of the pipe. The simplified expression for pressure not only provides a link to the theoretical expression for pressure, but it is also valuable in decreasing computer time when running complex models to determine the pipe motion.

2.5.1 Series solution to Bessel function and the Fluid-loading term

The series solution of the Bessel function [19] is

$$J_n(x) = \sum_{k=0}^{\infty} \frac{(-1)^k}{k!(k+n)!} \left(\frac{x}{2}\right)^{n+2k} \tag{2.5.1}$$

where the first approximation is $J_0(x) \approx 1$ and $J_0'(x) = -J_1(x) \approx x/2$, and leads to the a simplification of Equation (2.2.38),

$$\frac{P}{\langle W \rangle} = \frac{\rho_f \omega^2}{k_r} \left(\frac{2}{k_r a} \right). \tag{2.5.2}$$

Furthermore, the radial frequency can be expressed in terms of the non-dimensional frequency $\omega^2 = \Omega^2 \omega_r^2 = \Omega^2 (c_s/a)^2$ and the radial wavenumber can be defined in terms of the normalized radial wavenumber as $k_r^2 = (\xi_a/a)^2$. Substituting the non-dimensional frequency and normalized radial wavenumber results in the ratio given by Pavic [9] for the acoustical pressure due to the fluid wavetype,

$$\frac{P}{\langle W \rangle} = \frac{2\rho_f c_s^2 \Omega^2}{(\xi_a^2 a)}, \tag{2.5.3}$$

where $\xi_a^2 = \psi\Omega^2 - \kappa_a^2$ is the normalized radial wavenumber, $\psi = (c_s/c_f)^2$ is a non-dimensional constant and $\kappa_a^2 \simeq \zeta_a \Omega$ is the normalized acoustic axial wavenumber. The acoustic impedance in Equation (2.5.3) can be redefined as the product of a pressure coefficient and a fluid-loading term,

$$\frac{P}{\langle W \rangle} = \frac{Eh}{a^2(1-\nu^2)} \left[-\frac{\rho_f}{\rho_s} \frac{a}{h} \frac{2}{\psi - \zeta^2} \right], \tag{2.5.4}$$

where the fluid-loading term is the expression in brackets. This equation assumes that the radial component of displacement is purely due to the acoustical mode. Yet, in an analytical model, it is possible to reconstruct the radial displacement contribution from each propagating wave. Therefore, the equation for pressure should reflect this. The calculation of internal pressure in the ideal case where the propagating wave contributions

are known is represented by,

$$P = \frac{Eh}{a^2(1-\nu^2)}\left[Fl_l w_l + Fl_a w_a + Fl_b w_b\right], \tag{2.5.5}$$

where the fluid-loading terms are described in terms of their corresponding wave-type, as shown in Equations (2.3.6) and (2.3.8). Although it is very difficult if not impossible to exactly measure the propagating wave radial displacement contributions, Equation (2.5.5) provides a powerful analytical tool in the comparison of a theoretical pressure to an 'approximate' pressure. The validity of an 'approximate' pressure prediction will be analyzed in Chapter 3.

2.5.2 Development from hoop strain and stress

If longitudinal pipe vibrations are neglected, Junger and Feit [13] provide a development of the relationship between internal fluid pressure and external surface vibrations through hoop strain ϵ and stress σ,

$$\epsilon = w/a \quad \text{and} \quad \sigma = \epsilon E/(1-\nu^2).$$

Using the equation $h\sigma = ap$ from static equilibrium theory, the pipe reactance is,

$$\frac{p}{w} = \frac{Eh}{a^2(1-\nu^2)}. \tag{2.5.6}$$

This solution is similar to Equation (2.5.5) if the fluid-loading term is discarded. If the fluid-loading is assumed to be sufficiently close to one, it could be discarded and the solutions would be similar. The decision to discard the fluid-loading term would depend on the material properties of the pipe.

CHAPTER 3

ANALYTICAL MODEL

3.1 Purpose

An analytical model is constructed to investigate the error introduced by several input parameters on the calculation of the fluid-borne acoustic pressure. The model simulates the motion of the pipe in the three orthogonal directions based on the subscribed input parameters. The error is then calculated as the absolute decibel (dB) difference between the values obtained from the approximate and theoretical expressions for pressure (Equations 2.5.4 and 2.5.5). The difference between pressures is used to asses the amount of error produced by specific parameters.

These input parameters are divided into two categories: those that are inherent to the piping system and those that stem from the measurement sensor inaccuracies or configuration. Assuming the sensors are to be placed on an existing piping system, the operator will have no control over the parameters that are inherent to the system. These parameters include the piping material and geometry, the fluid being transported,

and the propagating waves present in the system. The parameters that can be controlled include the characteristics of the sensor selected as well as how the sensors are configured. The input parameters required for this model are listed in Table 3.1.

Table 3.1. Parameters used to simulate pipe motion and measurement conditions.

Inherent Parameters	
Pipe material properties	Energy flow factors
(ρ_s, ν, E, η)	Reflection coefficients
Pipe dimensions (a, h, L)	Polarization of bending waves
Interior fluid properties (ρ, c_f)	Phase angles
Measurement Inaccuracy Parameters	
Accelerometer configuration	Transverse sensitivity of accelerometers

The first category of parameters provides insight into the challenges faced using the proposed method with accelerometers on different piping systems and varying energy inputs. Within the limits of the model, the geometry and material of the pipe, as well as the fluid it transports, will be varied to study the effect each of these parameters has on the prediction of pressure. The effect of varying the amplitudes of the four propagating wave energies will also be analyzed, where special attention will be given to the ratio of the acoustical to longitudinal wave energies in order to identify the limiting ratio whose error lies below an acceptable limit. The parameter of energy flow is rather intangible, so a more physical interpretation is introduced through the use of excitation vectors to produce case-specific examples of energy flow amplitudes.

Results from varying the parameters in the second category establishes the importance of carefully selecting and configuring the accelerometers. The proposed equally-spaced circumferential ring configuration of the accelerometers is expected to be sensitive to offsets in placement. The model will give an idea of how large the offset can be before the error becomes unacceptably large. The sensor characteristics will also have an impact on the accuracy of the measurements. It is possible to select accelerometers

with specific characteristics, such as low transverse-sensitivity and a low-noise floor at low frequencies. However, an accelerometer with more detailed specifications introduces a higher cost which is an important factor in industrial applications. The model will evaluate which specifications are most important for accurate measurements.

The ultimate objective of this model is to evaluate which conditions are conducive to the accurate prediction of internal pipe pressure using a ring of accelerometers. A number of assumptions are made within the model and will be discussed in the following sections as they pertain to each parameter. The following sections provide a more thorough discussion of the model formulation and organization, including definitions of each of the parameters and their placement within the model.

3.2 Simulating pipe motion

The displacement at any axial (x) and circumferential (θ) coordinate pair on the pipe is calculated for the three orthogonal directions of motion by the equations,

$$\begin{aligned}\mathbf{u} =& iU_{l+}\mu_{l+} + iU_{l-}\mu_{l-} + iU_{a+}\mu_{a+} + iU_{a-}\mu_{a-} \\ &+ iU_{b+}\mu_{b+}\cos\alpha_+ + iU_{b-}\mu_{b-}\cos\alpha_-, \qquad (3.2.1a)\end{aligned}$$

$$\mathbf{v} = V_{t+}\mu_{t+} + V_{t-}\mu_{t-} + V_{b+}\mu_{b+}\sin\alpha_+ + V_{b-}\mu_{b-}\sin\alpha_-, \qquad (3.2.1b)$$

$$\begin{aligned}\mathbf{w} =& W_{l+}\mu_{l+} + W_{l-}\mu_{l-} + W_{a+}\mu_{a+} + W_{a-}\mu_{a-} \\ &+ W_{b+}\mu_{b+}\cos\alpha_+ + W_{b-}\mu_{b-}\cos\alpha_-, \qquad (3.2.1c)\end{aligned}$$

given by Pavic [9] and previously described in Section 2.4.2, where an in-depth explanation is given. Once the piping system material, contained fluid, and geometry are defined, the motion is simulated by assigning the energy flow factors of the four propagating wave types. These four energy flow factors will in turn define the four positive-going real wave

amplitudes, U_{l+}, U_{a+}, V_{t+} and W_{b+}. Using the reflection coefficients to calculate the negative going wave amplitudes and the relationships described in Equations 2.4.8, the sixteen necessary real wave amplitudes are defined and the motion of the pipe's middle surface is described at any position.

3.2.1 Simulating measurement conditions

The radial motion measured by each accelerometer depends on its configuration as well as its assigned transverse sensitivity. Circumferential modal decomposition, used to extract the amplitude of the $n = 0$ breathing mode, requires that the measurement sensors are equally-spaced. If an accelerometer is offset, the radial motion it detects will also be offset, and the calculation of the $n = 0$ breathing mode amplitude will be incorrect. The imperfect placement of accelerometers is simulated by first defining the circumferential positions of the equally-spaced ring,

$$\theta = [0, 2\pi/N, 2(2\pi/N), 3(2\pi/N), ...(N-1)(2\pi/N)],$$

where N is the number of accelerometers. The incorrect positions are then calculated by adding the offset to specific accelerometer positions prescribed by a 'distribution' vector,

$$\theta_{offset} = \theta + \left[(offset/a). * \text{distribution})\right].$$

This model attempts to explain the amount of error introduced by the incorrect placement of the measurement accelerometers.

Another source of error stems from the sensor characteristics. All accelerometers are susceptible to some transverse sensitivity. This means that the radial motion detected by each accelerometer will contain some contribution from the axial and tangential displace-

ments in addition to the desired radial motion. The transverse sensitivity inaccuracy is calculated in the model as,

$$w_T = T * (u\cos(q) + v\sin(q))$$

where T is the transverse sensitivity given as a percentage (commonly less than 5%) and q is the angle between the pipe axis and the direction of maximum transverse sensitivity. The transverse displacement is added to the pure radial displacement to get the total displacement that would be measured by the accelerometers. Yet, this calculation is somewhat simplified since the same sensitivity T and angle q is applied to each accelerometer. More realistically, each accelerometer should have a different transverse sensitivity and different angle of maximum transverse sensitivity. This calculation is made to provide a more consistent model without having to introduce another random variable. This model will determine the sensitivity of the pressure prediction to the altered, simulated motion.

3.3 Determining the error

The error is determined by comparing a theoretical and approximate expression for pressure. The theoretical calculation of pressure takes advantage of the model's ability to separate the longitudinal, acoustical, and flexural components of radial motion by applying their corresponding fluid-loading terms,

$$P = \frac{Eh}{a^2(1-\nu^2)}\left[Fl_l w_l + Fl_a w_a + Fl_b w_b\right], \tag{3.3.1}$$

as explained previously in Section 2.5. The approximate expression for pressure mimics the calculation that will be made with operational data, where the components of radial

motion are not separable. Instead, the amplitude of the $n = 0$ breathing mode is extracted from the total radial motion to exclude the bending wave component. The remaining radial amplitude is assumed to be dominated by the acoustical propagating wave energy and so applying only the acoustical component of fluid-loading is sufficient,

$$\tilde{P} = \frac{Eh}{a^2(1-\nu^2)}\left[Fl_a w_0\right] = \frac{Eh}{a^2(1-\nu^2)}\left[-\frac{\rho_f}{\rho_s}\frac{a}{h}\frac{2}{\psi-\zeta^2}w_0\right]. \tag{3.3.2}$$

When the acoustical propagating wave is the only wave present, Equations (3.3.1) and (3.3.2) are equivalent, otherwise there is always a small difference between them. To simulate more realistic measurement conditions, the model is altered to include the measurement inaccuracies outlined in Table 3.1. The theoretical and approximate pressures are then compared to determine the error introduced by specific parameters.

3.4 Limitations of model

It should be noted that the 'theoretical' pressure calculations are based on an approximate model, which includes a number of assumptions and, in turn, limitations. As the approximate model is used as a comparison tool, it is important that the approximations are negligibly different from the exact solutions. The model presented here follows Pavic's [9] formulations, where he presents an error analysis that will be useful in defining the limitations.

The error is determined by the difference between the exact and approximate solutions to the wavenumbers κ_l,κ_a,κ_b, and κ_t. Pavic [9] focuses on the error of κ_b as it is a less accurate approximation than the other wavetypes. As expected, the error increases with frequency and the range should be limited to frequencies not only below the ring frequency, but also below the cut-on of the $n = 2$ circumferential mode. The error is also

sensitive to Poisson's ratio and pipe thickness. In all cases of different pipe materials, fluids, and geometries, the difference between the theoretical expression and the exact solution is negligible (below 0.2 dB) when restricted to low relative frequencies $\Omega \leq 0.1$. Therefore, the analysis presented here will be limited to frequencies below $\Omega = 0.1$.

3.5 Control parameters

The control input parameters are defined in this section and they attempt to mimic the system used for the experiments in Chapter 4, which is a six inch ($\approx$ 150 mm) diameter, Schedule 40 (7.1 mm) aluminum pipe filled with water. As the analysis is conducted by

Table 3.2. Control parameters for the analytical model.

Piping System			
Material (Aluminum)		Fluid (Water)	
material density	$\rho_s = 2700$ kg/m^3	fluid density	$\rho_f = 998$ kg/m^3
Poisson's ratio	$\nu = 0.33$	fluid sound speed	$c_f = 1481$ m/s
Young's modulus	$E = 6.9E10$		
Loss factor	$\eta = 0.01$		
Dimensions			
diameter	$d = 6$ in		
thickness	$h = 0.28$ in		

Propagating Wave Energy			
Energy flow factor	reflection coefficient	phase angle	polarization angle
$\Lambda_l = 1$	$r_l = 0$	$\phi_{l+} = 0$	
$\Lambda_a = 1$	$r_a = 0$	$\phi_{a+} = 0$	
$\Lambda_b = 1$	$r_b = 0$	$\phi_{b+} = 0$	$\theta_{\pm} = 0$
$\Lambda_t = 1$	$r_t = 0$	$\phi_{t+} = 0$	

Sensor specifications	
accelerometer position	$\theta = [0, 2\pi/N, 2(2\pi/N), 3(2\pi/N), ...(N-1)(2\pi/N)]$ where N is number of accelerometers
accelerometer transverse sensitivity	0%

varying parameters individually, it is necessary to define a set of parameters that remain constant in order to obtain a consistent comparison. These control input parameters

are outlined in Table 3.2. If a parameter is not being varied to study its effects on the pressure prediction, it's value will be the one assigned in Table 3.2.

Since the analysis of each parameter is evaluated in the presence of no other inaccuracies, the difference between the theoretical and approximate expressions for pressure should be less than the acceptable error allowed for experimental data. Therefore, the acceptable error for the purposes of this model will be 1dB when varying a single parameter, as the error is expected to increase if more inaccuracies are included.

3.6 Piping system parameters

The vibrations of a piping system in response to an excitation depend on its size, material and contained fluid. The following sections will discuss the results of varying each of these parameters, in terms of their effect on the surface displacements simulated by the model and the calculation of the internal acoustic pressure. Different sizes, materials and fluids are chosen that fit within the limitations of the model.

3.6.1 Piping dimensions

By definition, a pipe is a circular cylindrical shell and is therefore fully characterized by it's diameter and thickness. The consequence of making the pipe thicker is that the pipe wall will exhibit smaller vibrations. The reason for thicker walls in pipes most likely has more to do with their ability to withstand high internal pressures rather than noise isolation.

Increasing the thickness of the pipe wall, while keeping the diameter constant results in a decrease of radial displacement for the same energy input. Alternately, if the level of surface vibrations is similar for each case of thickness, the level of pressure will increase with an increase of thickness due to the fact that a higher internal pressure is required to

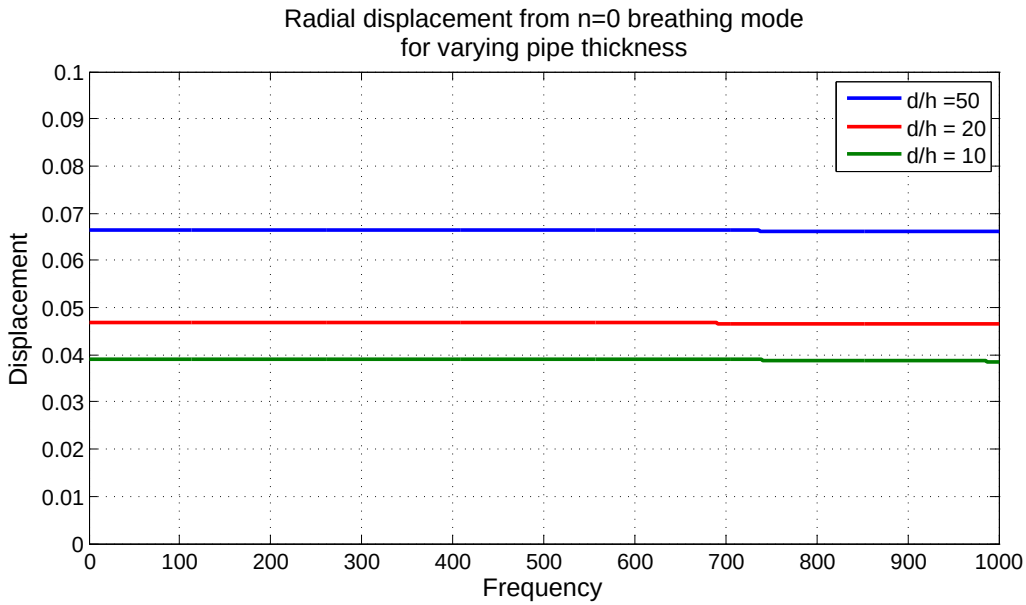

Figure 3.1. Response of pipe to varying thickness.

displace a thicker pipe wall by the same amount. This can also be seen in the calculation of pressure (Equation (3.3.1)), as it is proportional to the thickness.

The diameter and thickness go hand-in-hand and the ratio of the two is often given to characterize a piping system. Therefore, if the thickness is kept constant, an increase in diameter results in an increase in the surface vibrations because the pipe appears to be thinner relative to its diameter. The $n = 0$ radial displacement is shown in Figure 3.1 for varying diameter-to-thickness ratios.

Piping systems with smaller diameter-to-thickness ratios (larger thickness relative to its diameter) require accelerometers with low-noise floors in order to measure the small surface vibrations. This model confirms the results expected from changes in the pipe dimensions.

3.6.2 Pipe material

Two materials, aluminum and steel, were chosen to compare the effect of material parameters on radial displacement and pressure. As shown in Table 3.3, steel is more

Table 3.3. Material properties

material	density ρ_s [kg/m^3]	Poisson's ratio ν	Young's modulus E [Pa]	sound speed c_s [m/s]	ring freq ω_r [kHz]
aluminum	2700	0.33	7.1E10	5355	10.6
steel	7700	0.28	19.5E10	16577	32.7

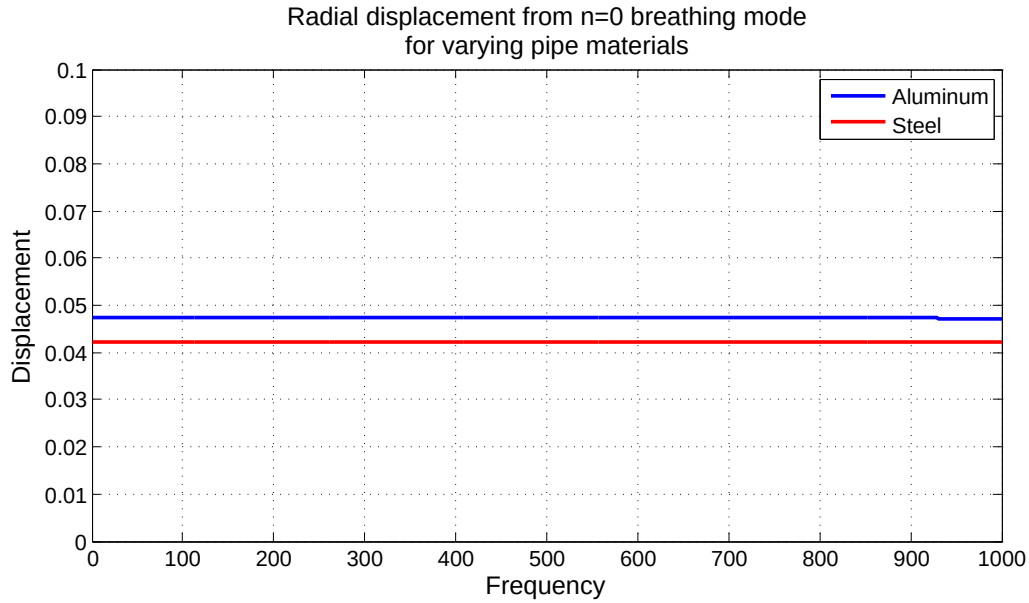

Figure 3.2. Response of pipe to varying materials.

dense and more stiff than aluminum. A denser and stiffer material such as steel will be more difficult to displace and therefore the vibration levels will be smaller than for an aluminum pipe with the same energy inputs. In turn, the pressure required to produce the same level of vibrations on a steel pipe versus an aluminum pipe are much greater. The model confirms these expectations, as seen in Figure 3.2.

3.6.3 Contained fluid

Two fluids, water and oil, were chosen to compare the effect of fluid parameters on radial displacement and pressure. A denser fluid, such as water in comparison to oil, results in an increase in radial vibrations, due to a larger fluid-loading on the surface. The acoustical and longitudinal fluid-loading terms are proportional to the fluid density. The radial displacement from the $n = 0$ breathing mode is plotted for both fluids in Figure 3.3.

Table 3.4. Fluid properties

fluid	density ρ_f [kg/m^3]	sound speed c_f [m/s]	ring frequency ω_r [kHz]
water	998	1481	10.6
steel	950	1540	10.6

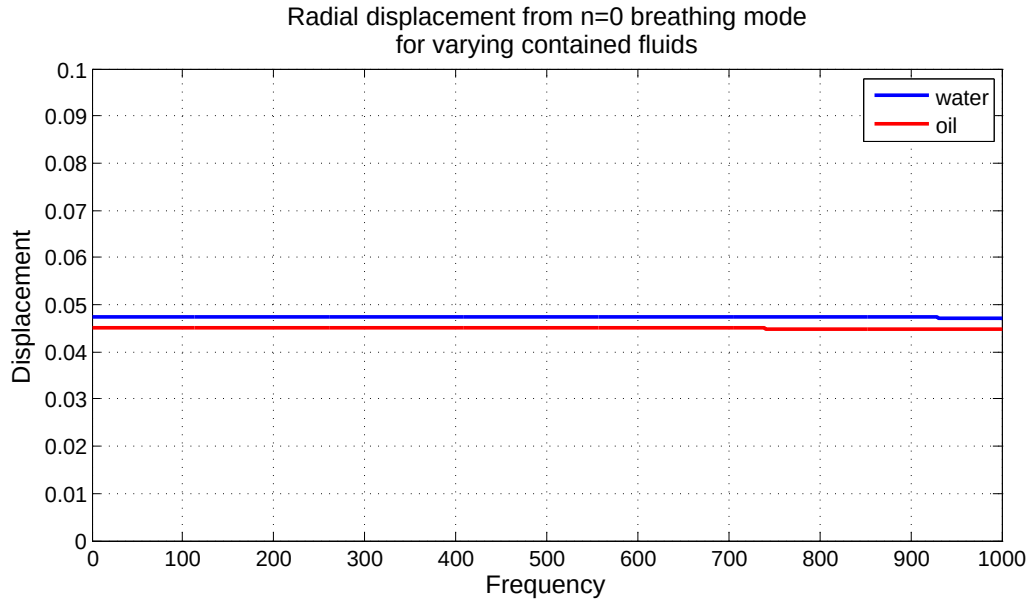

Figure 3.3. Response of pipe to varying fluid.

3.7 Energy flow

The analysis of the energy flow factors will focus on the ratio of the longitudinal and acoustical energy flow. If the measurement accelerometers are correctly placed and have no transverse sensitivity, the torsional and flexural energy flow factors have little to no effect on the accuracy of the pressure prediction. The torsional energy only contributes to the tangential motion, and therefore will have no effect on the measurement of the normal vibrations, unless some transverse sensitivity is attributed to the sensors. The flexural energy flow has a negligible effect on the accuracy, unless one or more of the accelerometers are incorrectly placed, preventing the correct calculation of the $n = 0$ breathing mode. Therefore, with the accelerometers correctly configured in an equally-spaced circumferential ring and with no transverse sensitivity, the longitudinal energy flow is the only factor that contributes to any inaccuracies.

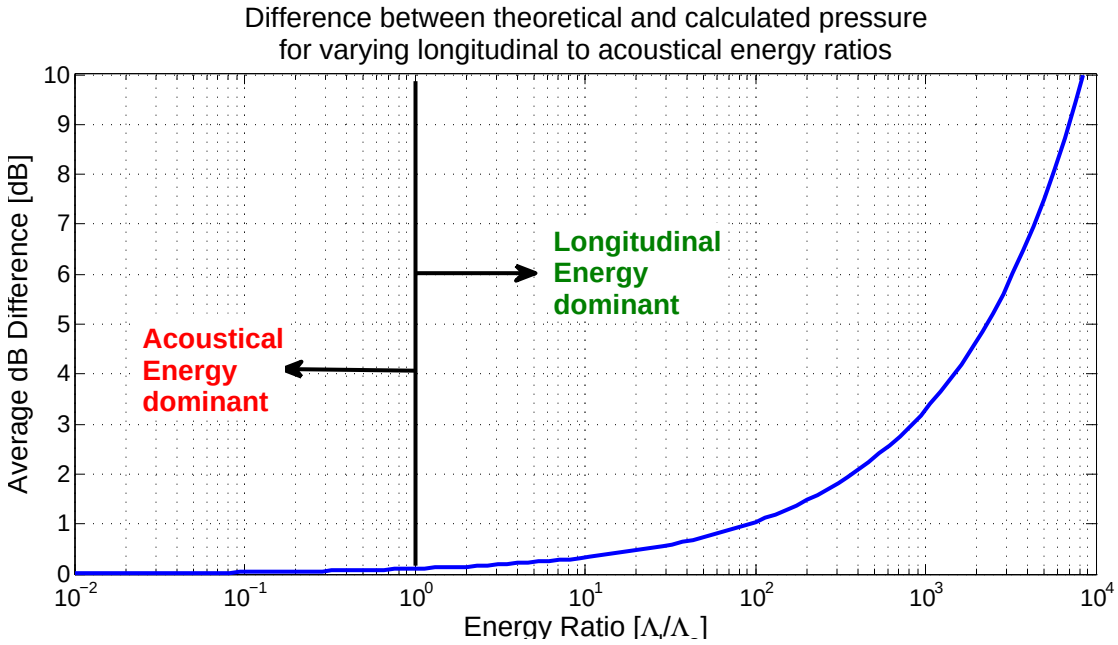

Figure 3.4. Sensitivity of error to variations in the longitudinal and acoustical energy.

The approximate expression for pressure (Equation (3.3.2)) assumes that w_0 is dominated by the acoustical energy. Therefore, it is of interest to examine the limits to this assumption. Figure 3.4 shows that there is very little difference between the exact and approximate pressure calculations when the acoustical energy is dominant over the longitudinal energy in the system. However, the deviation from the exact pressure appears when the longitudinal energy starts to dominate the system. This does not mean that the radial displacement is dominated by contributions from the longitudinal energy, but that the energy in the system is dominated by the longitudinal propagating wave energy and the longitudinal radial displacement is no longer negligible. Yet, the longitudinal energy can be 100 times that of the acoustical energy while maintaining an error less than 1 dB. It is not expected for the longitudinal energy flow to be 100 times greater than the acoustical energy flow, so it is safe to assume that the acoustical component of radial motion dominates the total motion and therefore, the approximate expression for pressure is valid if the longitudinal energy is less than 100 times the acoustical energy.

3.7.1 Physical implications of energy flow

The parameter of energy flow is rather intangible, so it is of interest to produce distributions of energy flow using case-specific excitations. These specific cases will clarify the physical implications of changing the parameters that control energy flow.

The model is altered in order to determine the energy flow factors based on an input excitation to the system such as a mechanical force or acoustic monopole source. The resulting total surface displacements in the three orthogonal directions are computed. Pavic [9] presents a method for measuring the energy flow using the surface displacements, strain and derivatives of strain. All of these are measurable quantities, so it is also possible to compute these quantities analytically.

The method Pavic [9] uses to compute the total energy flow requires four differences of squared amplitudes,

$$L = U_{l+}^2 - U_{l-}^2, \quad A = U_{a+}^2 - U_{a-}^2, \quad T = V_{t+}^2 - V_{t-}^2, \quad B = W_{b+}^2 - W_{b-}^2. \tag{3.7.1}$$

The real displacement amplitudes, U, V and W are not measurable directly, therefore we must use the total displacements $\mathbf{u}, \mathbf{v}$ and $\mathbf{w}$ to find the four quantities L, A, T and B. The torsional and bending quantities can be computed rather simply as,

$$T = 2a/\left[c_s \Omega \sin(2\zeta_t \Omega \delta/a)\right] \overline{\dot{v}^+(\delta,\alpha) v^+(-\delta,\alpha)} \tag{3.7.2}$$

$$B = 2a/\left[c_s \Omega \sin(2\zeta_b \sqrt{\Omega}\delta/a\right] \Big(\overline{\dot{w}^-(\delta,\alpha) w^-(-\delta,\alpha)} + \overline{\dot{w}^-(\delta,\alpha+\pi/2) w^-(-\delta,\alpha+\pi/2)} \Big), \tag{3.7.3}$$

where v^+ is the torsional component of the total tangential displacement from Equation (2.4.2b),

$$v^+ = V_{t+}\mu_{t+} + V_{t-}\mu_{t-}, \tag{3.7.4}$$

and w^- is the flexural components of the total radial displacement from Equation (2.4.2c)

$$w^- = W_{b+}\mu_{b+}\cos(\theta_+) + W_{b-}\mu_{b-}\cos(\theta_-). \tag{3.7.5}$$

Again, since the real displacement amplitudes are not available, v^+ is the $n = 0$ component of tangential displacement and w^- is the $n = 1$ component of radial displacement.

The squared differences L and A are slightly more complicated as they are both related to the $n = 0$ mode and are not easily separated as was the case for the quantities

T and B. In order to resolve this problem, Pavic [9] introduces four new variables,

$$\Phi_l = iU_{l+}\exp(i\phi_{l+}) + iU_{l-}\exp(i\phi_{l-}), \tag{3.7.6a}$$

$$\Xi_l = -(\kappa_l/a)\left[U_{l+}\exp(i\phi_{l+}) - U_{l-}\exp(i\phi_{l-})\right], \tag{3.7.6b}$$

$$\Phi_a = iU_{a+}\exp(i\phi_{a+}) + iU_{a-}\exp(i\phi_{a-}), \tag{3.7.6c}$$

$$\Xi_a = -(\kappa_a/a)\left[U_{a+}\exp(i\phi_{a+}) - U_{a-}\exp(i\phi_{a-})\right], \tag{3.7.6d}$$

where Φ_l and Φ_a are the longitudinal and acoustical components of $\mathbf{u}$ at $x = 0$, and Ξ_l and Ξ_a are the derivatives with respect to x of the longitudinal and acoustical components of $\mathbf{u}$ at $x = 0$. These variables are redefined as a function of the total axial displacement $\mathbf{u}$, axial strain $\epsilon = \partial u/\partial x$ and two strain derivatives,

$$\Phi_l = -(\kappa_a^2\mathbf{u} + a^2\partial\epsilon_x/\partial x)/(\kappa_l^2 - \kappa_a^2), \quad \Xi_l = (\kappa_a^2\epsilon_x + a^2\partial^2\epsilon_x/\partial x^2)/(\kappa_l^2 - \kappa_a^2), \tag{3.7.7a}$$

$$\Phi_a = -(\kappa_l^2\mathbf{u} + a^2\partial\epsilon_x/\partial x)/(\kappa_a^2 - \kappa_l^2), \quad \Xi_a = (\kappa_l^2\epsilon_x + a^2\partial^2\epsilon_x/\partial x^2)/(\kappa_a^2 - \kappa_l^2), \tag{3.7.7b}$$

which are related to the squared differences through the following expressions,

$$\overline{\Xi_l(t)\Phi_l(t)} = (1/2)\mathrm{Re}\{\Xi_l\Phi_l^*\} = \kappa_l[\omega/(2a)](U_{l+}^2 - U_{l-}^2) \tag{3.7.8}$$

$$\overline{\Xi_a(t)\Phi_a(t)} = (1/2)\mathrm{Re}\{\Xi_a\Phi_a^*\} = \kappa_a[\omega/(2a)](U_{a+}^2 - U_{a-}^2). \tag{3.7.9}$$

Solving for L and A results in,

$$L = \frac{a}{\omega\kappa_l}\mathrm{Re}\{\Xi_l\Phi_l^*\}$$

$$A = \frac{a}{\omega\kappa_a}\mathrm{Re}\{\Xi_a\Phi_a^*\}.$$

Therefore, the four squared differences L, A, T and B, required to calculate the distri-

bution of energy flow, are defined in terms of the three total displacements, axial strain and its derivatives. Therefore, a model is desired which can compute these six variables.

The model chosen to simulate the displacement and strain of the pipe uses the Donnell & Mushtari equations of cylindrical shell theory given by Leissa [14] and later described by Skelton and James [15]. The following formulations follow that of Skelton and James [15]. The pipe is assumed to be an infinite length isotropic shell, so that the only modes of vibration are in the circumferential plane and "rotatory inertia and transverse shear effects are omitted" [15]. The spectral equations of motion are,

$$\begin{pmatrix} S_{11} & S_{12} & S_{13} \\ S_{21} & S_{22} & S_{23} \\ S_{31} & S_{32} & S_{33}+Fl \end{pmatrix} \begin{pmatrix} \tau_u \\ \tau_v \\ \tau_w \end{pmatrix} = \begin{pmatrix} E_u \\ E_v \\ E_w \end{pmatrix} \tag{3.7.10}$$

where

$$S_{11}(n,k_x) = E_1\left(k_x^2 + n^2(1-\nu)/2a^2\right) - \omega^2\rho_s h, \tag{3.7.11a}$$

$$S_{12}(n,k_x) = E_1(1+\nu)nk_x/2a, \tag{3.7.11b}$$

$$S_{13}(n,k_x) = -E_1\nu i k_x/a, \tag{3.7.11c}$$

$$S_{21}(n,k_x) = S_{21}(n,k_x), \tag{3.7.11d}$$

$$S_{22}(n,k_x) = E_1\left((1-\nu)k_x^2/2 + n^2/a^2 + 2k_x^2\beta^2(1-\nu) + \beta^2 n^2/a^2\right) - \omega^2\rho_s h, \tag{3.7.11e}$$

$$S_{23}(n,k_x) = -E_1(in/a^2 + i\beta^2(2-\nu)k_x^2 n + i\beta^2 n^3/a^2), \tag{3.7.11f}$$

$$S_{31}(n,k_x) = -S_{13}(n,k_x), \tag{3.7.11g}$$

$$S_{32}(n,k_x) = -S_{23}(n,k_x), \tag{3.7.11h}$$

$$S_{33}(n,k_x) = E_1(1/a^2 + \beta^2 a^2 k_x^4 + \beta^2 n^4/a^2 + 2\beta^2 k_x^2 n^2) - \omega^2\rho_s h, \tag{3.7.11i}$$

and $E_1 = (1+i\eta)E$ is the complex Young's modulus to account for damping η; $\tau_u(n,k_x)$, $\tau_v(n,k_x)$ and $\tau_w(n,k_x)$ are the spectral displacements; $E_u(n,k_x)$, $E_v(n,k_x)$ and $E_w(n,k_x)$ are the spectral excitations; and Fl is the fluid-loading term defined as,

$$Fl = \rho_{ext}\omega^2 \frac{H_{|n|}(k_{r_{ext}}a)}{k_{r_{ext}}H'_{|n|}(k_{r_{ext}}a)} - \rho_{int}\omega^2 \frac{J_{|n|}(k_{r_{int}}a)}{k_{r_{int}}J'_{|n|}(k_{r_{int}}a)}, \tag{3.7.12}$$

where $H_{|n|}$ and $J_{|n|}$ are the nth order Hankel and Bessel functions respectively.

The excitations will vary based on the specific case and its prescribed input force. Solving for the spectral displacements is a result of simple matrix algebra,

$$\{\tau(n,k_x)\} = [S(n,k_x)]^{-1}\{E(n,k_x)\}. \tag{3.7.13}$$

To return to quantities in real space, the following transform can be computed as,

$$\tau(r,\theta,x) = \frac{1}{2\pi}\sum_{n=-\infty}^{\infty}\exp(in\theta)\int_{-\infty}^{\infty}\tau(r,n,k_x)\exp(ik_x x)dk_x, \tag{3.7.14}$$

and discretely as,

$$\tau(r,\theta,x) = \frac{1}{2\pi}\sum_{k_x,n}^{\infty}\tau(r,n,k_x)\exp(ik_x x)\exp(in\theta). \tag{3.7.15}$$

The transform into real space produces the total displacements in each of the three directions. However, to compute the energy flow, the $n = 0$ component of tangential displacement and the $n = 1$ component of radial displacement are desired. These are easily calculated as,

$$v^+(r,\theta,x) = \frac{1}{2\pi}\sum_{k_x}^{\infty}\tau_v(r,0,k_x)\exp(ik_x x) \tag{3.7.16}$$

$$w^{-}(r,\theta,x) = \frac{1}{2\pi}\sum_{k_x,n}^{\infty}\tau_w(r,1,k_x)\exp(ik_x x)\exp(i\theta). \tag{3.7.17}$$

The axial strain can also be computed from this model as it is the derivative of axial displacement. The strain and its derivatives are,

$$\epsilon_x = \frac{1}{2\pi}\sum_{k_x,n}^{\infty}(ik_x)\tau_u(r,n,k_x)\exp(ik_x x)\exp(in\theta) \tag{3.7.18}$$

$$\frac{\partial\epsilon_x}{\partial x} = \frac{1}{2\pi}\sum_{k_x,n}^{\infty}(-k_x^2)\tau_u(r,n,k_x)\exp(ik_x x)\exp(in\theta) \tag{3.7.19}$$

$$\frac{\partial^2\epsilon_x}{\partial x^2} = \frac{1}{2\pi}\sum_{k_x,n}^{\infty}(-ik_x^3)\tau_u(r,n,k_x)\exp(ik_x x)\exp(in\theta) \tag{3.7.20}$$

Therefore, along with the properties of the fluid and structure, an excitation is provided as an input in order to calculate the spectral displacements, which are transformed into displacements in real space. The strain and derivatives of strain are computed from the displacement, and these values help to compute the four squared differences from Equation (3.7.1) and in turn the energy flows in each wave-type.

3.7.2 Excitation vectors of varying force inputs

In order to solve Equation (3.7.10) and determine the energy flows, an excitation vector must be defined. Skelton and James [15] define the spectral excitation vector for a number of different force inputs. Here, two excitations are presented corresponding to a mechanical and acoustical source in order to study their corresponding distribution of energy flow.

3.7.2.1 Mechanical excitation

The mechanical excitation vector for a point force applied at (θ_0, x_0) on the cylinder is defined as,

$$\begin{pmatrix} E_u(n,k_x) \\ E_v(n,k_x) \\ E_w(n,k_x) \end{pmatrix} = \begin{pmatrix} F_u \exp(-in\theta_0 - ik_x x_0)/2\pi a \\ F_v \exp(-in\theta_0 - ik_x x_0)/2\pi a \\ F_w \exp(-in\theta_0 - ik_x x_0)/2\pi a \end{pmatrix} \tag{3.7.21}$$

where F_u,F_v and F_w are the point forces in the axial, tangential and radial directions respectively. This excitation vector can be altered to represent a distributed force which excites all modes by disregarding the exponential terms,

$$\begin{pmatrix} E_u(n,k_x) \\ E_v(n,k_x) \\ E_w(n,k_x) \end{pmatrix} = \begin{pmatrix} F_u/2\pi a \\ F_v/2\pi a \\ F_w/2\pi a \end{pmatrix}. \tag{3.7.22}$$

As seen in Figure 3.5(a), the energy from the bending, longitudinal, and torsional propagating waves is larger than the acoustical energy. Yet, even when the flexural and torsional energy is almost one million times the acoustical energy and the longitudinal energy is about twenty times the acoustical energy in the system, Figure 3.5(b) shows that the average error is less than 1 dB over the frequency range of interest. However, the results of these figures are obtained under the assumption that the sensors are perfectly placed with zero transverse sensitivity. With such a large amount of flexural energy flow in the system, a small misplacement may introduce a large amount of error. The sensor configuration and transverse sensitivity in response to varying energy ratios is further discussed in Section 3.8.

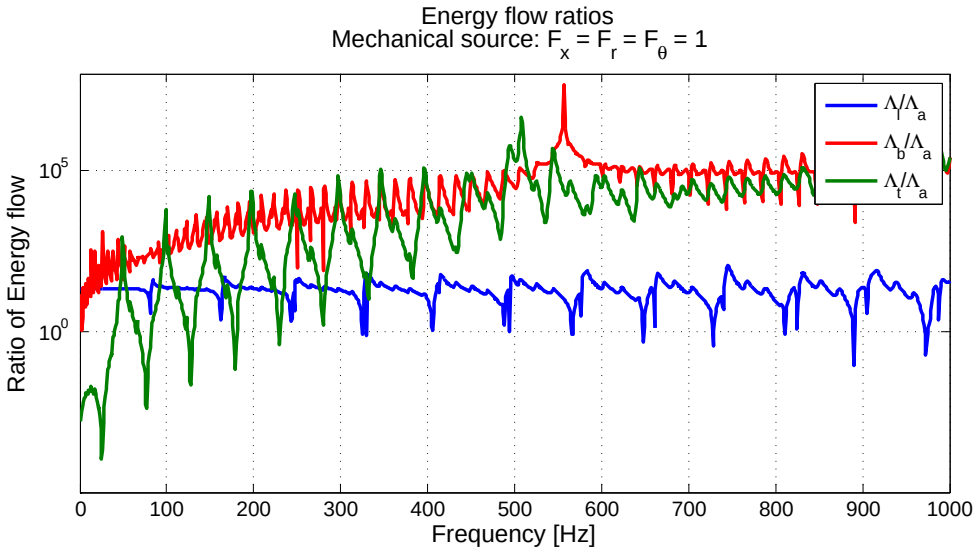

(a) Energy flow ratios for a mechanical source excitation

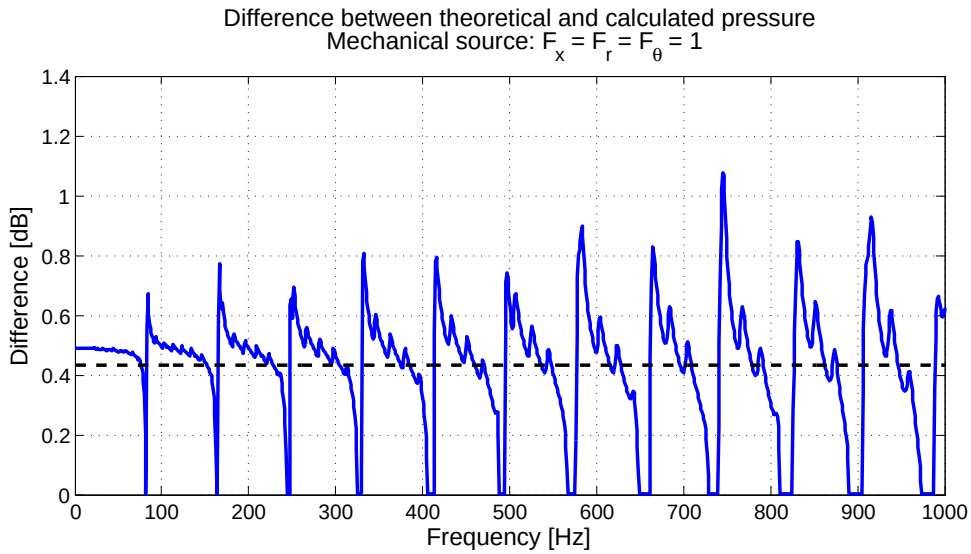

(b) Difference in pressure calculations due to prescribed distribution of energy flow resulting from a mechanical source excitation

Figure 3.5. Mechanical excitation

3.7.2.2 Monopole excitation

The excitation vector for a monopole located at (r_0, θ_0, x_0) within the interior of the cylinder, is defined as,

$$\begin{pmatrix} E_u(n,k_x) \\ E_v(n,k_x) \\ E_w(n,k_x) \end{pmatrix} = \begin{pmatrix} 0 \\ 0 \\ 2A\exp(-in\theta_0 - ik_x x_0)\frac{J_{|n|}(k_r r_0)}{k_r a J'_{|n|}(k_r a)} \end{pmatrix} \tag{3.7.23}$$

where A is the pressure per unit wavenumber.

When the system is excited by an acoustic monopole source, the energy of the torsional propagating wave is zero since it does not couple with the fluid. The energy of the longitudinal and flexural wavetypes, in comparison to the acoustical wavetype, are larger for a monopole source with an amplitude $A = 1$. Yet, the average error is still less than 1 dB, although the error reaches almost 7 dB at some frequencies. Again, this result assumes that the sensors are perfectly placed.

For both mechanical and acoustical excitations, the proposed method utilizing a ring of accelerometers to measure internal pressure should give accurate predictions within 1 dB of the actual pressure. That is if there are no errors introduced due to the accelerometers, such as misplacement and transverse sensitivity. These errors will likely be introduced when taking experimental measurements, and therefore a greater level of error should be expected. The following section will assess the sensitivity of accurate measurements to the sensor inaccuracies.

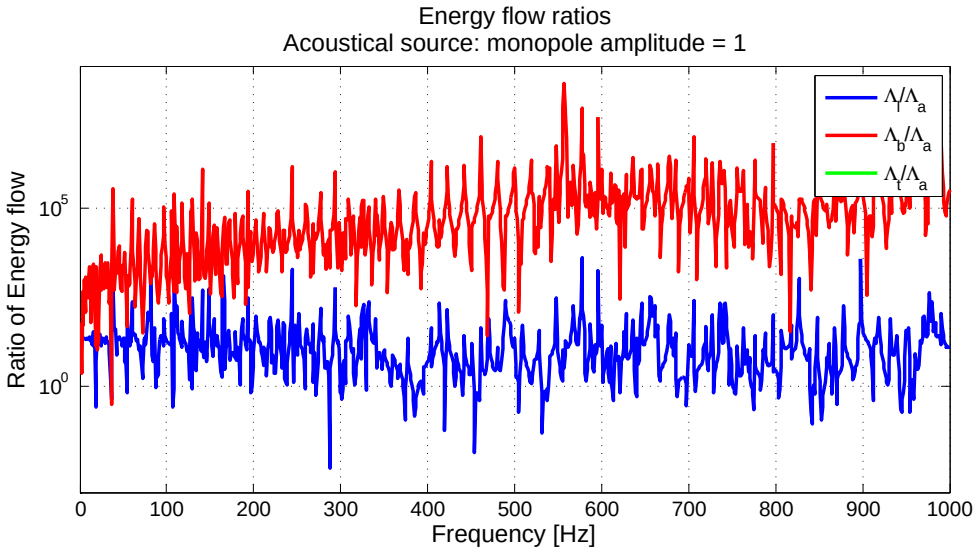

(a) Energy flow ratios for a monopole source excitation

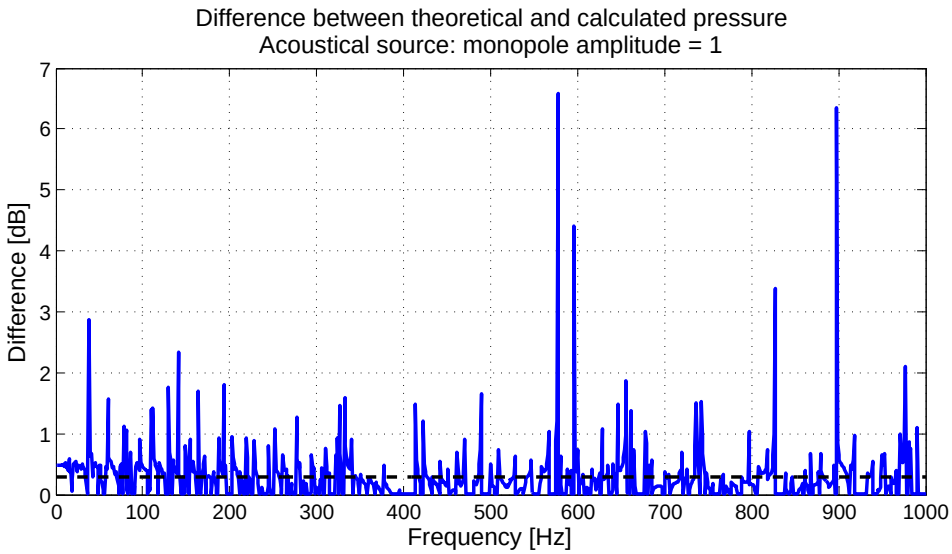

(b) Difference in pressure calculations due to prescribed distribution of energy flow resulting from a monopole source excitation

Figure 3.6. Monopole excitation

3.8 Sensor selection and configuration

It is important to select a measurement accelerometer for qualities that improve its performance in accurately measuring the breathing mode. As discussed in Section 3.6, piping systems with a small diameter-to-thickness ratio require an accelerometer with a high sensitivity and low noise floor in order to measure the low level vibrations. The transverse sensitivity will also affect the accuracy of the calculation of internal pressure. The model developed in Section 3.2.1 will be helpful in determining the importance of choosing an accelerometer for its low transverse sensitivity. Once the accelerometers are selected, their correct or incorrect configuration will affect the accuracy of the $n = 0$ breathing mode measurements perceived by the ring of accelerometers. This model will assess how sensitive the error is to the configuration and transverse sensitivity of the accelerometers.

3.8.1 Transverse sensitivity

Accelerometers are susceptible to transverse sensitivity, which allows a percentage of the axial and circumferential motion to contaminate the desired radial motion measurement. When using an accelerometer to measure the vibration, it is assumed that the additional unwanted vibrations are negligible. This model evaluates the error introduced by various percentages of transverse sensitivity. If the model shows that the transverse sensitivity has a large effect on the measurements, then it would be suggested to specifically choose accelerometers with low transverse sensitivity.

The angle q between the pipe axis and direction of maximum transverse sensitivity is consistently applied to all sensor positions in the model although each accelerometer would have a slightly different angle of maximum transverse sensitivity. Three cases are presented here: $q = 0^\circ$ where the transverse sensitivity is only applied to the ax-

ial motion (Figure 3.7), $q = 90°$ where the transverse sensitivity is only applied to the tangential motion (Figure 3.8), and $q = 45°$ where the transverse sensitivity is equally applied to the axial and tangential motion (Figure 3.9). As expected, the error decreases with decreasing transverse sensitivity. Yet, it is sensitive to the axis of maximum transverse sensitivity as seen in Figures 3.7, 3.8, and 3.9. If an acceptable error is less than 1dB, a transverse sensitivity $\leq 5\%$ should be acceptable for frequencies above 200 Hz. Though the frequency range below 200 Hz produces errors greater than 1dB, a lower transverse sensitivity allows less than 1dB error at lower frequencies than 200 Hz. The lowest possible transverse sensitivity is best if the frequency range of interest includes frequencies less than 200 Hz.

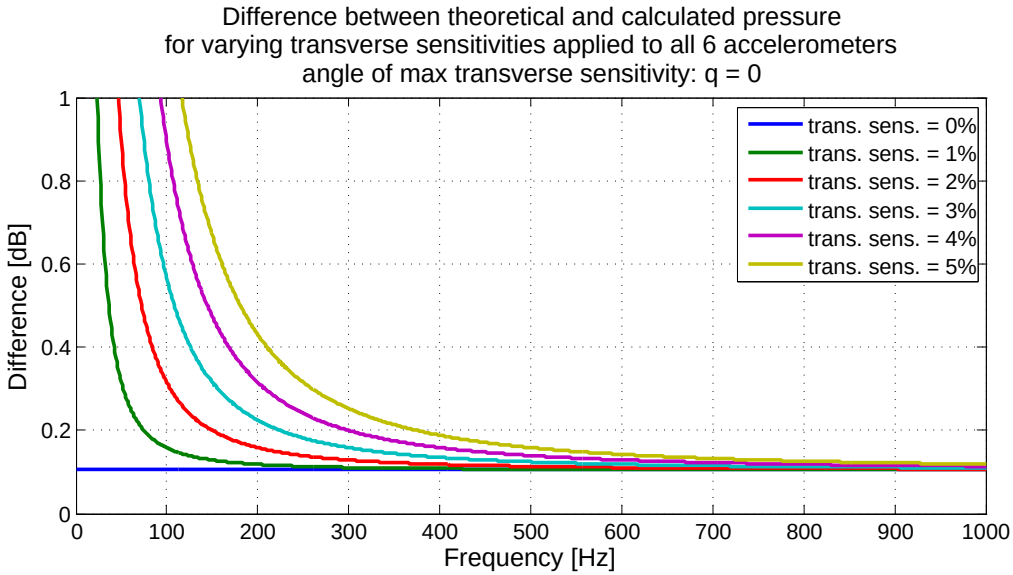

Figure 3.7. Error due to varying transverse sensitivities with angle $q = 0$

The previous three cases assume the energy is equally distributed among the four propagating wave types. However, the percentage of transverse motion may produce unacceptable error if this motion is greater than the radial displacement. Figures 3.10 and 3.11 show the effect of non-equal distributions of energy that may produce greater axial and tangential motion.

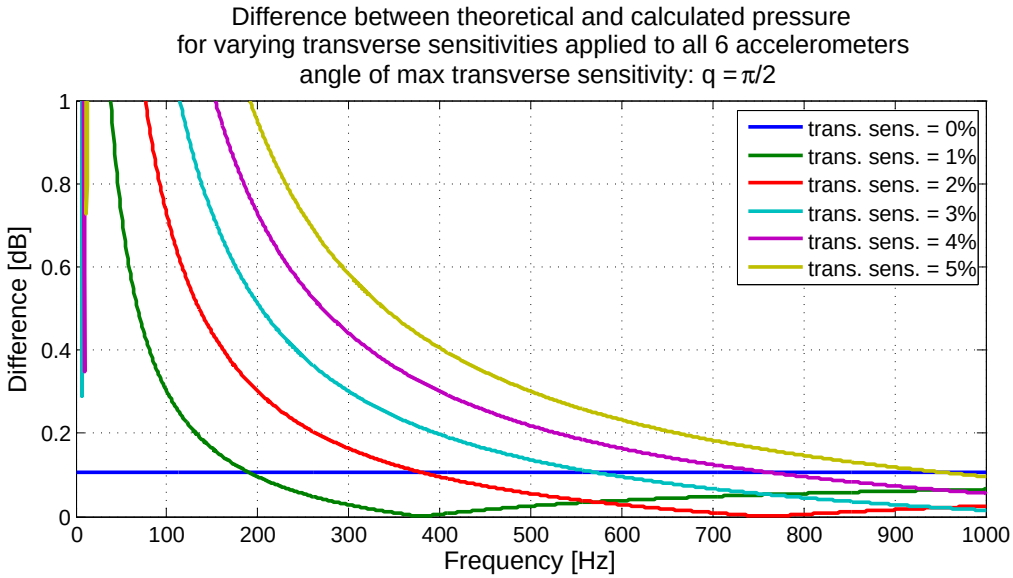

Figure 3.8. Error due to varying transverse sensitivities with angle $q = \pi/2$

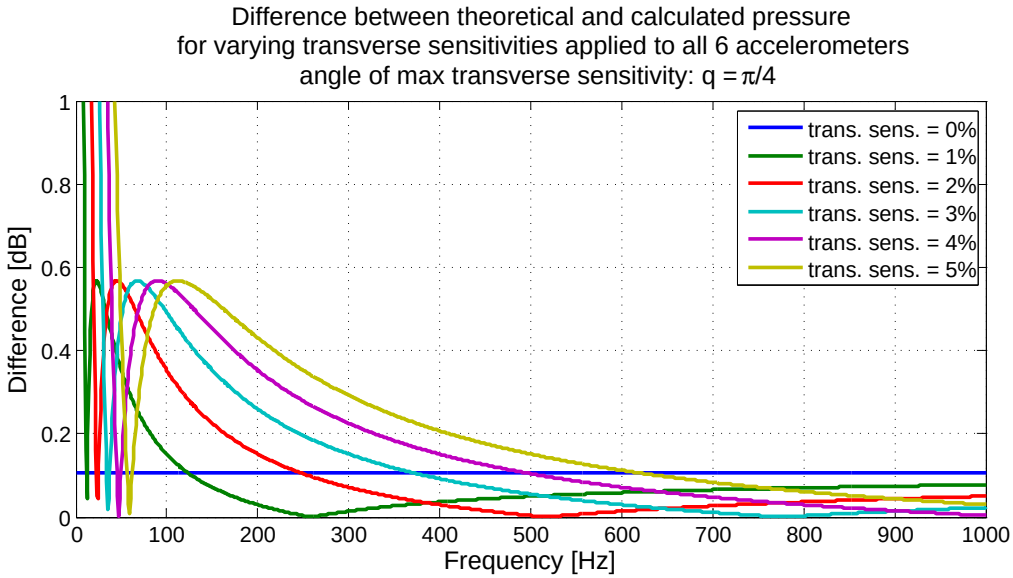

Figure 3.9. Error due to varying transverse sensitivities with angle $q = \pi/4$

If the acceptable average error in this model is less than 1 dB, then some distributions of energy flow will not be conducive to accurate measurements using accelerometers with 1% transverse sensitivity. When the angle of maximum transverse sensitivity is $q = 0$, the accelerometer is only sensitive to transverse motion in the axial direction. The axial motion is dominated by the longitudinal energy, so a greater amount of longitudinal

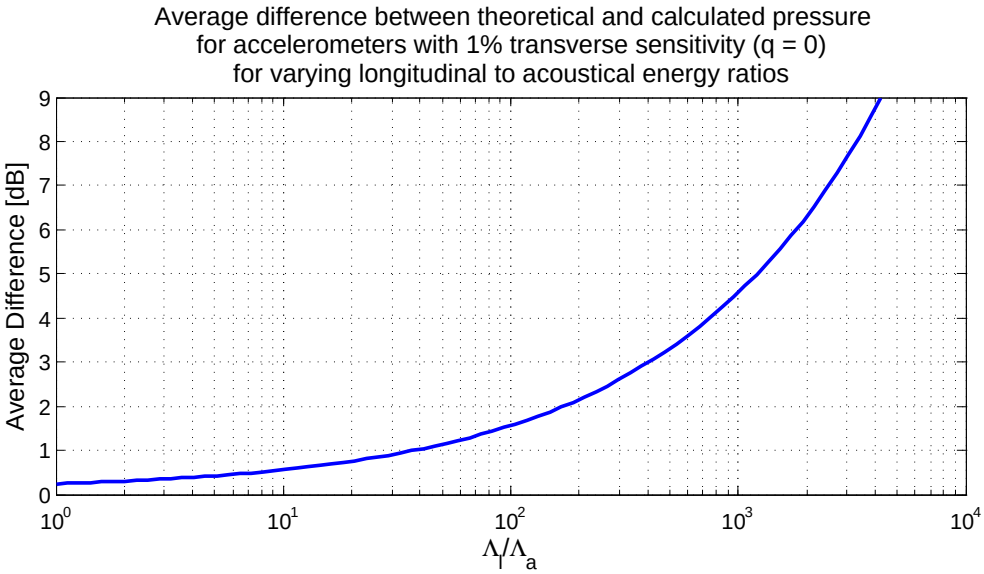

Figure 3.10. Error due to varying longitudinal to acoustical energy ratios for accelerometers with 1% transverse sensitivity and with angle $q = 0$

energy in comparison to acoustical energy will produce greater errors. This is shown in Figure 3.10, where the 1dB of acceptable error is surpassed when the longitudinal energy is about 40 times greater than the acoustical energy. This ratio $\Lambda_l/\Lambda_a = 40$ is the average ratio of energy encountered in response to an acoustic monopole source. For accelerometers with 1% transverse sensitivity, this ratio would still be acceptable. Yet, a greater percentage of transverse sensitivity would be expected to produce a greater amount of error and in turn lower the limiting ratio of Λ_l/Λ_a.

When the angle of maximum transverse sensitivity is $q = \pi/2$, the accelerometer is only sensitive to transverse motion in the tangential direction. The tangential motion is dominated by the torsional energy. Higher energy distributed to the torsional wavetype in comparison to the acoustical wavetype produces significant error. Figure 3.11 shows that the torsional energy must be less than 20 times the acoustical energy if the error is to be less than 1 dB. This result is somewhat concerning, as a mechanical source as described in Section 3.7.2.1 can produce a distribution of energy where the torsional

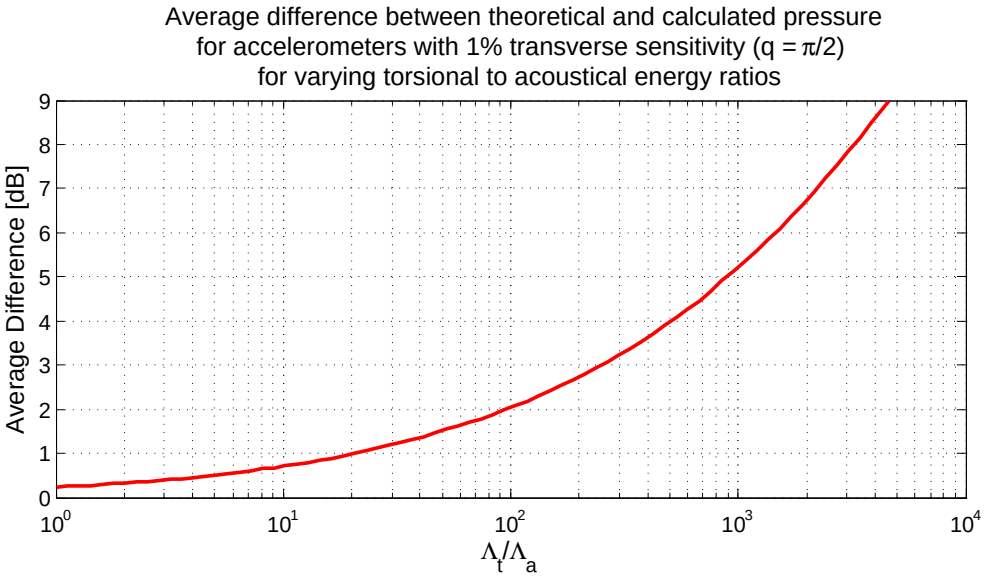

Figure 3.11. Error due to varying torsional to acoustical energy ratios for accelerometers with 1% transverse sensitivity and with angle $q = \pi/2$

energy is more than ten thousand times the acoustical energy. With that energy distribution, accelerometers with 1% transverse sensitivity or greater will most likely result in unacceptable levels of error.

Although, it is unlikely for the angle of maximum transverse sensitivity to be aligned with the axial or tangential motion alone, but rather a combination of the two, the results of this model show the importance of selecting accelerometers with the lowest possible transverse sensitivity.

3.8.2 Sensor configuration

There are unlimited combinations in which the accelerometer's positions can be offset, but one specific combination is chosen which gives among the highest error. An offset could be randomly assigned to each accelerometer, though this leads to an inconsistency in the model. Therefore, this specific combination is chosen and is based on the polarization angle of the bending wave. If the polarization angle is set at zero degrees, this

corresponds to the position of the first accelerometer. The two accelerometers closest to this position are the most sensitive to an incorrect placement. Therefore, the placement of the first and second accelerometers are chosen to be varied to analyze the effect of misplacement. Figure 3.12 shows the effect of offsetting these two accelerometers by varying degrees. At frequencies greater than 500 Hz, the model is rather insensitive to a small offset. Though, at low frequencies, especially below 200 Hz, the model is extremely sensitive to any misplacement. To limit the error at low frequencies, detailed attention must be paid to accelerometer placement.

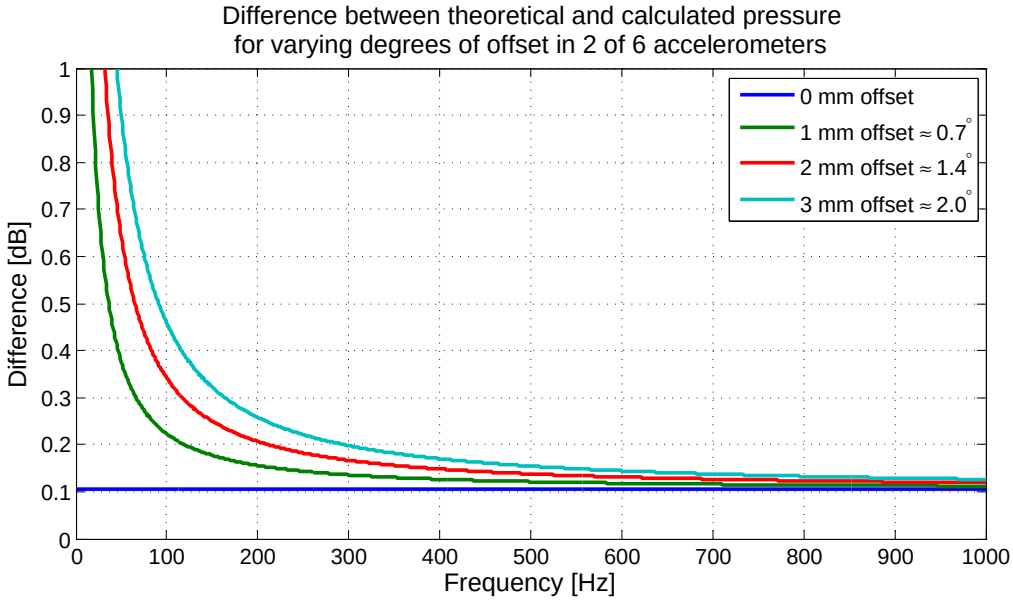

Figure 3.12. Error due to varying degrees of accelerometer offset

The error introduced from the incorrect placement of accelerometers is due to the incorrect circumferential decomposition calculation of the $n = 0$ breathing mode, which is essentially the mean of accelerometer measurements at each frequency. If the accelerometers are perfectly placed, the mean will cancel out a majority of the longitudinal and flexural components of radial motion. However, if one or more accelerometers are offset, the longitudinal and flexural contributions to radial motion may be more present in the $n = 0$ breathing mode calculation, making the predicted amplitude more susceptible to

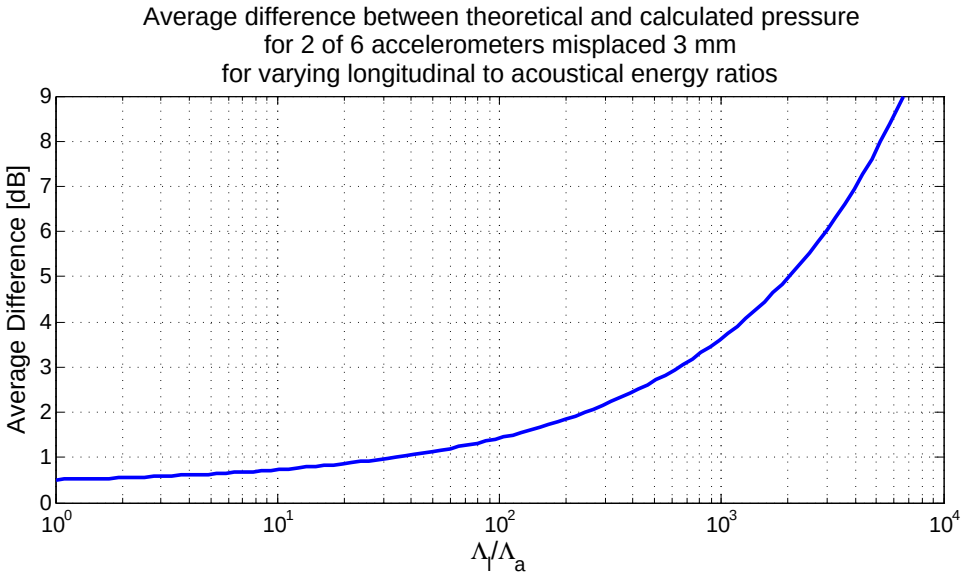

Figure 3.13. Error due to varying longitudinal to acoustical energy ratios when two accelerometers are offset by 3mm

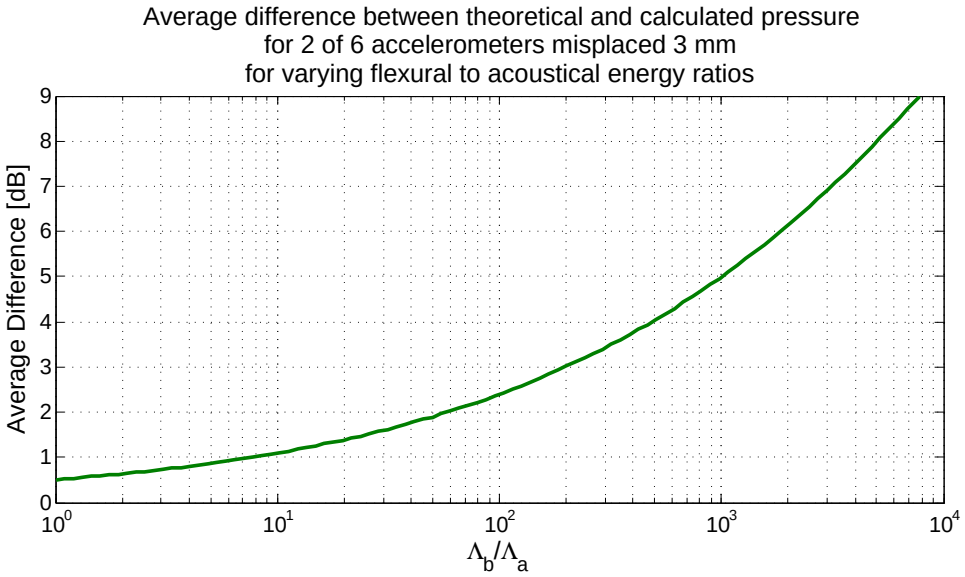

Figure 3.14. Error due to varying flexural to acoustical energy ratios when two accelerometers are offset by 3mm

errors. An increase in the energy of the longitudinal or flexural wavetypes in comparison to the acoustical wavetype may increase the error introduced by the misplacement of accelerometers. Figure 3.13 shows the effect of an increase in longitudinal energy as a result of two accelerometers offset by 3 mm. The acceptable 1 dB error is surpassed as

a ratio of $\Lambda_l/\Lambda_a \approx 40$ is approached. The ratio for flexural energy is shown in Figure 3.14, where the flexural energy must be less than seven times that of the acoustical energy in order for the error to be less than 1 dB as a result of a 3 mm offset in the two accelerometers.

The results presented here show that the model is extremely sensitive to incorrect placement of the accelerometers, especially when the dominant energy is from the longitudinal or flexural propagating waves.

3.8.3 Low frequency amplitude

The model is much more sensitive to the transverse sensitivity or misplacement of sensors at low frequencies. For frequency-independent energy sources, the mean radial displacement is almost constant. This is a result of the sum of positive and negative components of radial motion from the opposite sensor pairs, that leaves only the motion due to the $n = 0$ breathing motion. However, if a sensor is misplaced, the pairs will not be completely opposite and the $n = 1$ bending motion will not completely cancel out. Figure 3.15 plots the radial displacement at each position when they are perfectly placed and Figure 3.16 plots the radial displacement when the first and second position is misplaced by 3 mm. The small difference in placement produces respective mean differences with larger deviations at low frequencies.

The transverse sensitivity allows the pure $n = 0$ radial displacement to contain some contributions from the axial and tangential motion. Figures 3.17 and 3.18 show that the mean axial and tangential displacements are not constant. So if the displacement used to calculate the internal pressure contains some contributions from the axial or tangential motion, there will be a similar low frequency dependence.

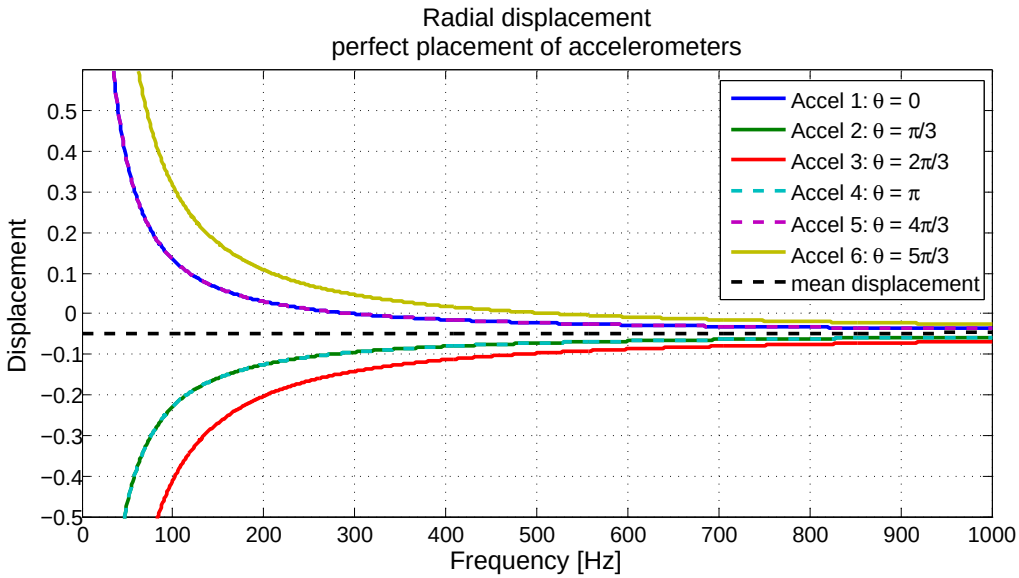

Figure 3.15. Radial displacement at the locations of the six equally-spaced sensors.

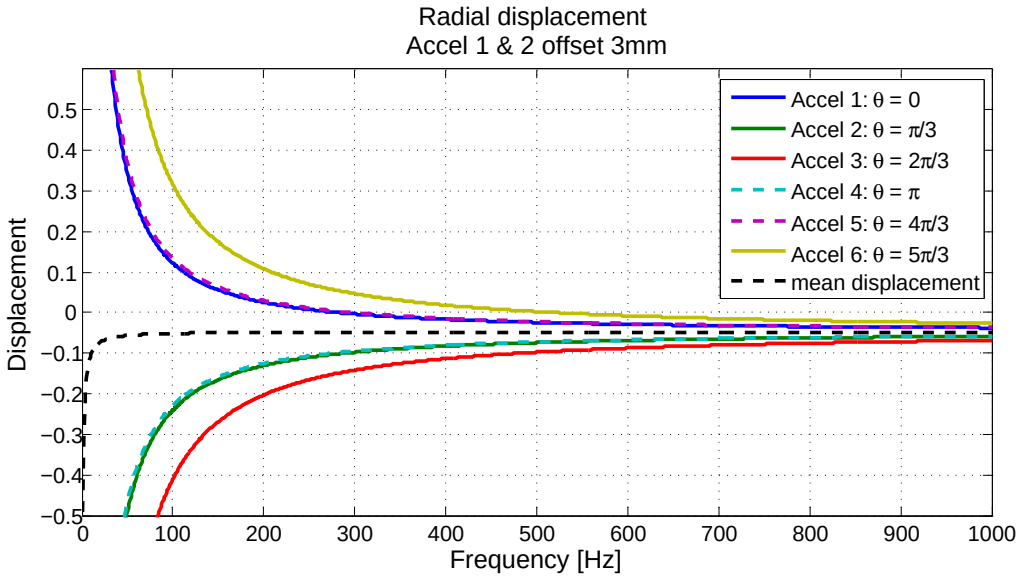

Figure 3.16. Radial displacement at the locations of the non-equally-spaced sensors.

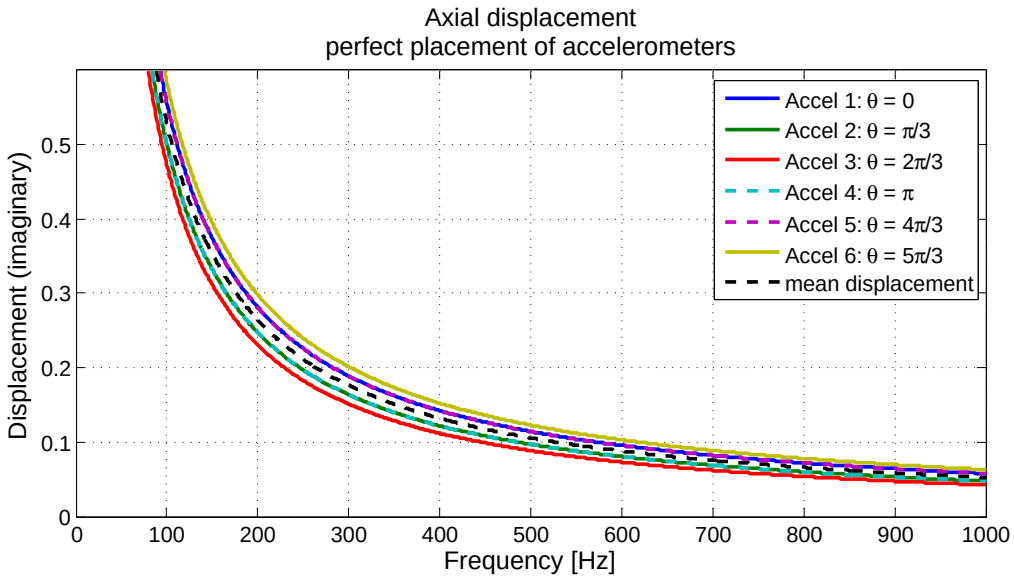

Figure 3.17. Axial displacement at the location of the six equally-spaced sensors.

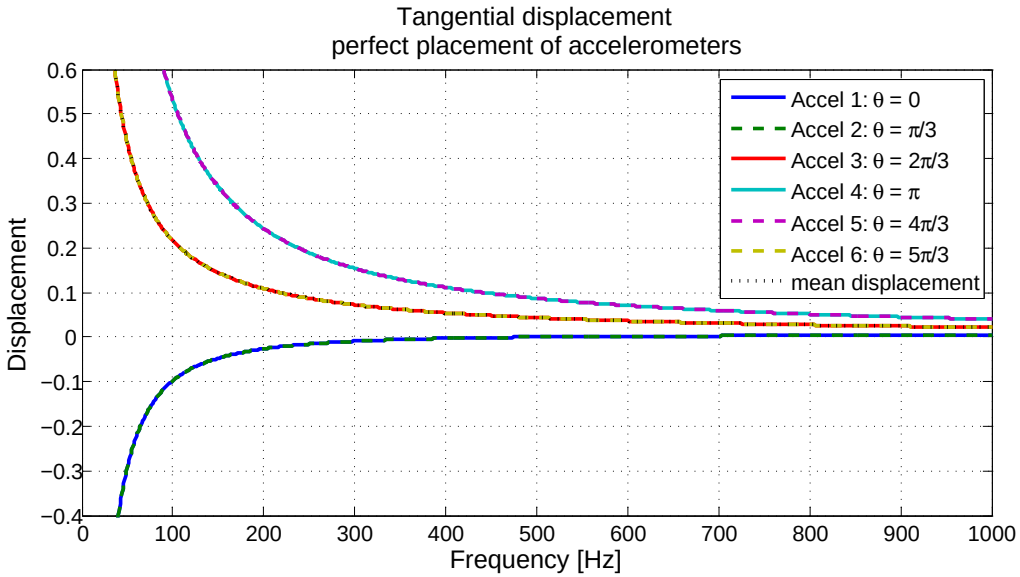

Figure 3.18. Tangential displacement at the location of the six equally-spaced sensors.

3.9 Summary

The model presented in this chapter confirms many expectations and determines the sensitivity of the approximate expression for pressure to certain parameters. The model results demonstrate the importance of selecting an accelerometer with a low noise floor and low transverse sensitivity. The correct placement of accelerometers in an equally-spaced ring is also important to making accurate measurements. The following chapter will provide experimental measurements to further analyze the feasibility of detecting internal acoustic pressure using a ring of accelerometers.

CHAPTER 4

EXPERIMENTAL METHODS & RESULTS

4.1 Experimental set-up

Experiments were conducted at the Garfield Thomas Water Tunnel facility of the Applied Research Laboratory located on the Penn State University Park campus. Water from the 48 inch diameter water tunnel was used to completely fill the piping system spanning about 17 m in total. A schematic of the set-up is shown in Figure 4.1. Not shown is the straight 150 mm diameter piping that extends about 4.7 m from the left end of the test section and about 9 m from the right end of the Tee-section (partly shown in Figure 4.2). Attached to the 4.7 m of piping to the left of the test section is a rubber pipe which bends upward in order for the excess water to be emptied into a holding tank (which is used only when filling the pipe with water). A butterfly valve was used to control the flow of water at this end. The valve was closed during measurements to ensure that

there was no flow through the pipe. At the opposite end, another valve was used to open access to the water tunnel reserve and fill the pipe with water. Once the pipe was completely filled, the two valves were shut so that the contained water was motionless.

The water-filled pipe was driven with an acoustical or mechanical source, both of which were located on/in the 305 mm diameter Sch 40 (7.1 mm) PVC Tee-section. The Tee pipe fitting was specifically chosen to provide easy access to insert and remove the USRD J9 projector acting as the acoustical source. The Tee-section can be seen in the schematic of Figure 4.1 and is pictured in Figure 4.2.

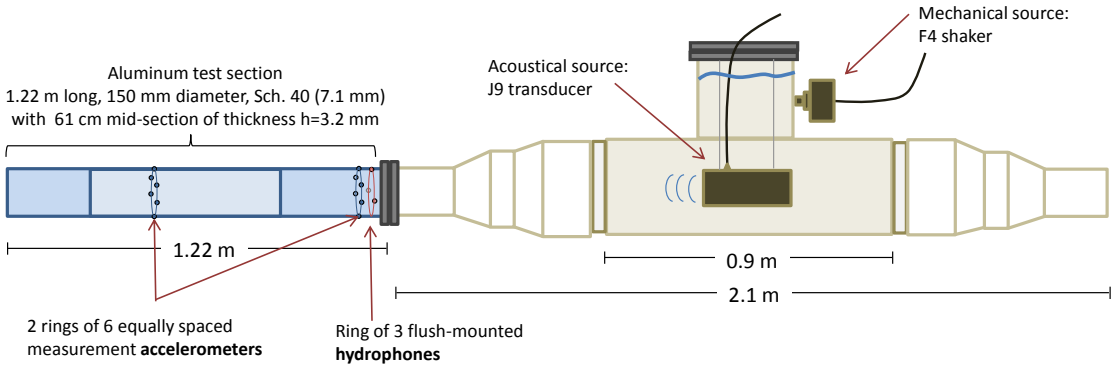

Figure 4.1. Schematic of source location and test section in the experimental set-up.

The J9 projector was attached to the lid of the Tee-section with four strings. The strings were carefully measured so that the J9 projector axis was aligned with the axis of the test section and oriented so that the driving piston was facing towards the test section. A Wilcoxon F4 electromagnetic shaker acted as the mechanical source. The shaker was attached about 130 mm up the neck of the Tee-section (pictured in Figure 4.3). It was glued to the PVC and oriented parallel to the axis of the test section. To sustain the weight and prevent the shaker from becoming detached, several wood blocks were placed beneath it. Special attention to the water level was given so that its highest point was above both excitation sources.

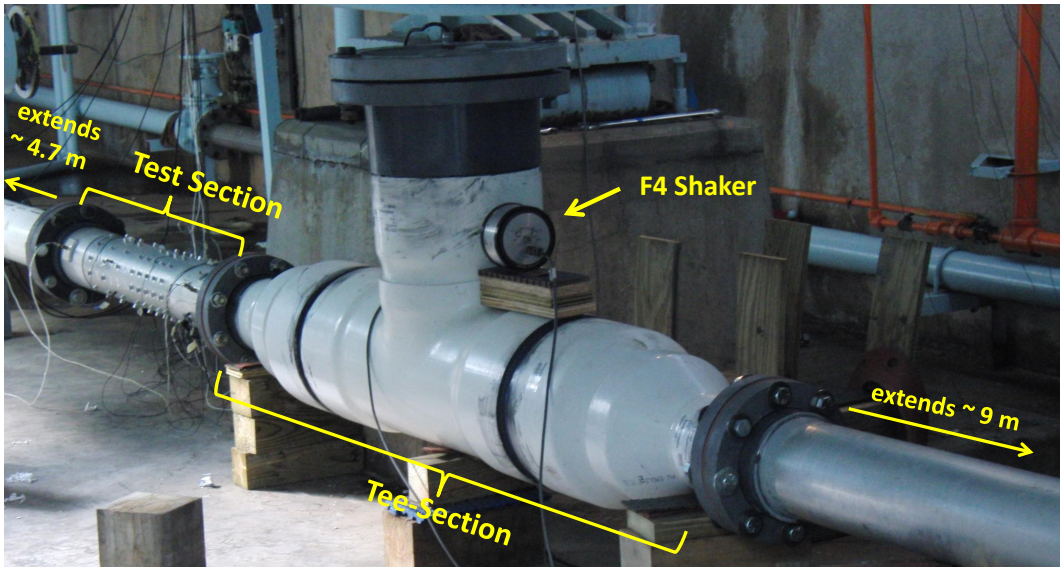

Figure 4.2. Photograph of experimental set-up.

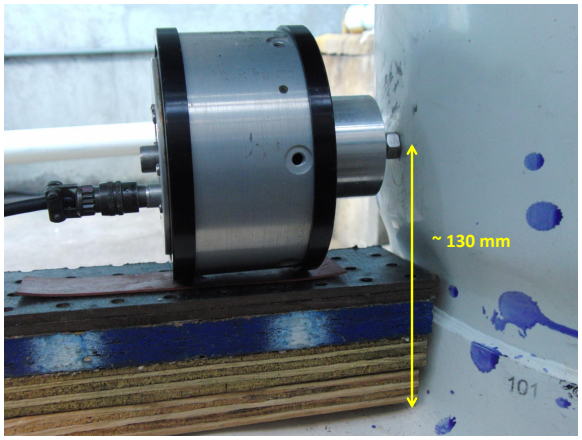

Figure 4.3. Photograph of the supported F4 Shaker attached to the neck of the Tee-section.

Transitional PVC pipe-fitting couplings were used to connect the 305 mm diameter Tee-section to the 150 mm diameter aluminum test-section on which all measurements were taken. The aluminum test section was originally a 1.22 m long 150 mm diameter Sch. 40 (7.1 mm thick) pipe. A photograph of the test section is shown in Figure 4.4. A 61 cm center portion of the pipe's outside surface was machined to a thickness of 3.2 mm and an inside diameter of 156 mm. A comparison of important frequency

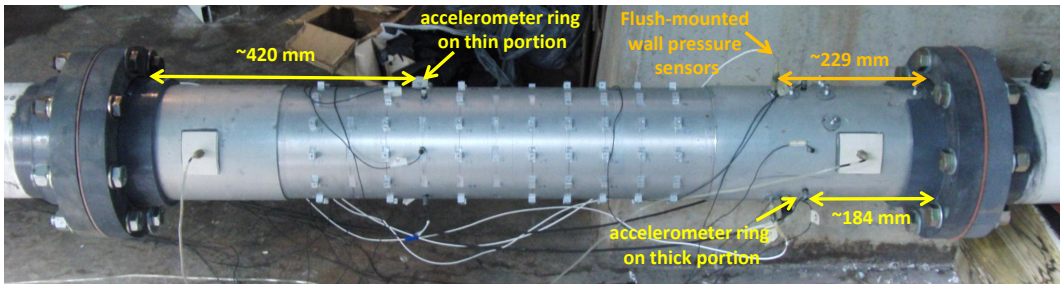

Figure 4.4. Photograph of 1.22 m long aluminum test.

Table 4.1. Important piping system parameters for pipe used in experiments.

	$h = 7.1$ mm, $d = 150$ mm	$h = 3.2$ mm, $d = 156$ mm
d/h	≈ 20	≈ 100
ring frequency (ω_r)	≈ 11.4 kHz	≈ 10.9 kHz
$n = 2$ cut on frequency	≈ 400 Hz	≈ 200 Hz
$n = 3$ cut on frequency	≈ 1400 Hz	≈ 700 Hz
$n = 4$ cut on frequency		≈ 1400 Hz
$p = 1$ cut on frequency	≈ 5 kHz	≈ 3 kHz

(a) Thick portion on right end of test section.

(b) Thin portion of test section.

Figure 4.5. A closer look at the accelerometer rings and pressure sensor ring on the thin and thick portions of the test section.

parameters for both cases of thickness are presented in Table 4.1, along with their value of diameter-to-thickness ratio.

The vibration response to the excitation sources was measured at two locations on the aluminum test-section to capture the effect of pipe wall thickness on the prediction

of pressure. Measurements were taken with 2 rings of six equally-spaced accelerometers (PCB W352, sensitivity 100 mV/g). One accelerometer ring was placed on the thin section (Figure 4.5(b)) about 420 mm from the left end of the test section, and the second accelerometer ring was placed on the thick section (Figure 4.5(a)) about 184 mm from the right end of the test section. The accelerometers were carefully glued to the aluminum pipe using mounting adhesive (LOCTITE 444). It is assumed that the accelerometers were carefully placed so that they were equally-spaced, however small misplacements are expected due to human error. A ring of 3 flush-mounted wall pressure sensors (PCB - 105M147, sensitivity 50 mV/psi) were located on the thick portion of the aluminum pipe about 229 mm from the left end of the test section.

4.2 Collecting and Processing experimental data

Data was collected from a total of 12 accelerometers and 3 flush-mounted wall pressure sensors simultaneously using a National Instruments PXI-1033 and the LabVIEW Time Data Acquisition (TDA) program. Recorded segments were at least 30 seconds long, with a sample frequency of 10,000 samples per second. All data was collected and recorded in the time domain and further processing of the data was performed using MATLAB. Sensitvities as specified on the sensor's data sheet were applied in MATLAB, and factory calibrated sensitivities were used when available.

A function generator included in the NI system was used to drive the excitation sources. The excitation input was Gaussian noise, filtered from 20 Hz to 1000 Hz. The range was limited to one kHz, as the J9 projector does not perform as well above that frequency. However, this is not of concern as the frequency range of interest is focused on low relative frequencies. The J9 projector was powered by a CROWN XTi2000 power amplifier and monitored by a FLUKE 45 Dual Display multimeter. The F4 shaker

was powered by a WILCOXON Research power amplifier (Model PA7C) and monitored by a FLUKE 87 V true RMS multimeter. The output RMS voltage and current were monitored for both excitation sources. To increase the acoustic pressure in the pipe, the voltage/current was increased. Vibration and pressure responses were collected at various voltage outputs of the J9 projector to determine the capability of the accelerometers to track pressure changes accurately.

4.2.1 Processing accelerometer data

After applying the appropriate sensitivities to each accelerometer, the $n = 0$ mode is calculated by two methods, one in the time domain and one in the frequency domain. Since the breathing mode is described as only the in-phase motion, higher order modes with out-of-phase components will be cancelled when the data from the six accelerometers in one ring are averaged at a single point in time. The result is the amplitude of the breathing mode, still in the time domain. The time signal is then transformed into the frequency domain by calculating the power spectral density (PSD) using the pwelch command in MATLAB [23]. The default parameters are used for this command, where the signal data is divided into eight segments and a hamming window is applied to each segment, there is 50% overlap, and the length of the FFT is specified by the segment length.

The second method requires frequency response functions (FRFs) in order to establish the phase differences between the signal data acquired by each of the six accelerometers. The FRF's are calculated with the following expression [20],

$$H_{xy}(f) = \frac{G_{xy}(f)}{G_{xx}(f)}, \tag{4.2.1}$$

where

$$G_{xy} = \overline{X^*(f)Y(f)}, \tag{4.2.2}$$

and X and Y are the force and acceleration linear spectrums. As the input force is unknown in the case of operational data, the 'first' accelerometer is arbitrarily chosen to act as a reference X. The function H_{xy} is scaled by $|G_{xy}|^{1/2}$ to give the FRF spectral character. As described by Bonness, Fahnline and Jenkins [21], a discrete spatial Fourier Transform (DFT) of the scaled FRF is taken at each frequency,

$$H_n(f) = \frac{1}{N}\sum_{y=1}^{N} H_{xy}(f)e^{-i2\pi(n-1)(y-1)/N} \tag{4.2.3}$$

and the total energy is computed by summing the energy of the corresponding positive and negative components of H_n,

$$|H_k(f)| = \sqrt{|H_{-n}(f)|^2 + |H_{+n}(f)|^2}. \tag{4.2.4}$$

The result is the amplitude of the first $N/2$ modes. Therefore, with six accelerometers, we can use this modal decomposition technique to calculate the amplitudes of the $n = 0, 1, 2, 3$ modes. Figure 4.6 shows an example of the results of the modal decomposition technique. The higher order modes have larger acceleration amplitude than the $n = 0$ breathing mode, which is easily observed in Figure 4.6.

Computing the amplitude from the $n = 0$ breathing mode by two different methods provides another chance to check the accuracy of the measurements and calculations. An example of the type of agreement observed is shown in Figure 4.7 with a closer look in Figure 4.8.

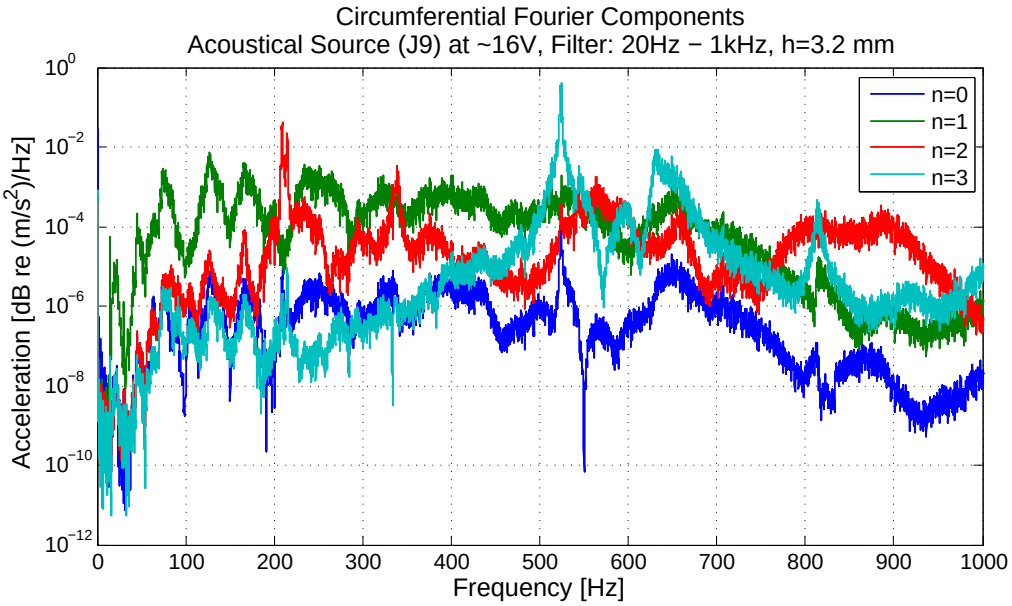

Figure 4.6. Result of modal decomposition for a ring of six accelerometers.

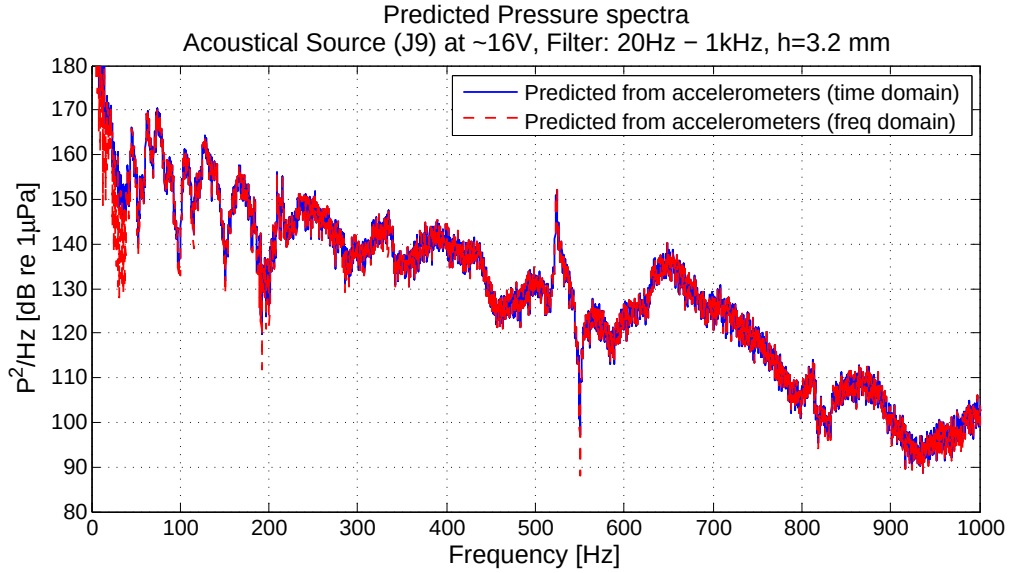

Figure 4.7. Comparison of predicted pressure for the two methods of calculating the $n = 0$ breathing mode amplitude.

The $n = 0$ amplitude computed in the time domain was consistently less noisy than the amplitude computed in the frequency domain, and is therefore the amplitude calculation used in the presented results. However, for each measurement, the agreement between the amplitude calculated from both methods was good.

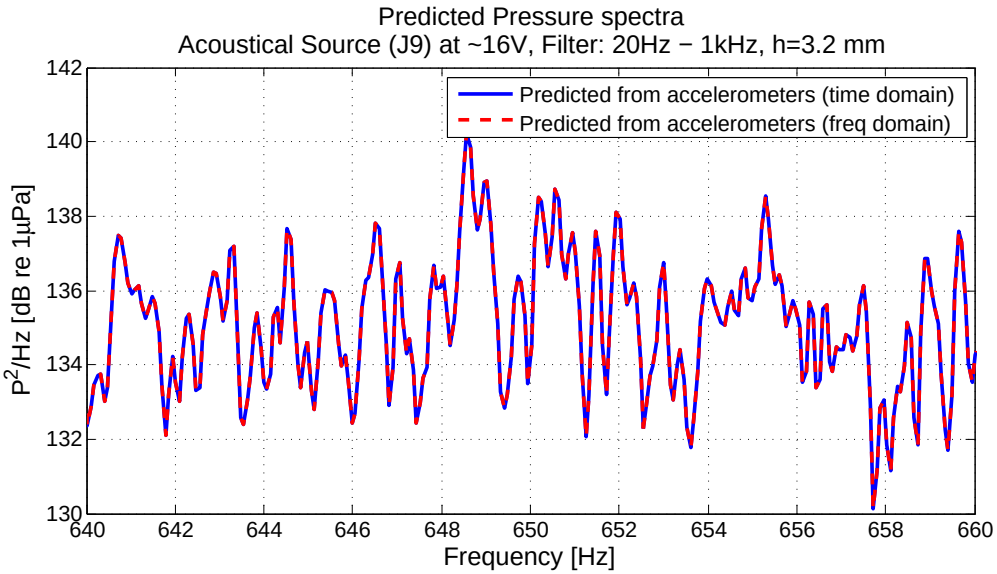

Figure 4.8. A closer look at the agreement between the two pressure calculations.

4.2.2 Calculating pressure

The internal pressure is directly related to the radial displacements contributed by the $n = 0$ breathing mode. The $n = 0$ amplitude calculated thus far is described in terms of acceleration. Assuming time-harmonic motion, the displacement is calculated by dividing the acceleration by the square of the angular frequency. As developed in Section 2.5 and presented in Equation (2.5.4), the pressure is then calculated as a function of the displacement as follows,

$$P = \frac{Eh}{a^2(1-\nu^2)} \left[-\frac{\rho_f}{\rho_s} \frac{a}{h} \frac{2}{\psi - \zeta_a^2} \right] W_{n=0} \tag{4.2.5}$$

where $\psi = (c_s/c_f)^2$ and $\zeta_a^2 = \psi + \left(2(\rho_f/\rho_s)(a/h) + \nu^2\right) / \left(1-\nu^2\right)$. The character of the calculated pressure, is determined solely by the displacement of the $n = 0$ breathing mode, as the other components of the calculation are constants defined by the material and geometry of the piping system and its contained fluid.

4.2.3 Comparing the direct and indirect pressure measurements

The direct measurements of pressure acquired with the wall pressure sensors are converted into the frequency domain using the pwelch command in MATLAB [23] with the same parameters as described previously. The data from the three pressure sensors is then averaged at each frequency. This direct measurement of pressure is taken as the actual acoustic pressure level and compared to the indirect measurement of pressure (using the ring of accelerometers) to determine the accuracy of the indirect method. Another comparison is made between the accuracy of the indirect method using the accelerometer ring mounted on the thin portion of the pipe versus the accelerometer ring mounted on the thick portion of the pipe.

Data was collected at different levels of pressure when the pipe was being excited by the acoustical J9-projector source. The voltage input was increased in order to increase the acoustic pressure in the pipe. An average difference between pressure levels over 10 Hz frequency bands was calculated for both the indirect and direct measurement of pressure. With this data, the performance of the accelerometer ring in detecting large pressure changes can be calculated and compared to the pressure changes monitored by the direct pressure sensors. The results of these comparisons are presented in Section 4.3.

4.3 Results

The results in this section are used to determine the accuracy of the non-invasive method by comparing the calculated pressure using a ring of accelerometers to the direct measurement of the internal acoustic pressure. First, the results from driving the pipe with the acoustical source (J9 projector) are presented. The performance of the accelerometer

ring is assessed in its ability to monitor the pressure level as well as accurately calculate the change in pressure level.

The results from driving the pipe with a mechanical source will also be presented. The response to two different excitations were measured. The F4 shaker as described previously, was a controlled source. The second excitation was a transient source created by axially striking a pipe flange about 7.6 m away from the test section with a metal tool. Both excitations produced good results. For each of the three excitations (acoustical, mechanical and transient mechanical), a comparison is also made between the performance of the accelerometer ring on the thick pipe wall to the accelerometer ring on the thin pipe wall.

The results are presented, for each excitation source, with two figures. The first figure plots the pressure level in dB for both the direct and indirect measurements of pressure. This allows for an easy visual comparison of the two methods. The second figure plots the calculated dB difference between the two levels to determine the accuracy of the calculation of pressure from the ring of accelerometers. These two figures plot the narrow band pressure levels. These same two plots are generated also for the one-third-octave band frequencies.

4.3.1 Acoustical Source

A J9 acoustic projector was chosen to act as the acoustical source, with it's piston face driven with gaussian noise over the freqeuency range from 20 Hz to 1000 Hz. Figures are presented for the case when the J9 input voltage is about 16 Volts. Figures 4.9 and 4.10 present the narrow band response of the accelerometer ring mounted to the thick portion of the test section and the one-third-octave band plots are presented in Figures 4.11 and 4.12. Figures 4.13 and 4.14 present the narrow band response of the accelerometer ring

mounted to the thin portion of the test section and the one-third-octave band plots are presented in Figures 4.15 and 4.16. The average pressure directly-measured by the wall pressure sensors is the same for both cases of thickness, as all measurements were taken simultaneously.

At first glance, the comparison of the direct and indirect measurements of pressure presented in Figures 4.9 and 4.13 seem to agree fairly well. However, a closer look at the difference between the two quantities presented for both cases of thickness by Figures 4.10 and 4.14 shows that a large percentage of the frequency range produces unacceptable levels if the desired error is to be less than 5 dB. On the other hand, the character of the predicted pressure matches that of the actual pressure if the frequencies below 200 Hz are neglected. Below 200 Hz, the predicted pressure deviates from the directly-measured pressure by a significant amount, making the indirect measurement of pressure using a ring of accelerometers invalid at these low frequencies.

The one-third-octave band plots more clearly present the results and confirm the previous observations. When the pipe wall is 7.1 mm thick (Figure 4.11), the predicted pressure matches the measured pressure very well above 300 Hz. The difference between pressures above 300 Hz is less than 5 dB as shown in Figure 4.12. In the case of the thinner pipe wall, the pressures match well for frequencies between 300 Hz and 500 Hz (Figure 4.11), but the difference between the pressure increases with increasing frequency (Figure 4.16).

When comparing the results for the two cases of pipe wall thickness, the accelerometers mounted on the thin portion of the test section predict the character of the pressure more accurately than the accelerometers mounted on the thick portion of the test section, although the difference between pressures is less for the accelerometers mounted on the thick portion of the test section. Although the displacements of the thin wall are larger

than the thick wall and possibly easier for the accelerometers to detect, the pressure sensors are located closer to the accelerometers on the thick wall, which may account for the small offset between the measured and predicted pressure using accelerometers on the thin wall. With the exception of a few peaks, the difference between the direct and indirect measurement of pressure is less than 10 dB as can be seen in Figures 4.10 and 4.14. Yet, if this method is to be used as an absolute measurement of pressure, the valid range of frequencies must be improved as well as the method's ability to more accurately measure the internal pressure on thicker pipes, as industrial pipes more commonly have thicker walls.

It is clearly observed that the difference between the predicted and measured pressure levels significantly increase for frequencies below 200 Hz. Since the noise generated by the J9 projector is filtered from 20 Hz to 1000 Hz, the results below 20 Hz can be disregarded. The radial displacement detected by the accelerometers is smaller at lower frequencies. A clear increase from 20 Hz to about 50 Hz can be observed when the radial displacements are plotted for each accelerometer (Figure 4.17). This suggests that the displacements may be too small to be accurately measured by the accelerometers. However, if the signal to noise ratio increased in this frequency range as it may for different more powerful excitations, the measurements may improve. The measured pressure is also less stable for lower frequencies, making it more difficult for the prediction of pressure to accurately match the non-steady state pressures. The difference between the predicted and measured pressure is more accurate when the measured pressure is more stable. This may suggest that there could be errors that also exist in the measured pressure due to the hydrophone's sensitivity to pipe wall accelerations or the proximity of the hydrophone measurements to the location of the accelerometer ring.

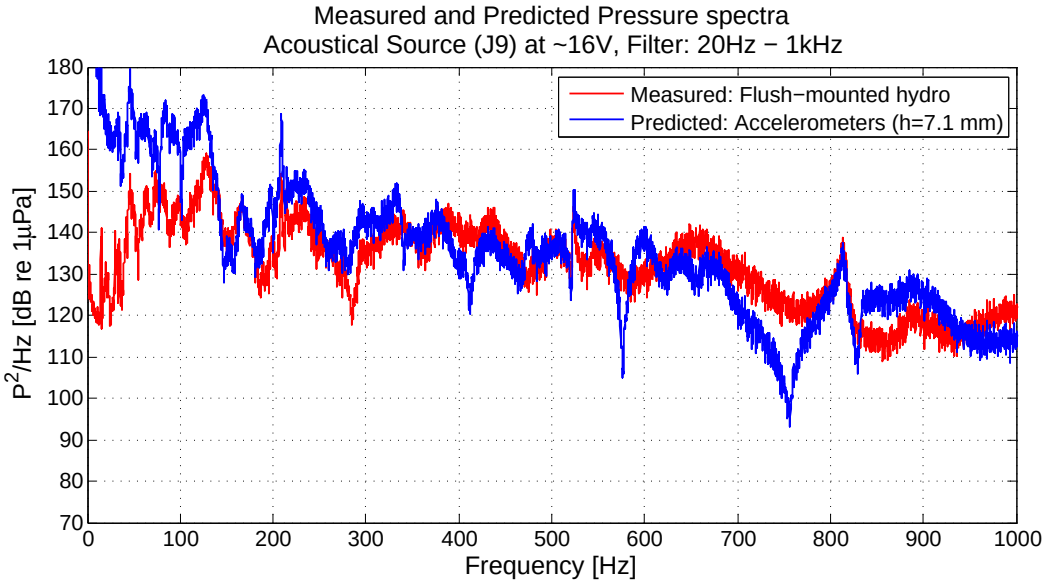

Figure 4.9. Internal sound pressure level as a result of measurements taken on the thick portion of the test section when the pipe is driven by the J9 acoustic projector.

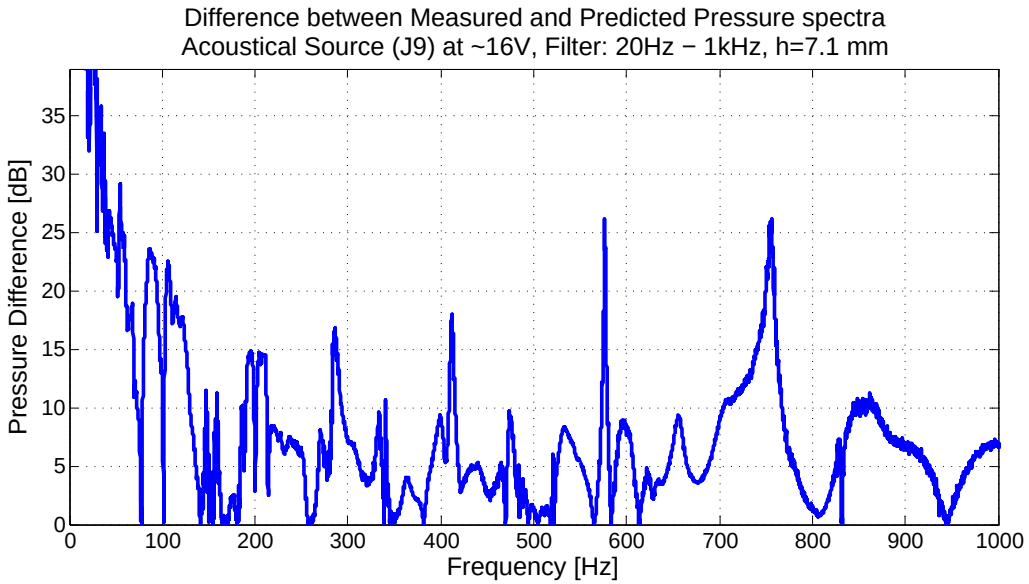

Figure 4.10. Difference between the measured and calculated internal pressure levels, as a result of measurements taken on the thick portion of the test section when the pipe is driven by the J9 acoustic projector.

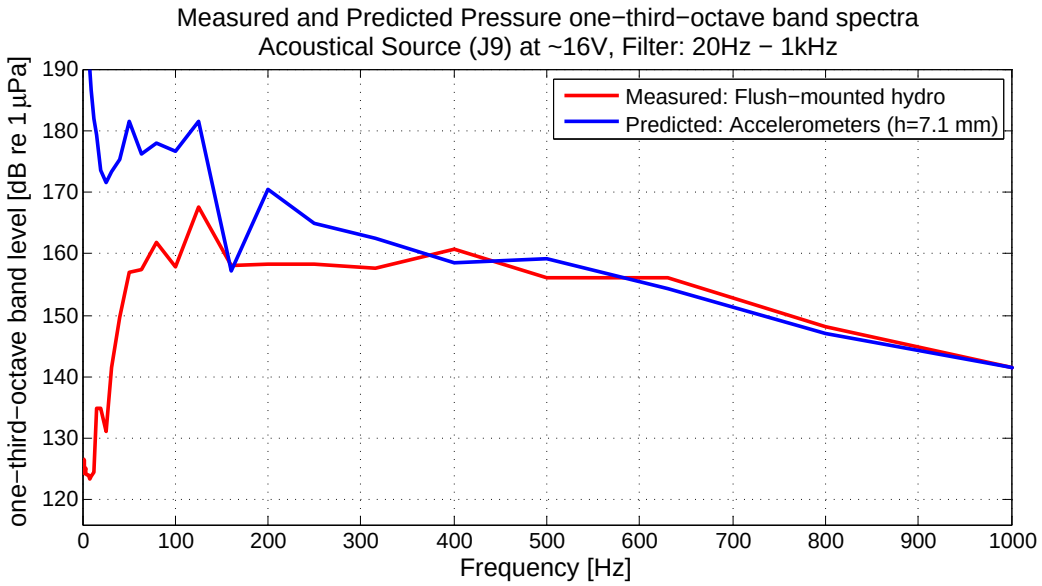

Figure 4.11. One-third-octave band internal sound pressure level as a result of measurements taken on the thick portion of the test section when the pipe is driven by the J9 acoustic projector.

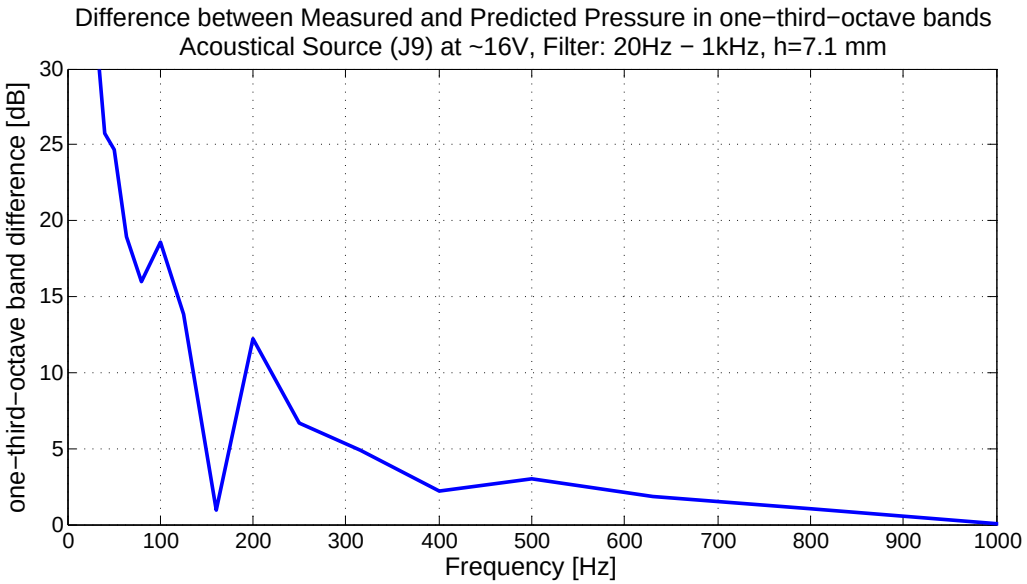

Figure 4.12. One-third-octave band dB difference between the measured and calculated internal pressure levels, as a result of measurements taken on the thick portion of the test section when the pipe is driven by the J9 acoustic projector.

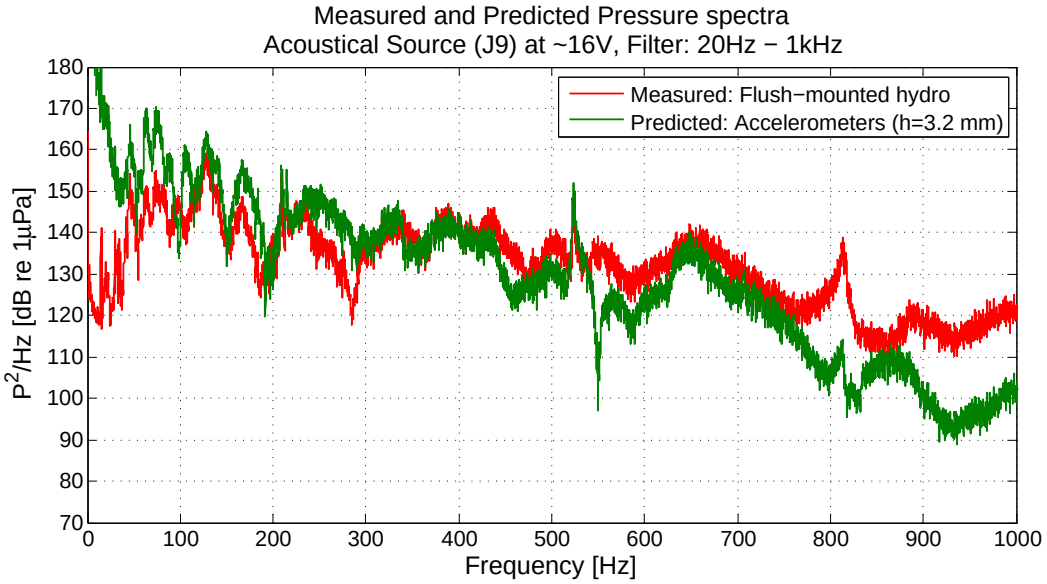

Figure 4.13. Internal sound pressure level as a result of measurements taken on the thin portion of the test section when the pipe is driven by the J9 acoustic projector.

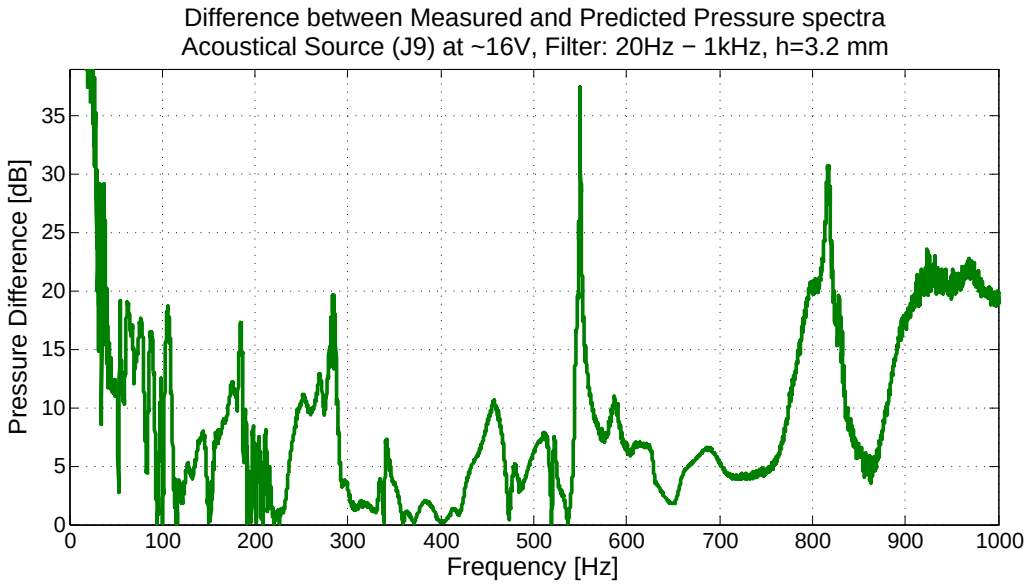

Figure 4.14. Difference between the measured and calculated internal pressure levels, as a result of measurements taken on the thin portion of the test section when the pipe is driven by the J9 acoustic projector.

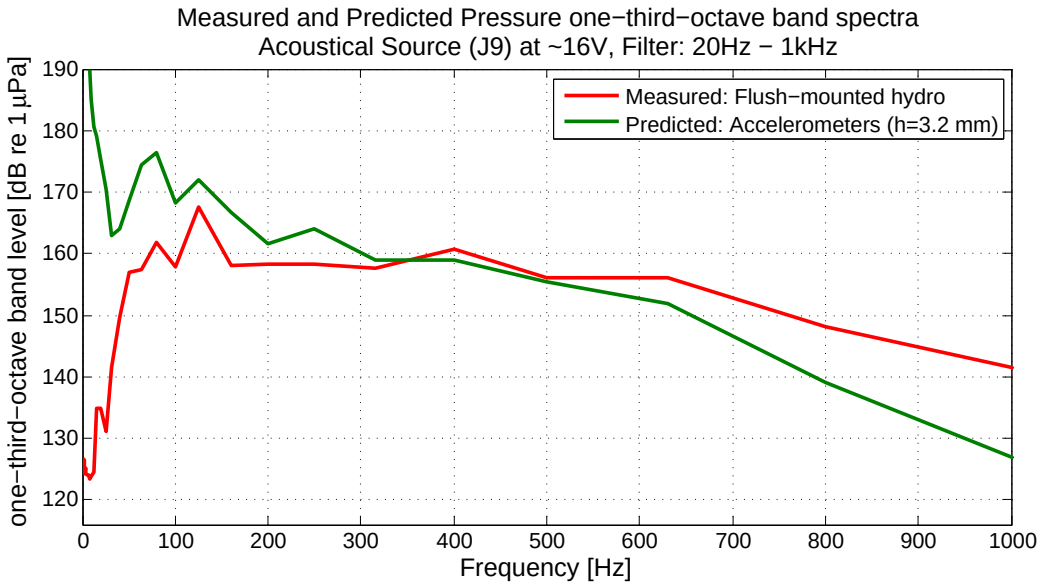

Figure 4.15. One-third-octave band internal sound pressure level as a result of measurements taken on the thin portion of the test section when the pipe is driven by the J9 acoustic projector.

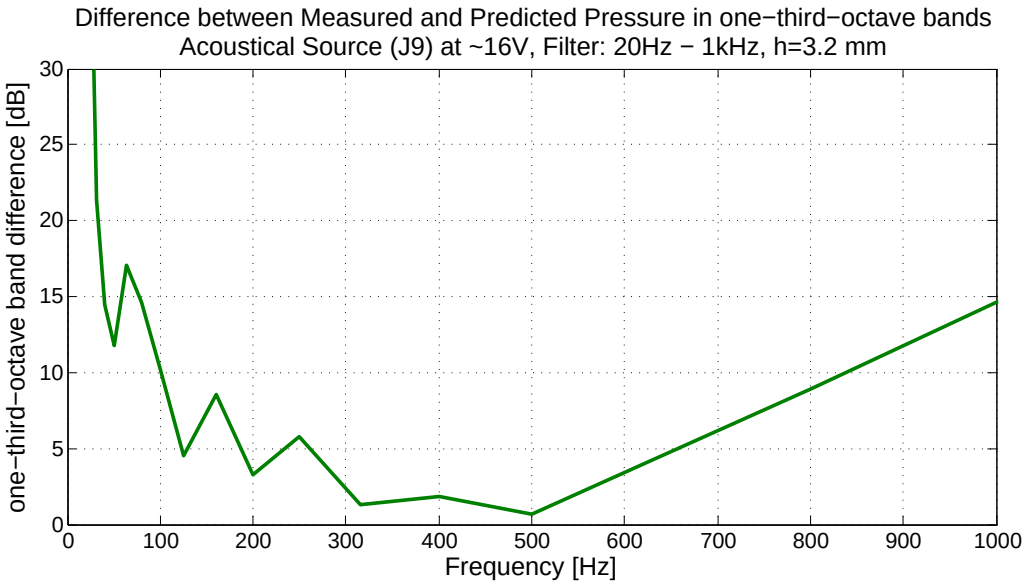

Figure 4.16. One-third-octave band dB difference between the measured and calculated internal pressure levels, as a result of measurements taken on the thin portion of the test section when the pipe is driven by the J9 acoustic projector.

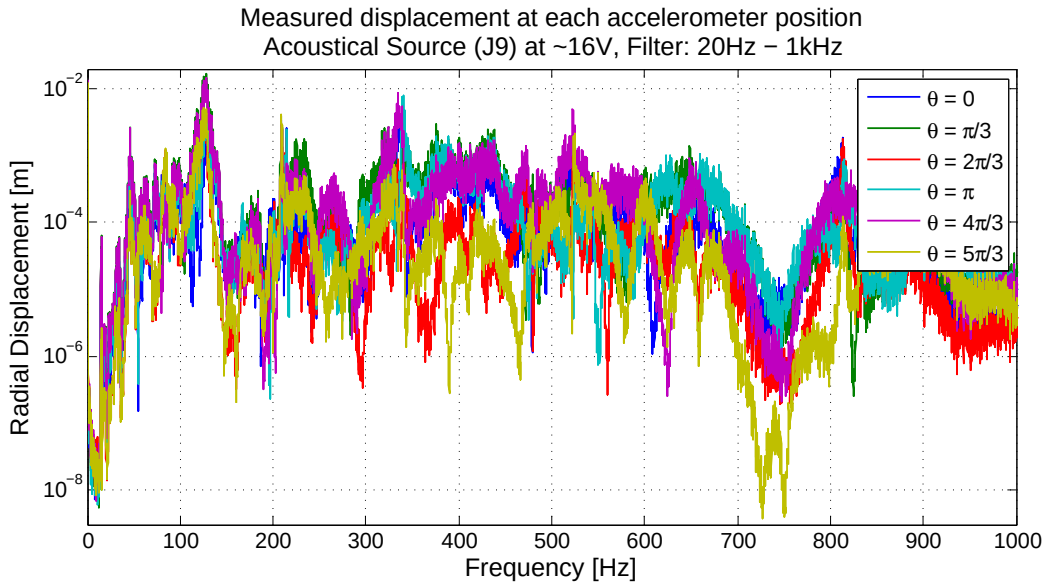

Figure 4.17. The spectra of radial displacement (acceleration/ω^2) measured by each accelerometer when the pipe is driven by the J9 acoustic projector.

4.3.1.1 Pressure tracking

The desired outcome of this research is to develop an indirect method for monitoring the acoustic pressure in pipes in order to detect any fatigue throughout its lifespan. If an absolute measurement of the internal acoustic pressure is desired within 5 dB, a ring of accelerometers may not have the ability to predict the pressure that precisely. However, the ring of accelerometers can monitor the fluctuations in pipe pressure fairly accurately. As mentioned previously, the character of the indirect measurement of pressure using the ring of accelerometers matches the character of the direct measurement of pressure fairly well. Therefore, if the internal pressure is increased or decreased by a significant amount, the indirect measurement should be able to accurately detect the change in pressure when compared to the actual change in pressure.

Measurements were taken at three different levels of pressure, which was controlled through changes in the voltage level to the J9 projector. The previous plots were mea-

sured when the J9 projector was driven at about 16 Volts. The additional pressure levels were measured when the J9 projector was driven at about 8 or 4 Volts. The pressure level measured at an input voltage of 16 V is compared to the two lower pressure levels in Figures 4.18 and 4.21. The change in pressure is noted on these figures and plotted over the entire frequency range in Figures 4.19 , 4.20, 4.22 and 4.23, which present the change in pressure level monitored by the indirect measurement of pressure in comparison to the direct measurement of pressure. The change in pressure level is tracked extremely well by this method at most frequencies in the range of interest. As expected, the accelerometers mounted on the thin portion of the test section result in more accurate calculations of the pressure change. With the exception of a few deviations at higher frequencies, the indirect measurement of pressure utilizing a ring of accelerometers is successful in accurately predicting changes of the internal acoustic pressure level.

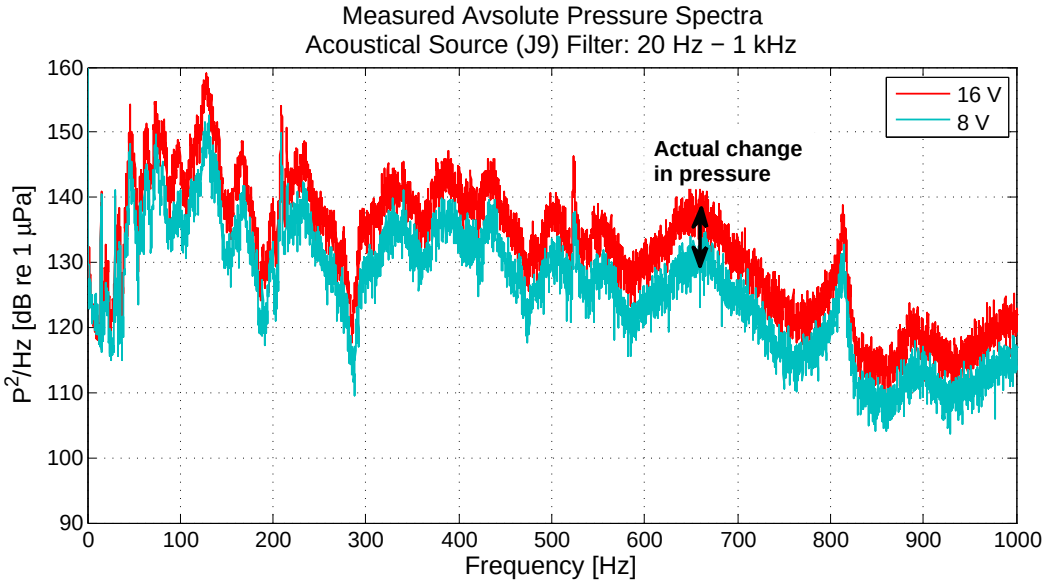

Figure 4.18. Measured absolute pressure levels at varying acoustical J9 projector input voltages.

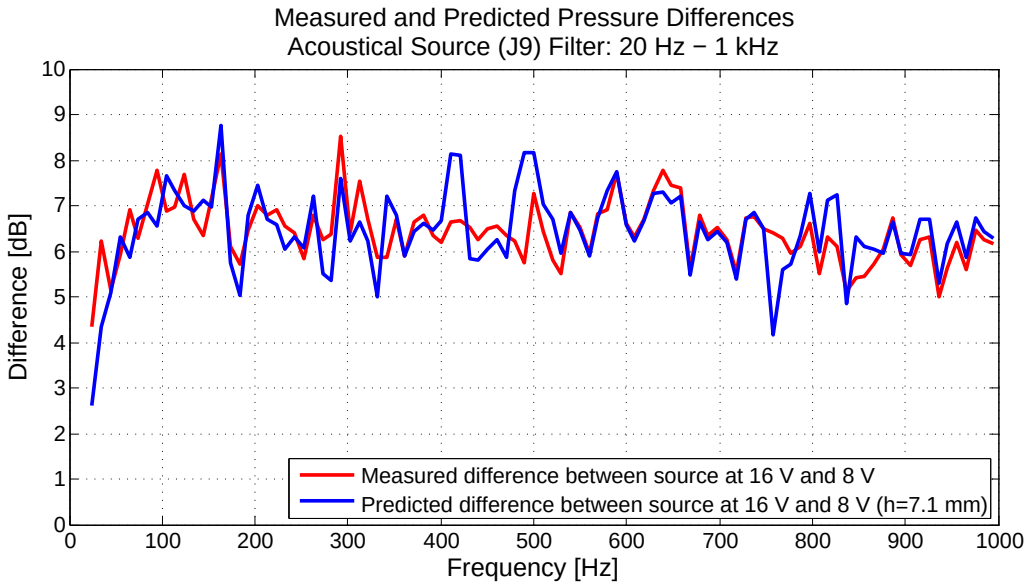

Figure 4.19. Measured and calculated change in pressure as a result of measurements taken on the thick portion of the test section when the pipe is driven by the J9 acoustic projector.

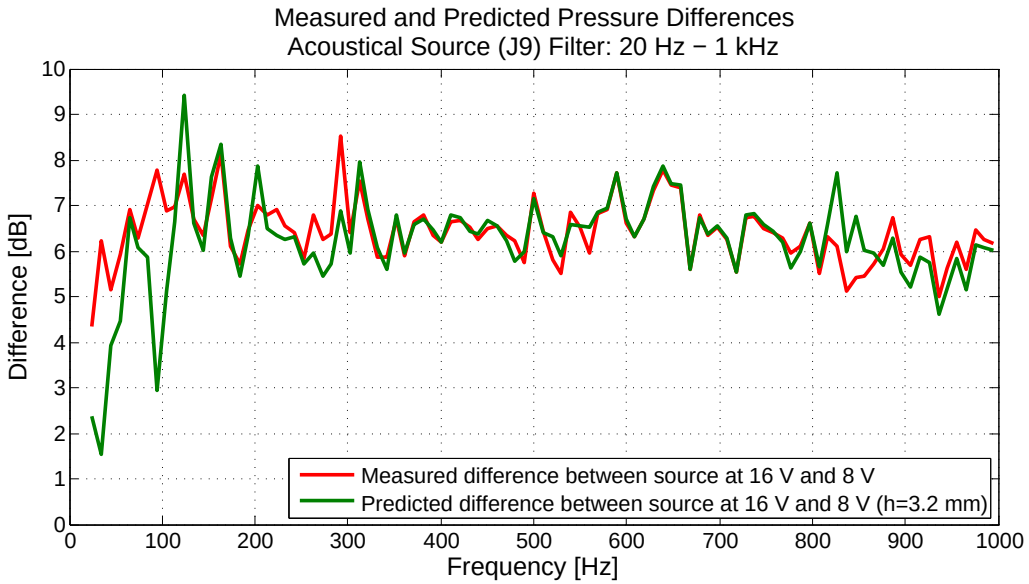

Figure 4.20. Measured and calculated change in pressure as a result of measurements taken on the thin portion of the test section when the pipe is driven by the J9 acoustic projector.

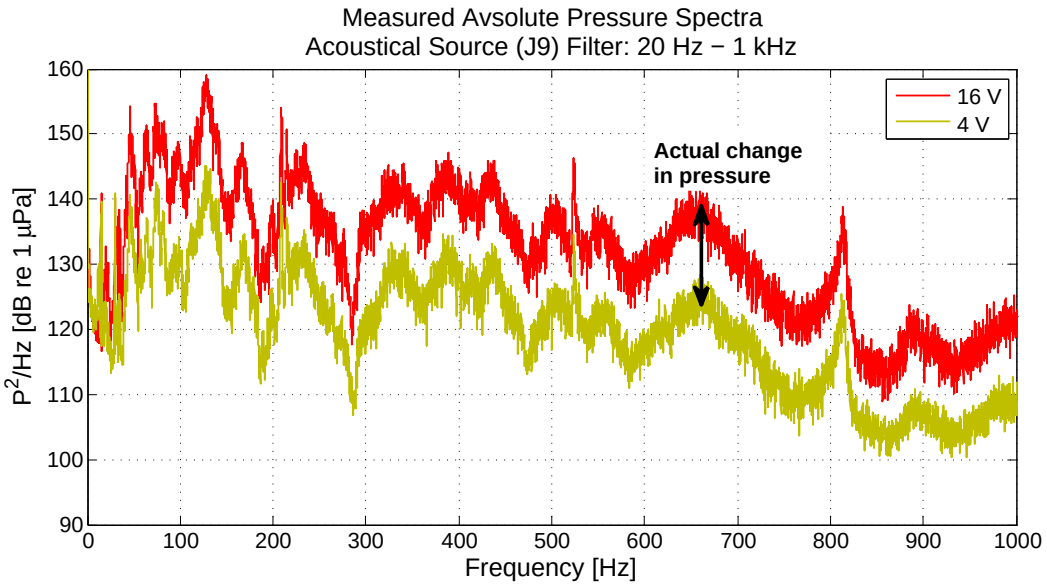

Figure 4.21. Measured absolute pressure levels at varying acoustical J9 projector input voltages.

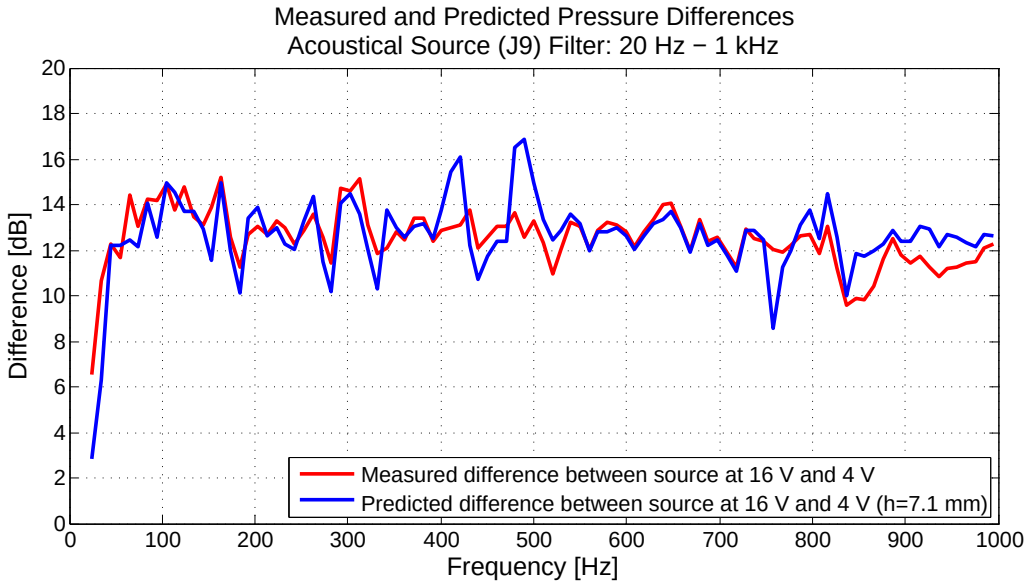

Figure 4.22. Measured and calculated change in pressure as a result of measurements taken on the thick portion of the test section when the pipe is driven by the J9 acoustic projector.

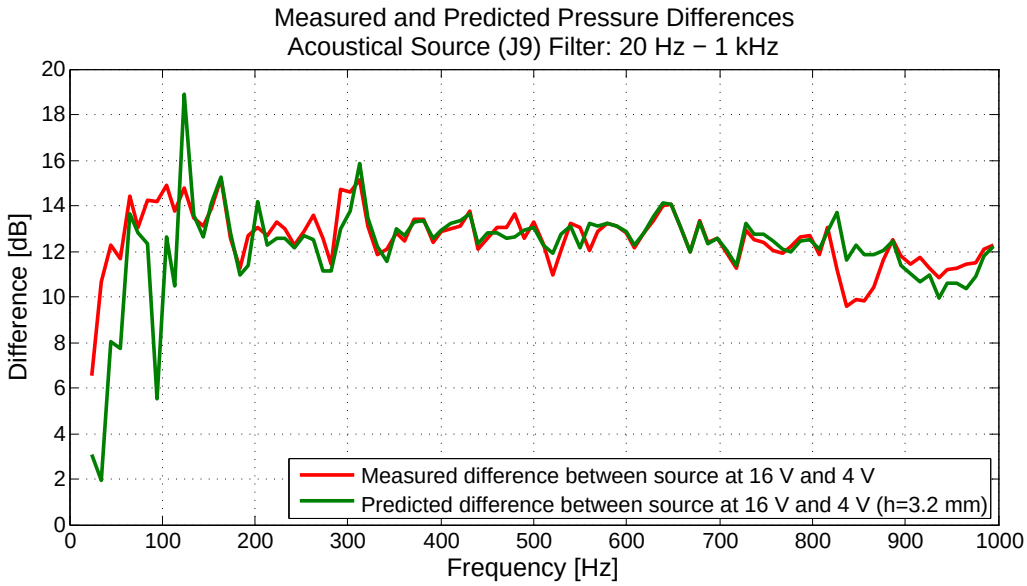

Figure 4.23. Measured and calculated change in pressure as a result of measurements taken on the thin portion of the test section when the pipe is driven by the J9 acoustic projector.

4.3.2 Mechanical Source

Driving the pipe with a mechanical source results in similar conclusions about the accuracy of the indirect method of measuring pressure utilizing a ring of accelerometers as when the pipe was driven with an acoustical source. The large error at low frequencies is consistently present in the range below 200 Hz. Similar to the results produced using an acoustical source, the small displacements at low frequencies (seen in Figures 4.24 and 4.25) and the non-steady nature of the pressure at low frequencies may contribute to the large errors seen in the frequency range below 200 Hz. In general, for frequencies above 200 Hz, the character of the pressure is tracked very well. Again, an absolute measurement of pressure within 5 dB of the actual pressure may not be possible at this time, but the method shows promise in its ability to monitor the pressure levels and fluctuations in pressure.

Two types of mechanical sources were measured. The results of the first source, an F4

electromagnetic shaker, are shown in Figures 4.26, 4.27, 4.30 and 4.31. The results of the second source, where a pipe flange is struck axially with a metal tool about 7.6 m away from the test section, are shown in Figures 4.34, 4.35, 4.38 and 4.35. For both sources of mechanical excitation, the case of a thicker pipe wall results in a more accurate prediction of pressure. This is clearly observed in the four one-third-octave band dB difference plots (Figures 4.29, 4.33, 4.37, and 4.41).

Although the thinner pipe wall case performs fairly well, there is a small offset that makes the difference slightly larger in comparison to the case of the thicker pipe wall. Again, this small offset may be attributed to the fact that the pressure sensors are farther away from this measurement location than for the measurement location on the thick wall. It would be expected that the thinner pipe wall would give an even more accurate prediction of pressure if compared to pressure measurements made closer to the location of these accelerometers.

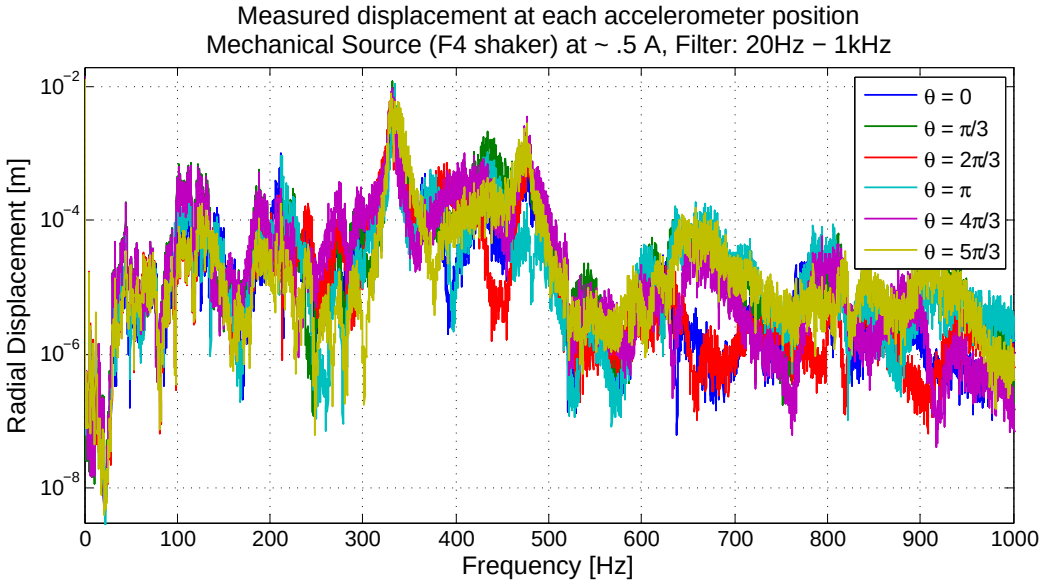

Figure 4.24. The spectra of radial displacement (acceleration/ω^2) measured by each accelerometer when the pipe is driven by the F4 electromagnetic shaker.

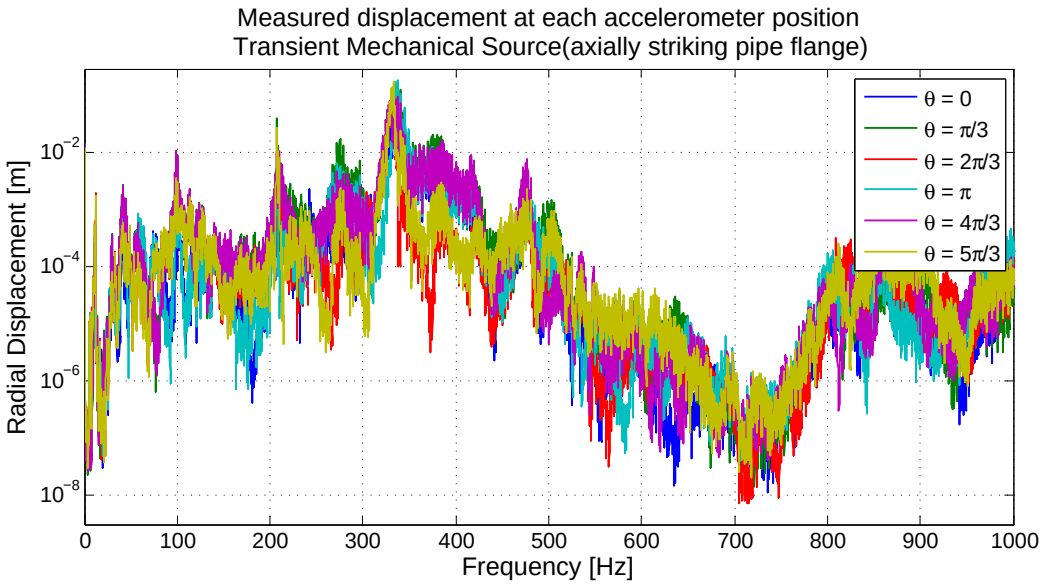

Figure 4.25. The spectra of radial displacement (acceleration/ω^2) measured by each accelerometer when the pipe is driven by the transient mechanical source.

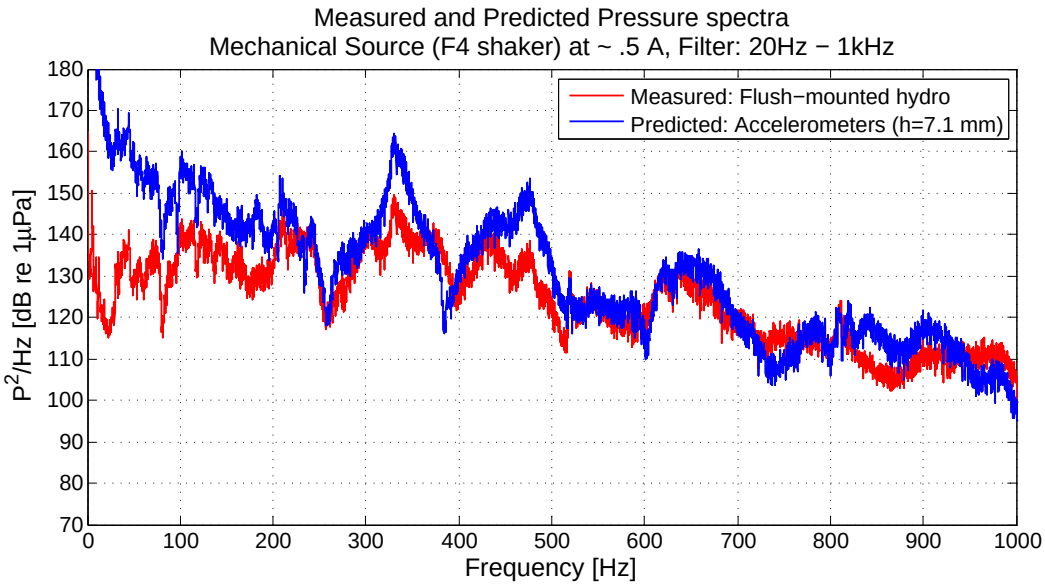

Figure 4.26. Sound pressure level as a result of measurements taken on the thick portion of the test section when the pipe is driven by the F4 electromagnetic shaker.

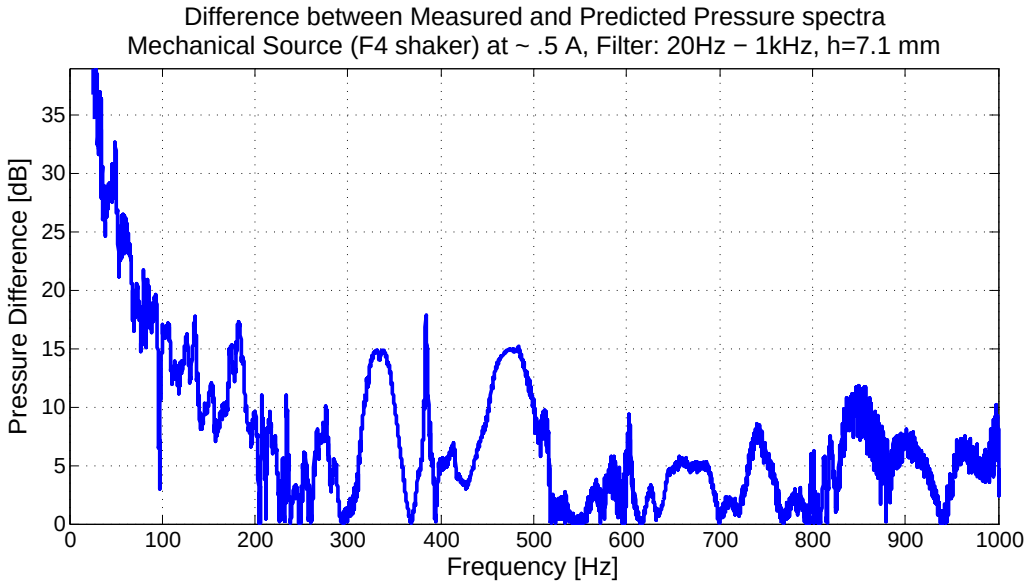

Figure 4.27. Difference between the measured and calculated pressure levels, as a result of measurements taken on the thick portion of the test section when the pipe is driven by the F4 electromagnetic shaker.

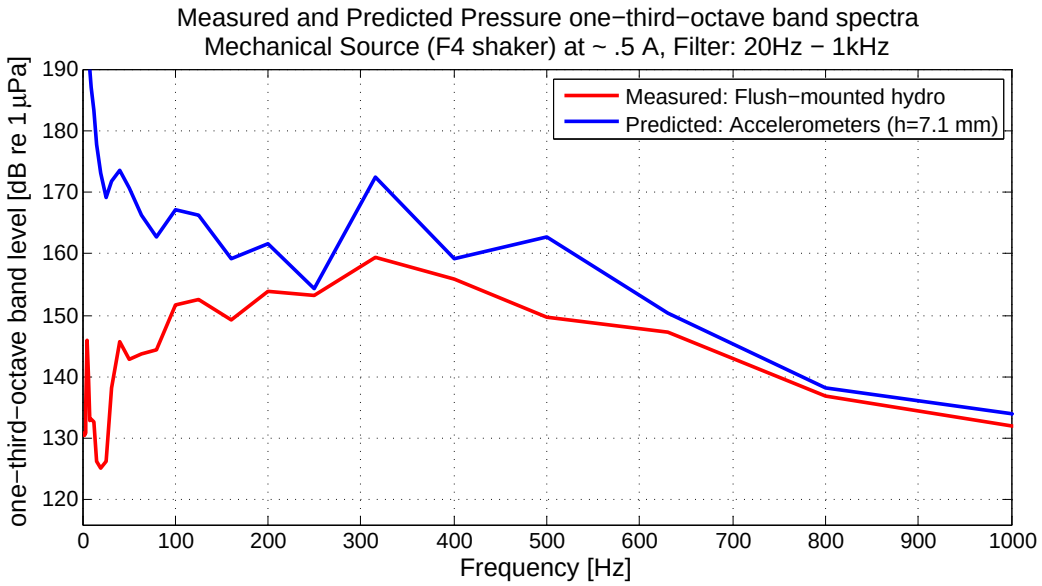

Figure 4.28. One-third-octave band sound pressure level as a result of measurements taken on the thick portion of the test section when the pipe is driven by the F4 electromagnetic shaker.

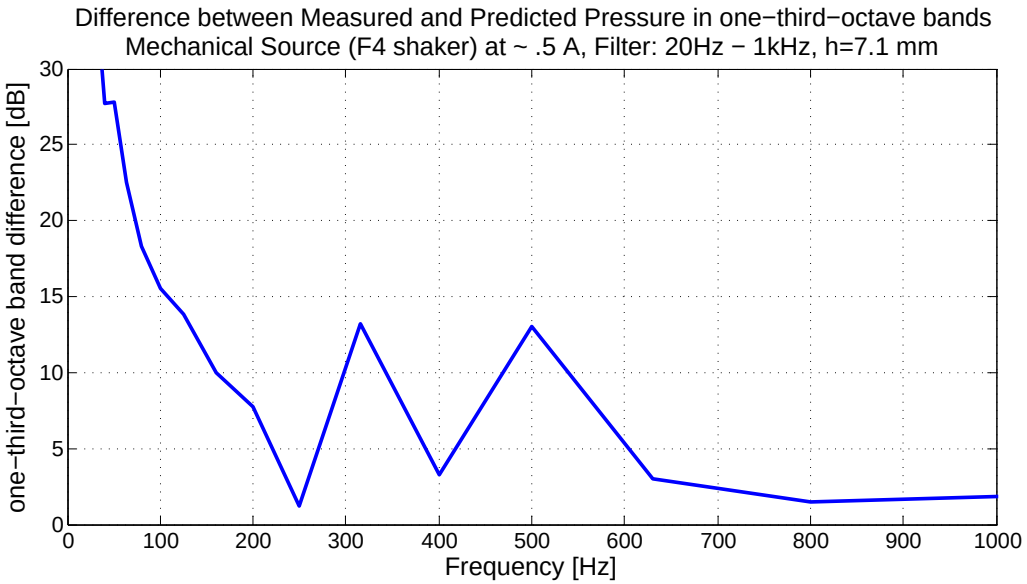

Figure 4.29. One-third-octave band dB difference between the measured and calculated pressure levels, as a result of measurements taken on the thick portion of the test section when the pipe is driven by the F4 electromagnetic shaker.

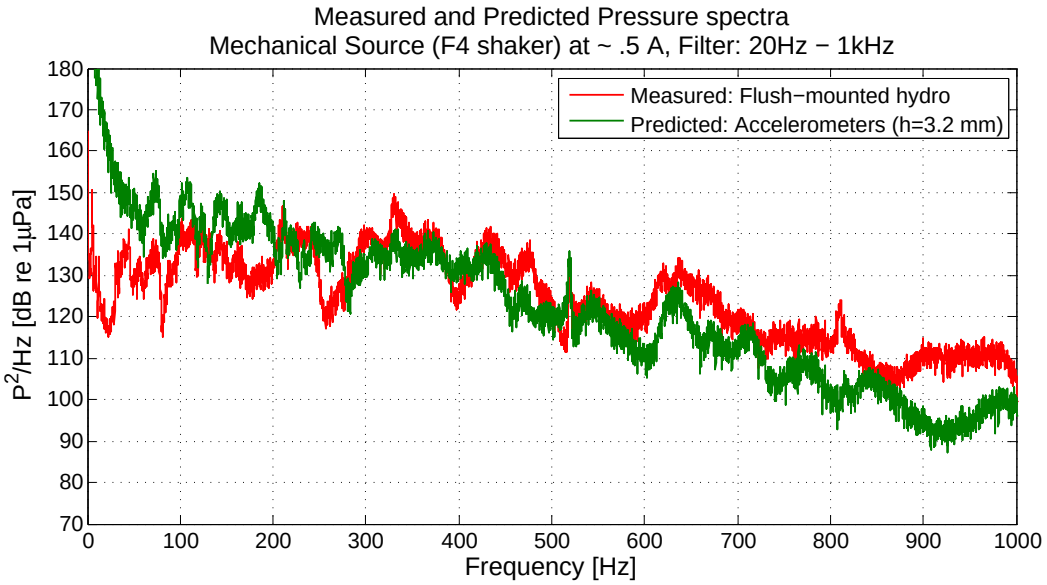

Figure 4.30. Sound pressure level as a result of measurements taken on the thin portion of the test section when the pipe is driven by the F4 electromagnetic shaker.

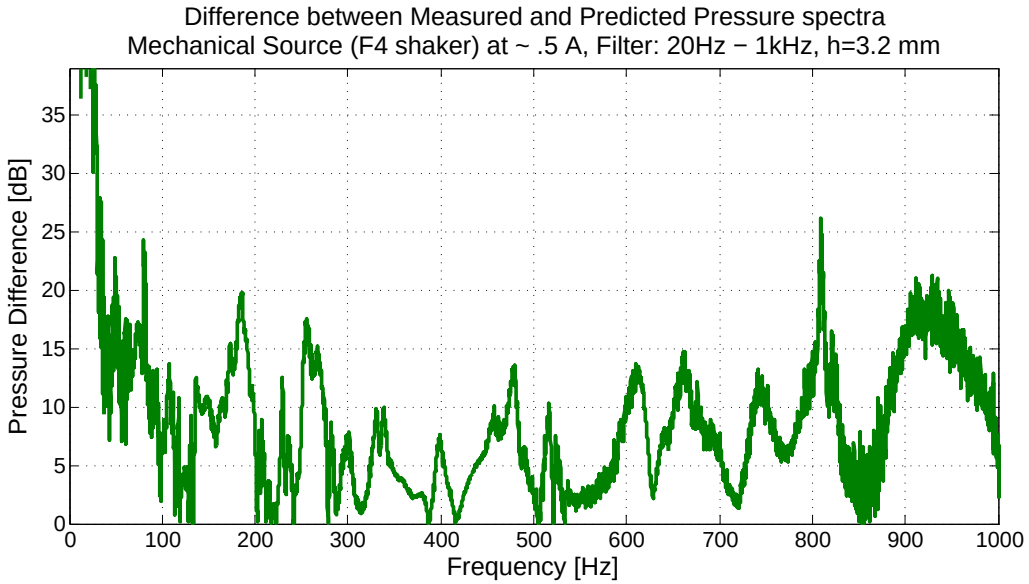

Figure 4.31. Difference between the measured and calculated pressure levels, as a result of measurements taken on the thin portion of the test section when the pipe is driven by the F4 electromagnetic shaker.

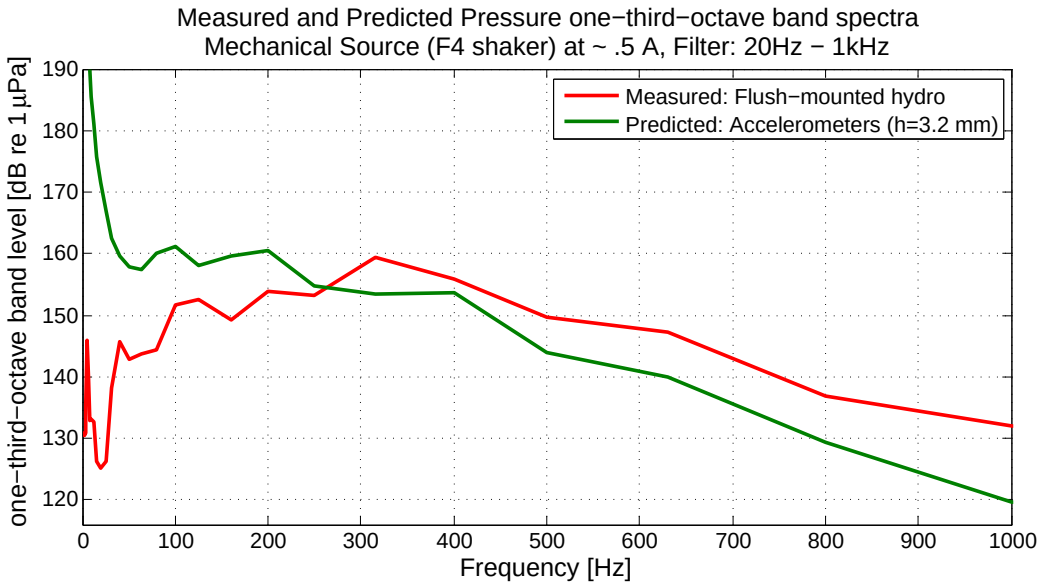

Figure 4.32. One-third-octave band sound pressure level as a result of measurements taken on the thin portion of the test section when the pipe is driven by the F4 electromagnetic shaker.

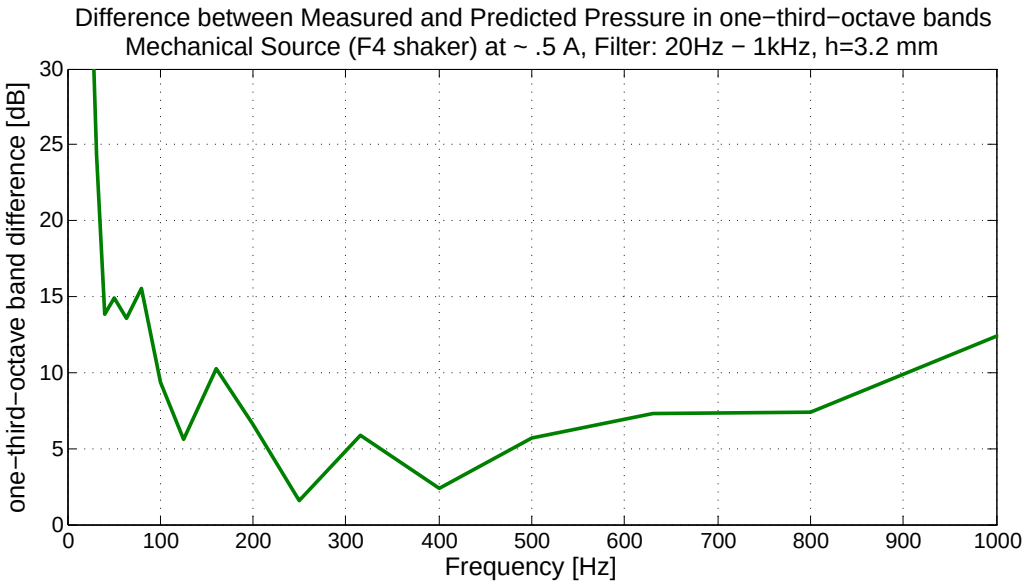

Figure 4.33. One-third-octave band dB difference between the measured and calculated pressure levels, as a result of measurements taken on the thin portion of the test section when the pipe is driven by the F4 electromagnetic shaker.

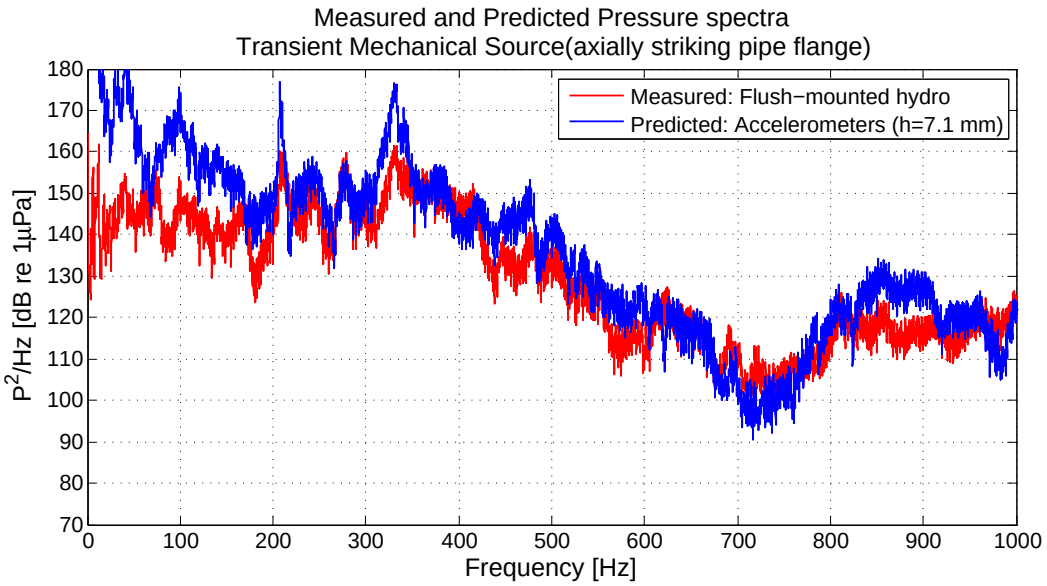

Figure 4.34. Sound pressure level as a result of measurements taken on the thick portion of the test section when the pipe is driven by the transient mechanical source.

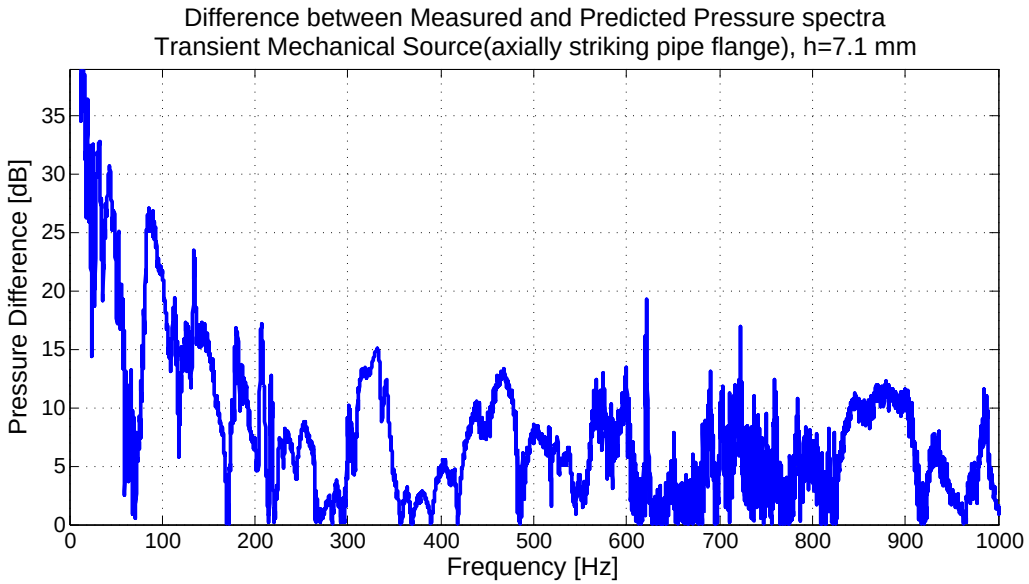

Figure 4.35. Difference between the measured and calculated pressure levels, as a result of measurements taken on the thick portion of the test section when the pipe is driven by the transient mechanical source.

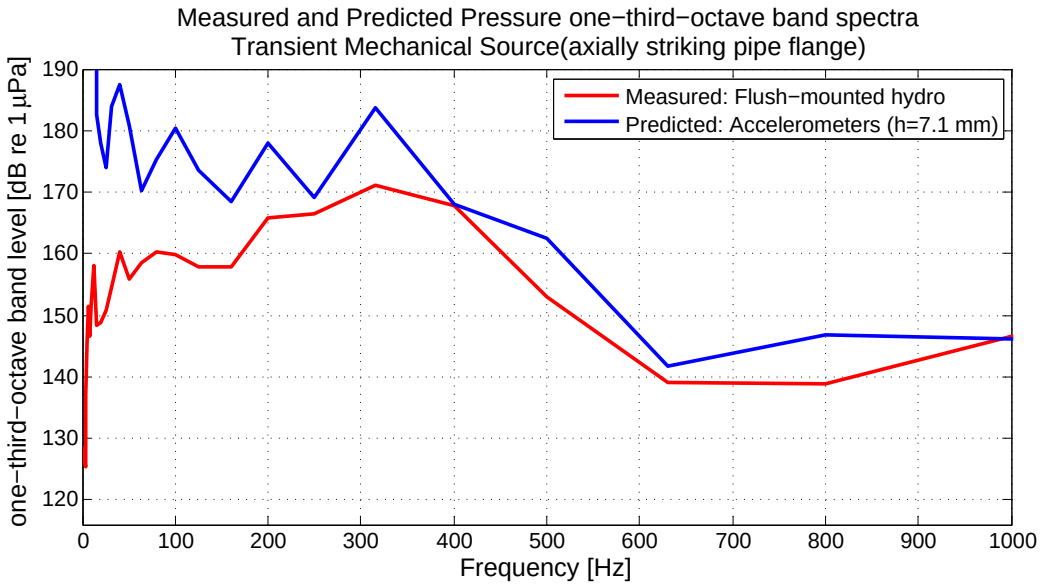

Figure 4.36. One-third-octave band sound pressure level as a result of measurements taken on the thick portion of the test section when the pipe is driven by the transient mechanical source.

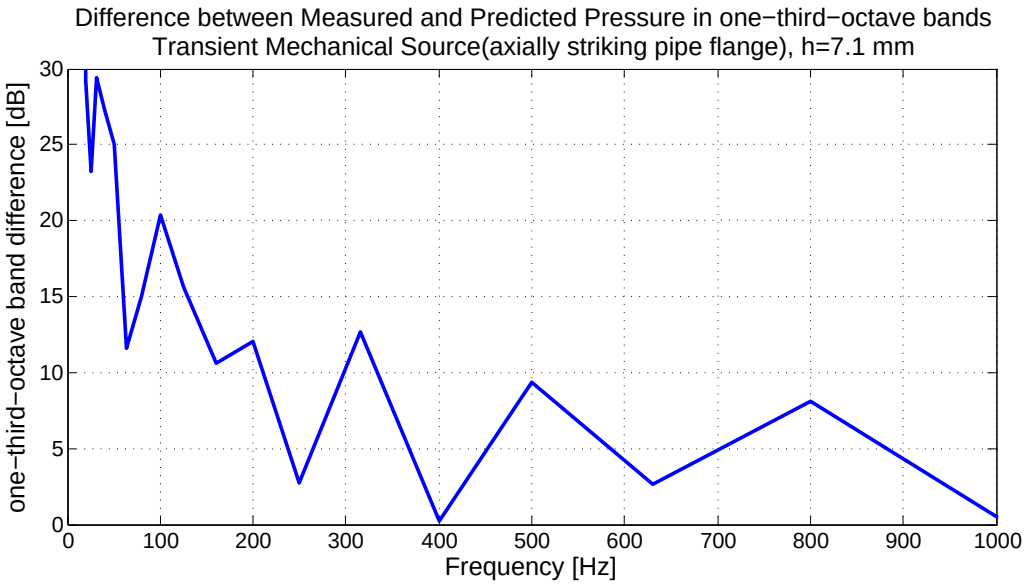

Figure 4.37. One-third-octave band dB difference between the measured and calculated pressure levels, as a result of measurements taken on the thick portion of the test section when the pipe is driven by the transient mechanical source.

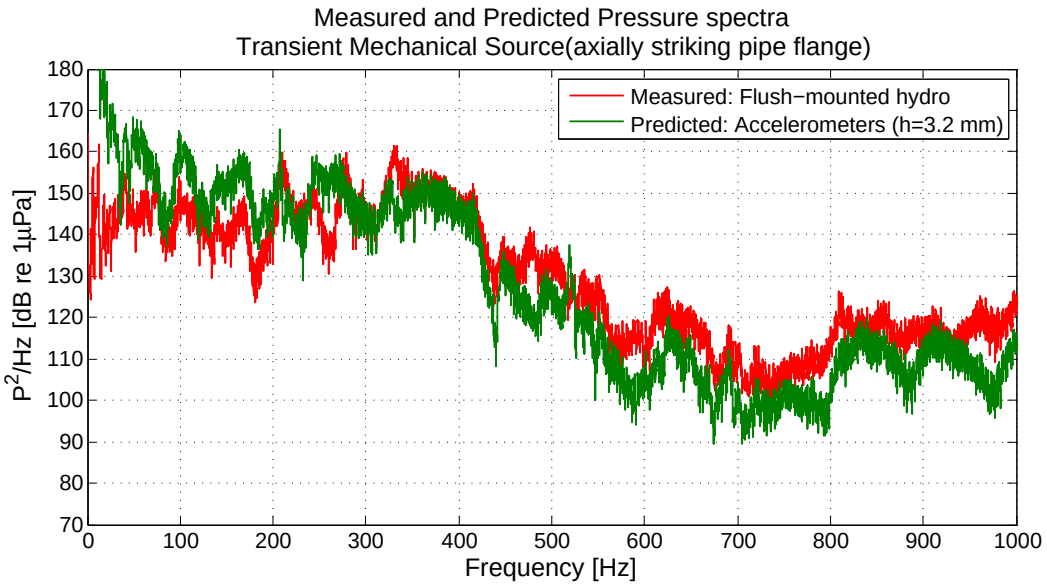

Figure 4.38. Sound pressure level as a result of measurements taken on the thin portion of the test section when the pipe is driven by the transient mechanical source.

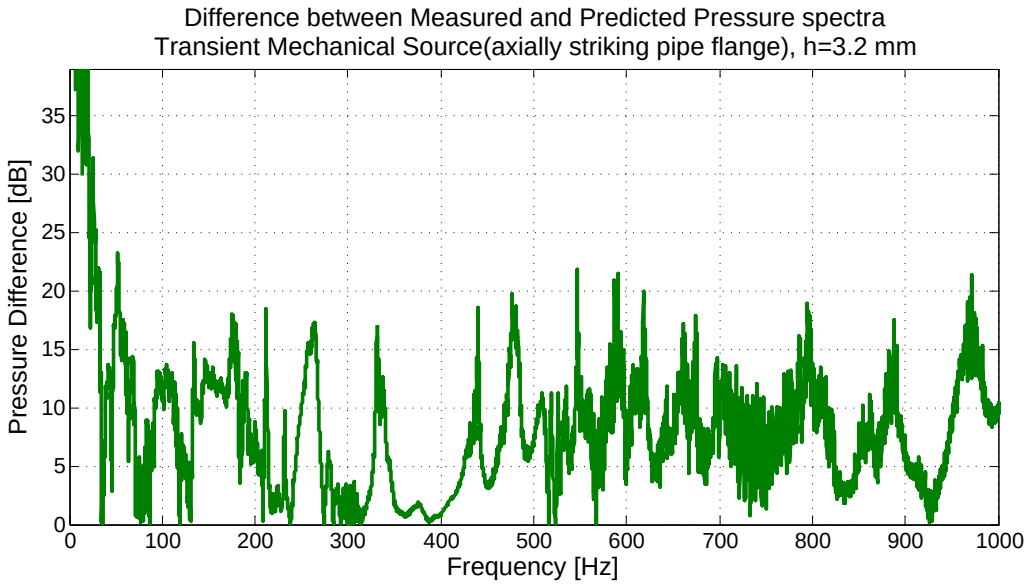

Figure 4.39. Difference between the measured and calculated pressure levels, as a result of measurements taken on the thin portion of the test section when the pipe is driven by the transient mechanical source.

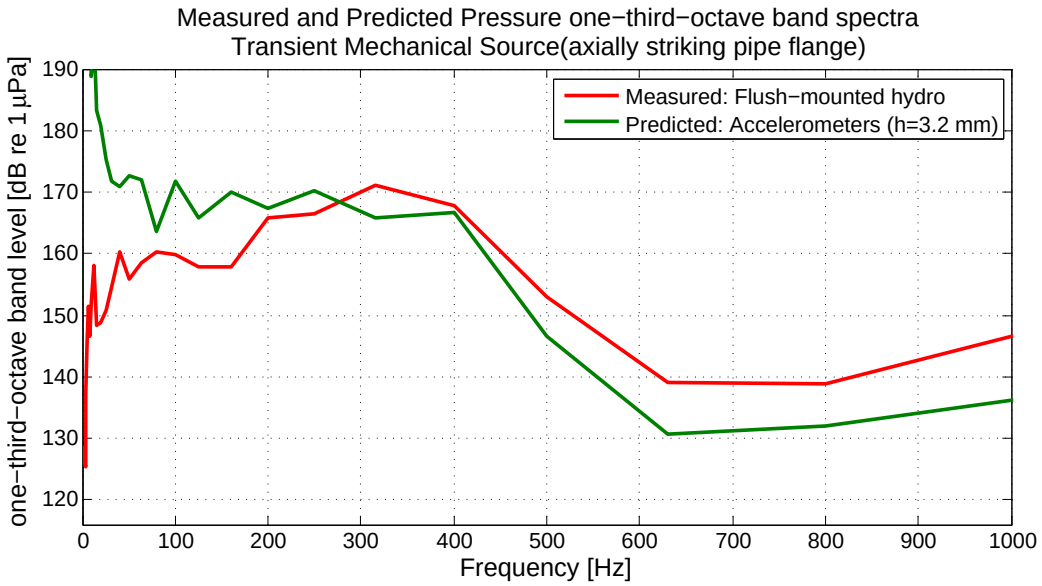

Figure 4.40. One-third-octave band sound pressure level as a result of measurements taken on the thin portion of the test section when the pipe is driven by the transient mechanical source.

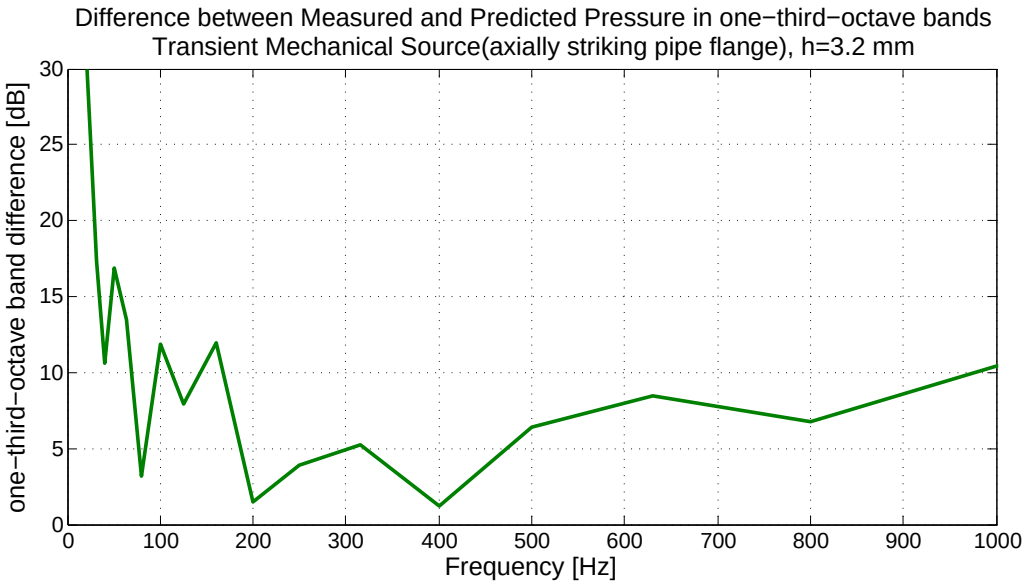

Figure 4.41. One-third-octave band dB difference between the measured and calculated pressure levels, as a result of measurements taken on the thin portion of the test section when the pipe is driven by the transient mechanical source.

4.4 Summary

The results of the measurements taken using an acoustical or mechanical excitation source show promise for the indirect method utilizing a ring of accelerometers to monitor the internal acoustic pressure. However, further investigation into the causes for the errors observed in the calculated pressure must take place in order for this method to become a valid absolute measurement of pressure. At this stage, the results confirm that the accelerometer ring method monitors the character and approximate level of the internal acoustic pressure fairly well at frequencies in the range from 200 Hz to 1000 Hz. The error below 200 Hz can possibly be attributed to lower radial displacements and less stable measured pressure at lower frequencies. For all cases of wall thickness and excitation sources, the error in the valid frequency range on average is between 5 and 10 dB. Table 4.2 presents the values of the average difference between the calculated pressure and the actual pressure for both cases of wall thickness.

Table 4.2. Error: Average difference between the directly-measured internal pressure and the indirectly-measured pressure using a ring of accelerometers.

Excitation Source		**Average error [dB] over 200 - 1000 Hz**	
		$h = 7.1$ mm	$h = 3.2$ mm
Acoustical	J9 projector	6.3	5.8
Mechanical	F4 shaker	5.1	6.0
Mechanical	axially hitting flange	5.6	6.9

Although the calculation of pressure using measurements from the thin portion of the test section is more accurate for the acoustical source, the calculation is still consistently around or above 5 dB different than the actual pressure measurement. However, the method tracks pressure changes very accurately. On average, the indirect method utilizing accelerometers can detect the change in pressure within 1 to 2 dB of the actual change in pressure level. If the pressure level under baseline conditions is known,

the accelerometers could aide in detecting abnormal pressure levels that could indicate fatigue or other unhealthy conditions in the pipe, although further measurements would be required to determine the cause.

CHAPTER 5

SUMMARY, CONCLUSIONS, RECOMMENDATIONS

5.1 Performance assessment

The objective of this thesis is to assess the feasibility of utilizing a ring of equally-spaced accelerometers to indirectly measure the internal acoustic pipe pressure. This was accomplished through the analysis of general results provided from an analytical model (presented in Chapter 3) as well as the results of experiments performed on a water-filled aluminum pipe for two cases of pipe wall thickness (presented in Chapter 4). Several factors were considered as potential challenges that could be faced in using this measurement method and calculation of pressure. The analytical model helped to determine the error produced by these factors, and it is suspected that they are likely candidates for contributors to the error observed in the results of the experiments.

The experimental results show that a ring of accelerometers can be used to pre-

dict the internal acoustic pressure level within 10 dB on average over the range from 200 Hz to 1000 Hz. Although, this may not be within the desired range of error, this method appears to be promising for the purpose of monitoring pressure levels and pressure fluctuations. The error in the predicted pressure level may be improved by selecting accelerometers that exhibit a smaller percentage of transverse sensitivity and equally-spacing them on the pipe with more precision. Further studies are needed to determine the limitations of the accelerometer ring with regards to pipe wall thickness and diameter size. However, the current studies prove that with some alterations, this method could very well be a useful tool for internal pipe acoustic pressure monitoring.

5.2 Configuration and selection of accelerometers

Piezoelectric accelerometers were chosen because they are a familiar tool in the field of vibration analysis, but they also are proven to be robust sensors with long-term stability. Yet, the transverse sensitivity of accelerometers and the proposed configuration in an equally-spaced circumferential ring present some challenges to accurately measuring the $n = 0$ breathing motion. These factors were analyzed through a model in Chapter 3 and the following sections will attempt to correlate the general conclusions provided from the model with the errors observed in the results of the experiments presented in Chapter 4.

5.2.1 Sensor configuration

The configuration of a circumferential ring of equally-spaced accelerometers was chosen to take advantage of the spatial harmonic motion of the pipe wall displacements. The calculation of internal acoustic pressure depends on the accurate detection of the $n = 0$ breathing mode amplitude and this configuration provides two methods for extracting the desired amplitude. Circumferential modal analysis can be performed, which results

in values for the amplitude of the $n = 0$ mode as well as the $n = 1$ bending mode and the first two lobar modes (when using six accelerometers). The $n = 0$ modal amplitude can also be extracted in the time domain via an average of the measured accelerations at each time position. The two methods of determining the $n = 0$ breathing mode amplitude consistently show good agreement, independent of the excitation. However, the calculation performed in the time domain is much less time consuming and may be a better tool if real time pressure monitoring is desired.

The effect of misplacing accelerometers was analyzed in Chapter 3. The result of this analysis showed that the calculation of pressure was sensitive to misplacements, especially at low frequencies below 200 Hz. Interestingly, the measurements also produce larger errors below 200 Hz. Although the likely conclusion would be that some of the low frequency error observed in the measurements is due to the misplacement of accelerometers, the source of the error in the model may not be the same source of error in the measurements. Since the average of the accelerometer measurements in the time domain to calculate the $n = 0$ amplitude is not sensitive to the sensor location and agreed well with the modal decomposition, the experimental results would suggest that sensor misplacement may not be a significant source of error.

The analysis in the model is done solely in the frequency domain, and therefore relies on circumferential modal decomposition to extract the $n = 0$ breathing mode amplitude. For the $n = 0$ amplitude, the calculation is essentially an average at each frequency of the amplitudes 'measured' by each of the accelerometers. In the model, the radial displacements are greater for lower frequencies and therefore the error is larger at these frequencies when an accelerometer is offset. However, the measurements do not exhibit the same frequency dependence. This can be attributed to the frequency-independent energy inputs in the model, where a more physically correct model would

require frequency-dependent energy inputs.

Incorrect placement of accelerometers leads to an incorrect calculation of the modal amplitudes using circumferential modal decomposition. The peaks observed in both the time domain and frequency domain calculations of the $n = 0$ modal amplitude may be due to contributions from higher order modes. Also, the $n = 0$ modal amplitude at frequencies below 200 Hz is at the same level as the $n = 2$ and $n = 3$ modes which may suggest that the $n = 0$ mode is not correctly calculated at these frequencies, which may lead to the error observed in this lower frequency range. Further research could study the effect of accelerometer misplacement by using a more precise method of placing the accelerometers and then determining whether the error is lower for these measurements. The accelerometers could also be purposefully misplaced by a small amount to see if the calculation of pressure is less accurate as would be expected. Additional rings of accelerometers could also be added in order to make a more complete analysis of the pressure fluctuations induced by the excitation source.

5.2.2 Sensor transverse sensitivity

All accelerometers inherently have a transverse sensitivity making the measurement of motion in the desired direction susceptible to contamination by the motion in the two orthogonal directions. A smaller transverse sensitivity will ultimately lead to better measurements. However, for the case in which the measurement of radial motion is desired, if the axial and tangential motions are small in comparison to the radial motion, a small percentage of transverse sensitivity will add negligible undesired motion to the measurements. As the transverse and axial motion was not measured in the experiments, the amplitude in these directions is unknown and a comparison to radial motion can't be made. Further studies should measure the motion in all three directions to make a

more complete analysis of the effect of the transverse sensitivity of accelerometers.

The effect of different transverse sensitivity was analyzed in the model. Similar to the accelerometer misplacement, the model predicts that the calculation of pressure is more sensitive to the transverse sensitivity at lower frequencies. However, a more general conclusion can be made that a larger percentage of transverse sensitivity produces a larger amount of error over all frequencies. Two assumptions, in regards to the transverse sensitivity, are made in the model that do not translate to real measurement conditions: the same transverse sensitivity is applied to all sensors and all accelerometers are oriented with the same angle of maximum transverse sensitivity. Therefore, the model should only be used to make more general conclusions rather than for a detailed analysis. For this reason, some of the error observed in the measurements could be attributed to a higher transverse sensitivity than is optimal for these measurements. Further studies could confirm or reject this conclusion by specifically selecting accelerometers with lower transverse sensitivity to see if the error is reduced.

5.3 Piping system

The effect of the geometry and material/fluid of the piping system on the calculation of the internal acoustic pressure using a ring of accelerometers was studied. General conclusions were made from the model and although the experiments did not study variations in the wall material or contained fluid, the experiments did study the effect of pipe wall thickness. The following sections provide some suggestions for further research to determine the source of the error and if it is possible to use this method on thicker industrial pipes.

5.3.1 Wall thickness

The displacement amplitudes of the pipe wall in response to an excitation are affected by the thickness of the wall. A thinner pipe wall will result in larger vibrations, as it is easier to displace than a thicker (heavier) wall. The model presented in Chapter 3 confirms this expectation.

For the same energy input, when the thickness is decreased, the amplitude of displacement increases. When the amplitude of displacement is larger, it is easier to measure the acceleration more accurately with accelerometers. Also, the noise floor of the accelerometers required for measurements on the thin-walled pipe can be higher than what would be required for thicker pipe walls. The noise floor of the accelerometers used in the measurements presented in Chapter 4 was low enough to measure the displacement amplitude resulting from the three different excitation sources for frequencies greater than 200 Hz.

The experimental results show that the calculation of pressure using the accelerometers mounted on the thick portion of the test section were more accurate (for the mechanical sources) than the calculation of pressure using the accelerometers mounted on the thin portion of the test section. The difference between the two cases is only about 1 dB. It should be noted that the pressure sensors were located on the thick portion of the test section, which may explain why the accelerometers for the thick pipe wall case performed slightly better. It would be expected that the thinner pipe wall would perform even better if the pressure sensors were located closer to this measurement location.

One contributing factor may involve the location of the excitation source. The mechanical source will cause displacements due to the movement of the source itself rather than displacements caused by the internal acoustic pressure pulsations. Therefore, if the source is located far enough away, the displacement of the pipe wall is in response to only

the plane wave propagation of the acoustic pressure which does not attenuate. Further studies may wish to examine this factor in more detail.

The ratio of different propagating wave energies may be another factor responsible for the poor measurements seen on the thicker walled pipe. As the thickness was varied on the same piping system, the propagating wave energy amplitudes should not change with respect to thickness, though the wall may react differently to the amounts of energy.

It would be interesting to examine these factors separately and their effect on varying thickness of the pipe wall. Since the measurements presented in Chapter 4 only included two values of thickness, more values of thickness may wish to be studied further. Varying these factors may be easier to implement in a finite element model as the cost of several variations of actual pipes may exceed the cost available to researchers.

5.3.2 Wall material

Similar to the pipe wall thickness, the model presented in Chapter 3 confirms the expectation that a stiffer wall material results in smaller wall displacements. The density of the material also affects the wall displacements, making the wall more difficult to move if the material is more dense (heavier). Although only an aluminum pipe was used in the experiments presented in Chapter 4, results similar to changes in wall thickness would be expected for stiffer and denser wall materials, where the accuracy of the calculation of pressure decreases for thicker, denser, and stiffer pipe walls. Unfortunately, many industrial pipes fall within all three categories.

5.3.3 Contained fluid

It is expected that a heavier fluid will be able to displace the wall by a larger amount due to an increase in the fluid loading. This expectation is confirmed by the model

in Chapter 3. However, only the response of a water-filled pipe was measured in the experiments. The effect of different contained fluids would also be an interesting factor to assess in the laboratory.

5.4 Other considerations

The experimental set-up could be altered to possibly produce better results. The desired measurement was of the plane wave propagation only without reflections. The length of the pipe was considered long enough that the amplitude of the reflections were expected to be negligible at the location of the measurements. To ensure no reflections, an anechoic termination could be installed at both ends of the pipe, this would also allow the pipe to be shorter in length. Although the current set-up represents less than ideal conditions, it may correspond more closely with conditions present for pipes in the field, where bends in the pipe may produce unwanted reflections. Other configurations of the set-up including bends and other discontinuities could be studied to understand the effect of more realistic conditions.

As mentioned previously, the location of the excitation source could be varied. Though, the response with respect to a wider variety of sources could also be studied. Specifically, it would be advantageous to look at the response of the pipe to an actual pump and valve that would produce the acoustic pressure more closely resembling those produced in the field. The better the experiment represents field conditions, the greater confidence one has that the experimental results will represent those in the field.

Yet another factor to consider is the accuracy of the error calculation. The error was determined as the difference between the directly-measured pressure and the calculated pressure using the measurements acquired from the ring of accelerometers. It is assumed

that the directly-measured pressure is the actual pressure level of the internal acoustic pressure in the pipe. However, there may be errors not considered in this calculation such as the hydrophones' sensitivity to pipe wall accelerations. It is also assumed that the pressure is negligibly different at locations close to the location of the direct measurement. The accelerometer rings were a small distance from the hydrophone ring location, which may account for some of the difference in pressure levels, but most likely not to the extent observed.

5.5 Conclusions

The use of a ring of accelerometers as a non-invasive method for measuring the internal acoustic pipe pressure shows promise in its ability to monitor pressure fluctuations with the objective of detecting changes in the pressure level that may indicate pipe fatigue. A number of alterations could be made that may improve the accuracy of the measurements including more precise placement of the accelerometers and selecting sensors with lower transverse sensitivities. If a more precise placement and a lower transverse sensitivity of the accelerometers does not reduce the error to acceptable levels, then the use of other sensors in addition to the accelerometers or the use of a different sensor entirely may need to be considered. However, if the measurements improve, alterations to the experimental set-up can be made to mimic more realistic piping conditions. At this time, a ring of accelerometers can aide in monitoring changes in acoustic pressure, although other methods must be used to determine absolute pressure levels.

BIBLIOGRAPHY

[1] Schirmacher, R. and R. Baars (2008) "Sound propagation on a high pressure gas pipe," in *Proceedings of the Acousitcal Society of America and Euronoise*, Paris,France.

[2] Conti, M., A. Stokes, and C. Corrado (2001) "Array-based methods of characterizing piping component acoustic behavior," in *Proceedings of ASME International Mechanical Engineering Congress and Exposition*, New York,New York.

[3] de Jong, C. A. F. (1994) *Analysis of pulsations and vibration in fluid-filled pipe systems*, PhD dissertation, TNO Institute of Applied Physics, Delft, Netherlands.

[4] Pinnington, R. J. and A. R. Briscoe (1994) "Externally Applied Sensor for Axisymmetrical Waves in a Fluid-Filled Pipe," *Journal of Sound and Vibration*, **173**(4), pp. 503–516.

[5] Royston, T. J. (1995) "Technical Note - Shaped Polyvinylidene Fluoride (PVDF) Sensors for Intelligent Measurement of Plane-Wave Acoustic Pressure in Liquid-Filled Pipes," *Noise Control Engineering Journal*, **43**(1), pp. 15–20.

[6] Muggleton, J. M., M. J. Brennan, R. J. Pinnington, and Y. Gao (2006) "A novel sensor for measuring the acoustic pressure in buried plastic water pipes," *Journal of Sound and Vibration*, **295**(3-5), pp. 1085–1098.

[7] Szasz, G., K. K. Fujikawa, and G. DeBoo (2006) "Assessment of Steam Line Dynamic Pressures Using External Strain Gage Measurements," *ASME Conference Proceedings*, **2006**(47543), pp. 761–765.

[8] Pierce, A. D. (1989) *Acoustics : an introduction to its physical principles and applications*, Acoustical Society of America, Woodbury, N.Y.

[9] Pavic, G. (1992) "Vibroacoustical Energy-Flow through Straight Pipes," *Journal of Sound and Vibration*, **154**(3), pp. 411–429.

[10] Gao, Y., M. J. Brennan, P. F. Joseph, J. M. Muggleton, and O. Hunaidi (2005) "On the selection of acoustic/vibration sensors for leak detection in plastic water pipes," *Journal of Sound and Vibration*, **283**(3-5), pp. 927–941.

[11] Fahy, F. and P. Gardonio (2007) *Sound and structural vibration : radiation, transmission and response*, Elsevier/Academic, Amsterdam ; London.

[12] a PCB Piezotronics Div., I. S. (2011), "Technical Information: Selecting and Installing Accelerometers," `http://www.imi-sensors.com Technical Information`.

[13] Junger, M. C. and D. Feit (1986) *Sound, structures, and their interaction*, MIT Press, Cambridge, Mass.

[14] Leissa, A. W. (1973) *Vibration of Shells*, National Aeronautics and Space Administration, Washington, D.C.

[15] Skelton, E. A. and J. H. James (1997) *Theoretical acoustics of underwater structures*, Imperial College Press; Distributed by World Scientific Pub. Co., London; River Edge, NJ.

[16] Soedel, W. (1993) *Vibrations of Shells and Plates*, Marcel Dekker, Inc., New York, New York.

[17] Kinsler, L. E., A. R. Frey, A. B. Coppens, and J. V. Sanders (2000) *Fundamentals of Acoustics*, John Wiley, New York.

[18] Morse, P. M. (1981) *Vibration and Sound*, Acoustical Society of America, Woodbury, N.Y.

[19] Blackstock, D. T. (2000) *Fundamentals of physical acoustics*, Wiley, New York.

[20] Bendat, B. and A. Piersol (1986) *Random Data Analysis and Measurement Procedures*, second ed., John Wiley and Sons.

[21] Bonness, W., J. Fahnline, and D. Jenkins (2003) "Circumferential Wavenumber Decomposition of Experimental Data From Structures Containing Circular Symmetry," in *Proceedings of IMAC-XXI: A Conference on Structural Dynamics*, Kissimmee, Florida.

[22] Fuller, C. R. and F. J. Fahy (1982) "Characteristics of Wave-Propagation and Energy-Distributions in Cylindrical Elastic Shells Filled with Fluid," *Journal of Sound and Vibration*, **81**(4), pp. 501–518.

[23] MATLAB (2009) *version 7.8.0 (R2009a_x64)*, The MathWorks Inc., Natick, Massachusetts.